

UC San Diego

UC San Diego Electronic Theses and Dissertations

Title

Multiscale simulations and design of porous materials

Permalink

<https://escholarship.org/uc/item/17c5h0g1>

Author

Zhang, Xuan

Publication Date

2016

Peer reviewed|Thesis/dissertation

UNIVERSITY OF CALIFORNIA, SAN DIEGO

Multiscale simulations and design of porous materials

A dissertation submitted in partial satisfaction of the
requirements for the degree
Doctor of Philosophy

in

Engineering Sciences (Mechanical Engineering)

by

Xuan Zhang

Committee in charge:

Professor Daniel M. Tartakovsky, Chair
Professor Prabhakar R. Bandaru
Professor Marcos Intaglietta
Professor Ratneshwar Lal
Professor Kesong Yang

2016

Copyright
Xuan Zhang, 2016
All rights reserved.

The Dissertation of Xuan Zhang is approved, and it is acceptable in quality and form for publication on microfilm and electronically:

Chair

University of California, San Diego

2016

DEDICATION

My beloved parents, Keming Zhang and Yuan Hao

EPIGRAPH

*The solutions all are simple - after you have arrived at them. But they're simple only
when you know already what they are.*

—Robert M. Pirsig

TABLE OF CONTENTS

Signature Page	iii
Dedication	iv
Epigraph	v
Table of Contents	vi
List of Figures	viii
List of Tables	x
Acknowledgements	xi
Vita	xiii
Abstract of the Dissertation	xiv
Chapter 1 Introduction	1
1.1 Nanoporous materials in science & engineering	1
1.2 Multiphysics and multiscale modeling of nano-porous materials	2
1.3 Objectives of this dissertation	4
1.4 Organization of this dissertation	6
Chapter 2 Design of Nanoporous Materials with Optimal Sorption Capacity	8
2.1 Abstract	8
2.2 Introduction	9
2.3 Problem formulation	11
2.4 Macroscopic properties of nanoporous materials	15
2.5 Simulation results	17
2.6 Conclusions	22
2.7 Acknowledgements	23
Chapter 3 Effective Ion Diffusion in Charged Nanoporous Materials	25
3.1 Abstract	25
3.2 Introduction	26
3.3 Problem Description	29
3.3.1 Microscopic transport model	30
3.3.2 Macroscopic Transport Model	35
3.4 Application to electrical double layer capacitors	41
3.5 Conclusions	48
3.6 Acknowledgments	50

Chapter 4	Optimal Design of Nanoporous Materials for Electrochemical Devices	51
4.1	Abstract	51
4.2	Introduction	52
4.3	Macroscopic transport model	53
4.4	Electrosorption on charged porous materials	54
4.4.1	Parameters for electrosorption study	56
4.4.2	Results and discussions	57
4.5	Optimum design of microstructure for charged materials	62
4.5.1	The optimization problem	63
4.6	Conclusions	64
4.7	Acknowledgements	65
Chapter 5	Effective Transport Properties for Dendritic Spine F-actin Network	66
5.1	Abstract	66
5.2	Instruction	67
5.3	Effective transport properties of spine network structure	70
5.3.1	Problem formulation	71
5.3.2	Macroscopic properties of porous material	73
5.4	Results and discussion	74
5.4.1	Porosity	75
5.4.2	Porous morphology	77
5.4.3	Tortuosity	79
5.5	Future work – MCell simulation	81
5.6	Conclusions	82
5.7	Acknowledgements	83
Chapter 6	Conclusions	84
Appendix A	Derivation of the boundary condition	88
Appendix B	Homogenization of transport equations	90
Appendix C	Homogenization of PNP equations	95
Appendix D	Macroscopic model of an EDLC cell	100
Appendix E	Homogenization of diffusion equation	106
Bibliography	111

LIST OF FIGURES

Figure 2.1:	A schematic representation of Material 1 (left) and the corresponding unit cell \mathcal{U} (right). The unit cell is a $2y_1^c$ by y_2^c	14
Figure 2.2:	The horizontal χ_1 (left) and vertical χ_2 (right) components of the closure variable $\boldsymbol{\chi}(\mathbf{y}) = (\chi_1, \chi_2)^\top$ defined on the fluid-domain $\mathcal{P}_{\mathcal{U}}$	17
Figure 2.3:	Dependence of effective longitudinal diffusion coefficient D_{11} (left) and effective reaction constant γ_{eff} (right) on pore radius R	18
Figure 2.4:	Dependence of the longitudinal (D_{11}) and transverse (D_{22}) components of the effective diffusion tensor (left) and effective reaction	19
Figure 2.5:	Dependence of the longitudinal (D_{11}) and transverse (D_{22}) components of the effective diffusion tensor (left) and effective reaction	20
Figure 2.6:	A schematic representation of Material 2 and the corresponding unit cell \mathcal{U} (right).	21
Figure 2.7:	Dependence of the longitudinal (D_{11}) and transverse (D_{22}) components of the effective diffusion tensor on the number of microporous	22
Figure 3.1:	(a) A unit cell comprising a homogeneous isotropic nanoporous material with porosity $\omega = 0.67$ and pore throat size 1.5 nm.	39
Figure 3.2:	The normalized effective diffusion coefficient of an isotropic nanoporous material, $\mathcal{D}^{\text{eff}}/D$, computed alternatively with Bruggeman's relation	40
Figure 3.3:	Schematic representation of an electrical double layer capacitor (EDLC) cell. Pore space of the cathode and anode and the separator	42
Figure 3.4:	Measured EDLC voltage response to charging[96] (stars), and its counterparts predicted with the original model[96] (dotted line)	46
Figure 3.5:	Temporal snapshots, at $t = 1, 8$ and 18 s, of the (a) ion concentration $C(x, t)$ and (b) electric potential $\Phi(x, t)$ profiles computed	47
Figure 4.1:	Conceptual and schematic representation of hierarchical porous texture containing mesopores and micropores[110].	55
Figure 4.2:	Effective diffusion coefficients \mathbf{D}^{eff} as a function of concentration, for material 1 with diffuse layer potential $\varphi_d = 0.2$ V.	58
Figure 4.3:	Effective diffusion coefficients \mathbf{D}^{eff} as a function of concentration, for material 2 with diffuse layer potential $\varphi_d = 0.2$ V.	58
Figure 4.4:	Longitudinal transport D_2 as a function of dilute concentration $C = 0.01\text{M}$, for material 2 with different diffuse layer potentials.	59
Figure 4.5:	Effective diffusion coefficients \mathbf{D}^{eff} as a function of diffuse layer potential, for material 1 with concentration $C = 0.01$ M	60
Figure 4.6:	Effective diffusion coefficients \mathbf{D}^{eff} as a function of diffuse layer potential, for material 2 with concentration $C = 0.01$ M	61
Figure 4.7:	Effective diffusion coefficients \mathbf{D}^{eff} as a function of diffuse layer potential, for material 2 with concentration $C = 0.1$ M	61

Figure 5.1:	3-D dendritic spine head model. Porosity of this F-actin network of the cytoskeleton is 0.689.	70
Figure 5.2:	2-D cross sections sampling and 3-D representative volume element.	71
Figure 5.3:	XY plane and XZ plane cross sections of 3-D actin spin model in Fig. 5.2a	72
Figure 5.4:	Unit cells \mathcal{U} in XY and XZ planes. The \mathcal{U} -periodicity of $\chi(\mathbf{x})$ is enforced. Representative cell size is $100 \text{ nm} \times 100 \text{ nm}$	76
Figure 5.5:	Simulation results of closure variable χ of the first unit cell in Fig.5.4a	76
Figure 5.6:	Porosity of selected unit cell satisfies Gaussian distribution. Mean value of porosity of all samples, consistent in XY-plane and XZ-plane	77
Figure 5.7:	Dependency of effective diffusion coefficients and porosity in XZ plane	78
Figure 5.8:	Dependency of effective diffusion coefficients and porosity in XY plane	78
Figure 5.9:	MCell simulation of 2-D unit cell. (a) is particle distribution at steady state. Porosity of this unit cell is $\varepsilon = 0.757$ (COMSOL result)	82

LIST OF TABLES

Table 3.1:	Parameter values used in the experimental study[96] of supercapacitors.	45
Table 4.1:	Geometry limits of porous structure	63
Table 4.2:	Material 1, dilute electrolyte ($C = 0.1$ M and 0.01 M), $\varphi_d=0.3$ V	64
Table 4.3:	Material 2, dilute electrolyte ($C = 0.1$ M and 0.01 M), $\varphi_d=0.3$ V .	64

ACKNOWLEDGEMENTS

I would like to express my sincerest gratitude to my advisor Prof. Daniel Tartakovsky for his distinct, adroit thoughts that broaden the scope of my thinking. None of this work could have been possible without his guidance and support.

I thank Dr. Marcos Intaglietta, Dr. Prabhakar R. Bandaru, Dr. Ratneshwar Lal and Dr. Kesong Yang for being my committee members and for providing valuable comments and suggestions in this work. I am especially thankful to Dr. Tom Bartol for his time and for numerous discussions that moved my research forward.

I am thankful to my lab mates for their friendship during the past few years. Thanks to Francesca and Natalia for their consideration and 'sugary' support. My thanks also go to my friends and San Diego Kendo club who made my life outside campus joyful and enjoyable. Thanks to tranquil and breathtaking national parks that eased me during those hard times.

I would like to give my deepest appreciation to my parents for their unconditional love and support that have enabled me to complete my Ph.D work.

Chapter 2 is a reformatted reprint of: Zhang, X., Urita, K., Moriguchi, I. and Tartakovsky, D.M. *Design of nanoporous materials with optimal sorption capacity*. Journal of Applied Physics, 117(24), p.244304, 2015. The dissertation author was the primary investigator and author on this paper.

Chapter 3 is a reformatted reprint of: Zhang, X. and Tartakovsky, D.M. *Effective ion diffusion in charged nanoporous materials*. Submitted for review to Journal of The Electrochemical Society, 2016. The dissertation author was the primary investigator and author on this paper.

Chapter 4 is a reformatted reprint of: Zhang, X. and Tartakovsky, D.M. *Optimal*

design of nanoporous materials in electrochemical devices. Submitted for review to Applied Physics Letter, 2016. The dissertation author was the primary investigator and author on this paper.

Chapter 5 is currently being prepared for submission for peer review and publication: Zhang, X. Bartol, T. and Tartakovsky, D.M. *Effective transport properties for dendritic spine F-actin network*. The dissertation author is the primary investigator and author on this paper.

VITA

2016	Doctor of Philosophy in Engineering Sciences (Mechanical Engineering), University of California, San Diego.
2012	M.Sc. in Engineering Sciences (Mechanical Engineering), University of California, San Diego.
2011	BE in Energy and power engineering, Xi'an Jiaotong University, Xian, China.

PUBLICATIONS

X. Zhang, K. Urita, I. Moriguchi, and D. M. Tartakovsky. “Design of nanoporous materials with optimal sorption capacity”, *J. Appl. Phys.*, 117(24):244304, 2015.

X. Zhang and D. M. Tartakovsky, “Effective ion diffusion in charged nanoporous materials”. Submitted for review to *J. Electrochem. Soc.*, 2016.

X. Zhang and D. M. Tartakovsky, “Optimal design of nanoporous materials in electrochemical devices”. Submitted for review to *Appl. Phys. Lett.*, 2016.

X. Zhang, T. M. Bartol, Jr. and D. M. Tartakovsky, “Effective transport properties for dendritic spine F-actin network.” Under preparation

ABSTRACT OF THE DISSERTATION

Multiscale simulations and design of porous materials

by

Xuan Zhang

Doctor of Philosophy in Engineering Sciences (Mechanical Engineering)

University of California, San Diego, 2016

Professor Daniel M. Tartakovsky, Chair

Nanoporous materials are used in the variety of fields, ranging from medicine and biosensors to clean energy and purification. Technological advances have enabled one to manufacture nanoporous materials with a prescribed pore structure. This raises a possibility of using controllable pore scale properties (e.g., pore size distribution, pore connectivity and tortuosity) to design materials with desired macroscopic properties (e.g., porosity, effective diffusion coefficient and effective electrical conductivity). Upscaling techniques, such as homogenization via multiple-scale expansions, provide a framework to connect these two scale. This research uses such techniques to optimize

macroscopic properties of a material by using its microscopic properties as decision variables.

This research aims to obtain qualitative understanding and quantitative predictions of macroscopic properties of nanoporous materials to transmit solutes that undergo non-equilibrium adsorption and local electrochemical surface reactions at the fluid-solid interface. The first part of this work focuses on the design of hierarchical nanoporous materials with optimal permeability and sorption capacity. A class of nanoporous materials whose pore space consists of ordered nanopores interconnected by nano-channels is considered. Anisotropic effective diffusion coefficients and adsorption coefficients of such materials are expressed in terms of pore properties and connectivity. Nano-channels can significantly alter diffusive properties and increase its adsorbing capacity.

The second part of this work contains a macroscopic model of ion transport in electrically charged nanoporous materials. The corresponding effective diffusion coefficients, electric conductivity and transference numbers account for dynamic changes in the electrical double layer (EDL), possible overlap of EDLs in nanopores, and electrochemical conditions (i.e., concentration of ions in the electrolyte). Our effective coefficients are derived from the first principles and vary with a range of electrochemical conditions (e.g., initial concentration of ions in the electrolyte). The resulting model predictions of the EDLC voltage response match the experimental data better than the original model does.

The last part of this work is devoted to derivation of macroscopic properties of three-dimensional dendritic spines. The effective diffusion coefficient estimated with this analysis is used to quantify travel time of electric signal through the spine.

Chapter 1

Introduction

1.1 Nanoporous materials in science & engineering

Nanoporous materials, as a category of nanostructured materials, possess distinguished features such as high interior surface, distinctive porous structures and bulk properties. Their unique surface features make nanoporous materials attractive for applications in the fields ranging from ion exchange, adsorption (for separation) and catalysis to purification and sensor. Nanoporous materials attract technological and scientific interest because of their ability to chemically and physically interact with atoms, ions and molecules on their large interior surfaces. New technological fields engendered by nanoporous materials include infusion chemistry, molecular manipulations and reaction in the nanoscale for making quantum nanostructures [59, 27]. Because of the potential to use nanomaterial topography and spatial distribution of functional groups, bio-nanomaterials are applied to control proteins, cells, tissue interactions and for bioseparations and other biological applications [80, 71, 31].

Of particular interest is the use of nanomaterials in clean energy and other

environment-oriented fields. For example, porous membranes are the top choices for new separation systems in chemical industry, hot gas filtration materials for energy production, and separation for filtering poisonous and nano-particles cleanup technologies. Environmentally friendly modes of transportation, such as hybrid, electric and fuel cell powered vehicles, place different requirements on porous materials for electrodes, separators, and gas storage media. Rechargeable batteries need cost-effective and efficient porous materials for electrodes and separators [82, 85, 26, 56, 64].

1.2 Multiphysics and multiscale modeling of nanoporous materials

Distributions of pore sizes, shapes and voids directly affect functional macroscopic properties of porous materials. Nanoporous structures can be tailored to improve a material's ability to perform a required function. The overall performance of a tailored material are not only determined by atoms and molecular composition, but also the transport mechanisms that take place in the pores.

When accounting for driving force inside the pores, advection due to pressure-driven flow is often not negligible; electric potential-driven ion transport is often referred to as electromigration. Pore size variability affects the importance of different transport mechanisms. Macropores, pore size larger than 50 nm in diameter, are much larger than the mean free path of molecular species of interest. In this cases, molecular diffusion is significant due to predominance of molecule-molecule collision over molecule-wall collisions. Mesopores, pore size 2 to 50 nm, are on the same order or smaller than the mean free path and Knudsen diffusion is the predominant

mechanism that accounts for the relative importance of molecule-wall collisions. If the pore surface is sensitive to the specific adsorption features forming strong bond of the molecule-solid pair, multilayer adsorption and capillary transport may occur. Micropores (pore diameter < 2 nm) are comparable in size to molecules. In this regime, micro-phenomena depend on both molecular size and specific interactions with the solid. For instance, in ionic solution, electrical double layer forms on the solid surface and impacts transport inside micropores [60, 82, 31].

A complete analysis of composite porous materials problems is extremely difficult. For example, the dispersed phases (fibers or particles) in porous materials, which may be randomly distributed, give rise to uncertainties in the thermal or electrical conductivity; moreover, problems of discontinuity of conductivity across the phase boundaries might arise [100]. Direct solutions provide quantitative information of the physical processes at all scales only when the resolving all small-scale features of a physical problem is affordable. A direct numerical solution of multiscale problems is computationally prohibitive even with modern supercomputers. The major problem is the size of computation [29]. Multiscale methods have been proposed to bridge distinct scales ranging from particle to continuum. From engineering viewpoint, macroscopic models with approximated effective conductivity and permeability properties are frequently deployed in multiscale simulations [82]. A motivation for multiscale modeling comes from the requirement of combining the efficiency of macroscale models and the accuracy of microscale models. Some knowledge of microscale information is crucial for predicting tailored materials while empirically obtained macroscale models are very efficient but often not accurate enough. Microscopic models, on the other hand, are able to incorporate microstructure and give better accuracy of solutions, but too

expensive to be used to model systems of real interest.

Major analytical approaches to multiscale problems include matched asymptotic expansions, averaging method, homogenization methods and renormalization group methods. Analytical methods along with comprehensive interpretation of multiscale physics provide a needed insight into the nature of many problems. Such methods, a problem can be either simplified to the point of being amenable to analytical treatment or provide guidance for designing and analyzing numerical algorithms. Matched asymptotics methods are used for problems that have different dominant features in distinct regions. An “inner region” or “local region” is one in which a solution changes rapidly. Effective models match the leading-order behavior of the solution in both inner and outer regions. Analyzing disparate scales through multiscale expansions is systematic and effective. Homogenization methods based on the multiple-scale expansions establish effective equations for slow variables (large scale) by averaging out fast variables (local scale). Numerical techniques, such as multigrid methods and adaptive mesh refinement, are examples of resolving the details of a solution efficiently. In this work, I use a homogenization upscaling method to study nanoporous materials.

1.3 Objectives of this dissertation

This research provides an analytical methodology to determine macroscopic functional properties of nanoporous materials. Continuum-scale transport models are introduced with effective properties that account for the pore structure and microscale behavior at solid-fluid interface. With controlled and tailored molecular treatment, the desirable properties of porous materials can be purposely formed by designing

their microstructure. This research presents a methodology for systematical design and optimization of micropore structure, obviating the need for endless and blind trial and errors in materials design.

The specific objectives are to

1. Derive a macroscopic transport model for non-equilibrium Langmuir-type adsorption reactions. Express effective diffusion coefficients and adsorption reaction rates that account for complex pore structure and microscale processes.
2. Derive a macroscopic ion transport model that captures the significant influence of formation of electric double layer on the solution-solid surface. Effective diffusion coefficients of positive/negative charges are specified under different electric double layer conditions.
3. Validate the macroscopic model with experimental data of electric double layer capacitor charging and include effects of different diffuse layer potentials and solution concentrations on macroscopic diffusion coefficients.
4. Design and optimize sorption materials with tunnels-connected microporous structures and nonequilibrium Langmuir-type adsorption.
5. Design and optimize hierarchical porous electrode materials composed of micro-mesopores. Using macroscopic effective properties as complementary instruction, microscale structures are optimized to reach material functional goals.
6. Introduce periodic closure formula to upscale an actin network and calculate effective diffusion coefficients of an F-actin dendritic spine model through particle methods. Discuss representative unit cell size and microscale morphology of the actin network.

1.4 Organization of this dissertation

Chapter 1 discusses the profound impact of nanoporous materials on various applications in modern live. Alternative techniques of multiscale and multiphysics analyses of porous materials techniques are briefly reviewed. Objectives and motivations of this research are formulated.

In chapter 2, I derive a homogenized formula by relating pore-scale parameters and macroscopic properties. Using controllable pore-scale parameters (e.g., pore size and connectivity) enables one to manufacture nanoporous materials with desired diffusion coefficients and adsorption capacity. This provides a means of guiding experimental design. A class of nanoporous materials, whose pore space consists of nanotunnels interconnected by microporous tubes (carbon nanotubes), is considered. I express the anisotropic diffusion coefficients and adsorption coefficient of such materials in terms of tunnel's properties (pore radius and inter-pore throat width) and their connectivity (spacing between the adjacent tunnels and microporous tube-bridge density). Micropore structures details (i.e., intersection angle, porosity, tube-bridge densities) are discussed with the goal of optimizing permeability and sorption capacity.

Chapter 3 contains a study of porous materials filled with a charged ion solution. I derive a new homogenized ion transport model, which considers the effect of electrical double layer behavior in micropores. Homogenized Nernst-Planck equations are represented by bulk properties of the solution and macroscopic effective diffusion coefficients, which are modified through digging into microscopic double layer behavior in pore structure. To demonstrate the superiority of this model, I simulate the behavior of electric double layer capacitors under a constant current charging process. Simulation results using my effective diffusion coefficients show a much

more prominent congruency with experimental data than using diffusion coefficient predicted by widely used Bruggeman's effective medium theory. Meanwhile, to address the significance of microscopic double layer potential for determining effective diffusion coefficients, different charging and solution conditions are studied and compared with Bruggeman's predictions.

In chapter 4, a class of hierarchical micro-meso porous materials are considered. Because of the high interior surface area provided by micropores and the sustainable conductivity in mesopores, I concentrate on the use of such materials in next-generation energy storage devices. The macroscopic ion transport model derived in chapter 3 provides guidance for optimization of electrolyte conductivity by designing the porous structure and electrode porosity. The double layer formed in micropores not only effects real specific surface area of such materials, but also impacts transport paths of ions-filled mesopores. An optimum micro-meso hierarchical structure is suggested through an optimization analysis of micro- and meso-pore sizes, ion concentrations and solid-fluid interface potentials.

In chapter 5, two-dimensional (2D) cross sections of a F-actin cytoskeleton in purkinje cell dendritic spine allow us to interpret the microstructure of actin through characteristic unit cells. Pore-structure information is assembled and interpreted through macroscopic effective diffusion coefficients. A sufficient and adequate amount of unit cells is collected in order to predict the overall anisotropic effective diffusion coefficients using finite element methods. Representative cell size and morphologies of the pore structure are discussed. The prediction of effective diffusions for the three-dimensional network structure is alternatively achieved via MCell using particle methods.

Chapter 2

Design of Nanoporous Materials with Optimal Sorption Capacity

2.1 Abstract

Modern technological advances have enabled one to manufacture nanoporous materials with a prescribed pore structure. This raises a possibility of using controllable pore-scale parameters (e.g., pore size and connectivity) to design materials with desired macroscopic properties (e.g., diffusion coefficient and adsorption capacity). By relating these two scales, the homogenization theory (or other upscaling techniques) provides a means of guiding the experimental design. To demonstrate this approach, we consider a class of nanoporous materials whose pore space consists of nanotunnels interconnected by microporous tube bridge. Such hierarchical nanoporous carbons with mesopores and micropores have shown high specific electric double layer capacitances and high rate capability in an organic electrolyte. We express the anisotropic diffusion coefficient and adsorption coefficient of such materials in terms of the tunnels' properties (pore radius

and inter-pore throat width) and their connectivity (spacing between the adjacent tunnels and microporous tube-bridge density) Our analysis is applicable for solutes that undergo a non-equilibrium Langmuir adsorption reaction on the surfaces of fluid-filled pores, but other homogeneous and heterogeneous reactions can be handled in a similar fashion. The presented results can be used to guide the design of nanoporous materials with optimal permeability and sorption capacity.

2.2 Introduction

Small pore sizes and large surface porosity are some of the unique properties of nanoporous materials, which can be used in a wide range of applications involving ion exchange, adsorption, sensing and catalysis.[85, 105, 72] Nanoporous materials play central role in biomedical diagnostics, such as combinatorial biochemistry on-a-chip, chromatography, biosensors, cell manipulation and DNA analysis.[28, 2, 77] Because of their high electrical conductivity and wettability towards electrolytes, nanoporous materials might significantly boost the performance of energy storage devices.[1, 50, 49]

Desirable properties of manufactured (nano)porous materials can be enhanced by controlling their pore structure and physicochemical properties of emerging pore networks.[27] For instance, introduction of active sites onto pore surfaces of mesoporous metallosilicate materials is a promising venue for designing novel adsorbents and catalysis.[62] Embedment of microporous tubes[104] between layers of macro- or nanopores results in new materials with superior mechanical and thermal properties.[108] For example, hierarchical nanoporous carbons with mesopores and micropores have shown high specific electric double layer capacitances and high rate capability in an organic electrolyte.

Quantitative predictions of macroscopic properties of such new materials (e.g., their sorption capacity or thermal conductivity) require the ability to relate these properties to their pore-scale counterparts, such as a pore-size distribution and pore-network connectivity.[86] This can be accomplished with a variety of upscaling techniques, including volume averaging[102] and homogenization via multiple-scale expansions[42, 14, 5]. We use the latter approach to predict anisotropic diffusion coefficients and effective adsorption rates for a class of nanoporous materials[63], whose synthesis allows one to control their pore structure. It is worthwhile emphasizing that the use of various homogenization techniques to derive effective (continuum- or Darcy-scale) models of reactive transport in porous media (primarily subsurface environments) is not new.[30, 94, 99, 4] The novelty of our study comes from using such techniques to optimize macroscopic properties of a material by using its microscopic properties as decision variables.

The effective reaction rate in a given solid-solution system is an essential factor for sorption system design. Our analysis is applicable for solutes that undergo a non-equilibrium Langmuir-type adsorption reaction on the surfaces of fluid-filled pores, but other homogeneous and heterogeneous reactions can be handled in a similar fashion. The presented results can be used to guide the design of nanoporous materials with optimal permeability and sorption capacity.

In section 2.3, we formulate a non-equilibrium pore-scale model, which is based on the first-order theory of sorption kinetics[11, 22, 76]. The corresponding continuum-scale model is derived in Section 2.4. This model relates the macroscopic properties of a nanoporous material (i.e., its diffusion coefficient and adsorption capacity) to its pore-scale counterparts (e.g., the radii of micro- and macro-pores, and the size

of nanobridges). In Section 2.5, we present simulations results and discuss their implications for material design. Our findings are summarized in Section 2.6.

2.3 Problem formulation

Consider a nanoporous material $\hat{\Omega}$ with a characteristic length L . Let $\hat{\mathcal{P}}$ denote the part of this material occupied by nanopores whose characteristic length scale, e.g., a typical pore diameter, is l such that $\epsilon \equiv l/L \ll 1$. The impermeable solid skeleton $\hat{\mathcal{S}}$ occupies the rest of the nanoporous material, i.e., $\hat{\Omega} = \hat{\mathcal{P}} \cup \hat{\mathcal{S}}$. The (multi-connected, smooth) boundary between the pore space $\hat{\mathcal{P}}$ and the solid skeleton $\hat{\mathcal{S}}$ is denoted by $\hat{\Gamma}$.

The pore space $\hat{\mathcal{P}}$ is occupied by a fluid, which contains a solute with concentration $\hat{c}(\hat{\mathbf{x}}, \hat{t})$ [mol/L³], where $\hat{\mathbf{x}}$ denotes a point in $\hat{\mathcal{P}}$ and \hat{t} is time. The solute diffuses throughout the pore space $\hat{\mathcal{P}}$ and undergoes a heterogeneous reaction at the solid-fluid interface $\hat{\Gamma}$, both taking place in isothermal conditions. The former process is described by a diffusion equation

$$\frac{\partial \hat{c}}{\partial \hat{t}} = D \hat{\nabla}^2 \hat{c}, \quad \hat{\mathbf{x}} \in \hat{\mathcal{P}}, \quad \hat{t} > 0. \quad (2.1)$$

where D [L²/T] is the diffusion coefficient. The pore spaces considered in our analysis consist of both interconnected nanopores and nanotubes. The diffusive transport in the former is due to molecular diffusion (with molecular diffusion coefficient D_m), while Knudsen diffusion (with diffusion coefficient D_k) might take place in the latter. While the analysis presented below is capable of handling spatially variable and anisotropic diffusion coefficients, we use the constant diffusion coefficient D to simplify the presentation.

Mass conservation along the impermeable solid-fluid interface $\hat{\Gamma}$ requires the normal component of the solute mass flux $-D\hat{\nabla}\hat{c}$ to be balanced by the rate of change in the adsorbed solute \hat{q} , i.e.,

$$-D\mathbf{n} \cdot \hat{\nabla}\hat{c} = \frac{\partial \hat{q}}{\partial \hat{t}} = \hat{q}_m \frac{\partial \hat{s}}{\partial \hat{t}}, \quad \hat{\mathbf{x}} \in \hat{\Gamma}, \quad \hat{t} > 0, \quad (2.2)$$

where \hat{q} [mol/L²] is the adsorption amount per unit area of the solid-fluid surface $\hat{\Gamma}$, \hat{q}_m [mol/L²] is the maximal adsorption amount, $\hat{s}(\hat{\mathbf{x}}, \hat{t})$ [-] is the fractional coverage of $\hat{\Gamma}$, and $\mathbf{n}(\mathbf{x})$ is the unit normal vector of $\hat{\Gamma}$. Equation (2.1) is also subject to an initial condition $\hat{c}(\mathbf{x}, 0) = c_{\text{in}}$, in which the initial concentration c_{in} assumed to be spatially uniform. Finally, appropriate boundary conditions are imposed on the bounding surface of the nanoporous material $\hat{\Omega}$.

Previous efforts to derive effective (continuum-scale) descriptions of processes, which admit the pore-scale representation (2.1) and (2.2), dealt with either equilibrium adsorption[79, 36] or general non-equilibrium adsorption described by a coupled system of reaction-diffusion equations for \hat{c} and \hat{s} [30, 94, 99, 4, 15]. While the former are not applicable for many nanoporous phenomena, the latter are too complex to be used in materials design. Instead, we derive a reduced-complexity model based on the Lagergren (pseudo-first-order) rate equation,[53, 74, 41, 57]

$$\frac{d\hat{s}}{d\hat{t}} = \gamma(\hat{s}_{\text{eq}} - \hat{s}), \quad (2.3)$$

where γ [T⁻¹] is the first-order adsorption rate constant, and \hat{s}_{eq} is the adsorption coverage fraction at equilibrium. The latter is assumed to follow the Langmuir

adsorption isotherm,

$$\hat{s}_{\text{eq}} = \frac{\hat{K}\hat{c}}{1 + \hat{K}\hat{c}}, \quad (2.4)$$

where \hat{K} [L³/mol] is the adsorption equilibrium constant. The derivation of the reduced-complexity model is facilitated by rewriting this pore-scale boundary-value problem (BVP) in the dimensionless form. Let us introduce dimensionless variables and parameters

$$\mathbf{x} = \frac{\hat{\mathbf{x}}}{L}, \quad t = \frac{D\hat{t}}{L^2}, \quad c = \frac{\hat{c}}{c_{\text{in}}}, \quad q_{\text{m}} = \frac{\hat{q}_{\text{m}}}{Lc_{\text{in}}}, \quad K = \hat{c}_{\text{in}}\hat{K}, \quad \text{Da} = \frac{L^2\gamma}{D} \quad (2.5)$$

where the Damköhler number Da represents the ratio of reaction and diffusion time-scales. We show in Appendix A that, for nanoporous materials characterized by $\text{Da} \ll 1$, Eqs. (2.2)–(2.4) give rise to a nonlinear (but decoupled) boundary condition at the solid-fluid interface Γ ,

$$-\mathbf{n} \cdot \nabla c = \text{Da } q_{\text{m}} \frac{Kc}{1 + Kc}, \quad \mathbf{x} \in \Gamma, \quad t > 0. \quad (2.6a)$$

The remainder of the pore-scale BVP takes the form of a diffusion equation

$$\frac{\partial c}{\partial t} = \nabla^2 c, \quad \mathbf{x} \in \mathcal{P}, \quad t > 0 \quad (2.6b)$$

subject to the initial condition $c(\mathbf{x}, 0) = 1$ for $\mathbf{x} \in \mathcal{P}$ and the corresponding boundary conditions on the bounding surface of the nanoporous material Ω .

Solving this BVP in a large interconnected network of nanopores \mathcal{P} is neither feasible nor necessary. Instead, one is often interested in the emerging (macroscopic)

properties of the nanoporous material Ω as a whole. While its pore structure is described by diameters and a spatial arrangement of individual nanopores and nanotubes bridges, its macroscopic properties are characterized by bulk (average) quantities such as porosity ϕ , effective diffusion coefficient \mathbf{D}_{eff} , and effective adsorption rate constant γ_{eff} . Connecting these two levels of description allows us to relate such macroscopic properties to the underlying microscopic (pore-scale) characteristics. This, in turn, enables one to manufacture nanoporous materials with desired macroscopic attributes.

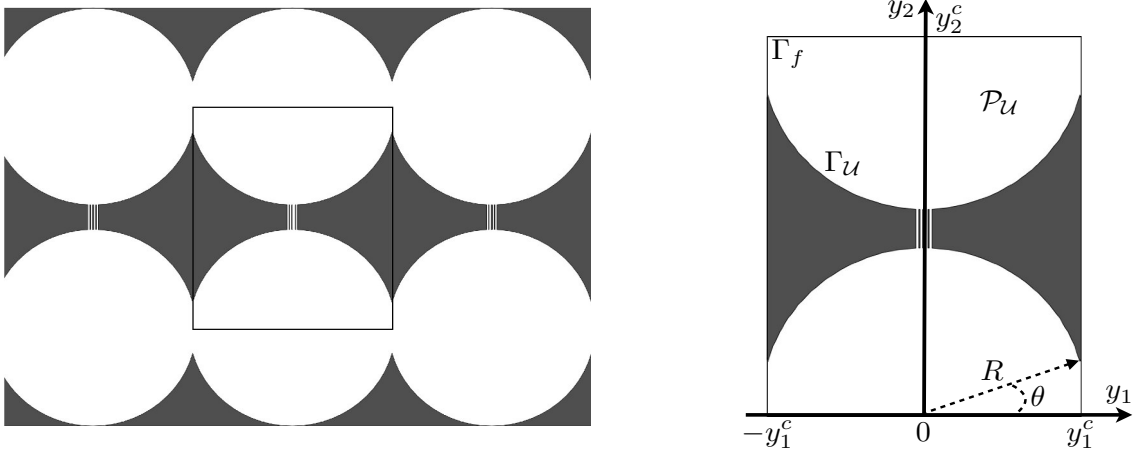


Figure 2.1: A schematic representation of Material 1 (left) and the corresponding unit cell \mathcal{U} (right). The unit cell is a $2y_1^c$ by y_2^c rectangle, with $y_1^c = R \cos \theta$ and $y_2^c = 2R + l$.

By way of example, we consider nanoporous materials in which rows of interconnected uniform nanopores of radius R are bridged by regularly placed microporous tubes. The spacing between two neighboring pores in a single row is expressed in terms of the angle θ that we refer to as an intersection factor. A number n of microporous tubes (diameter $d = 0.7$ nm) per unit cell is referred to as a microporous tube density. In the first class of materials, the rows of interconnected nanopores are perfectly aligned (Fig. 2.1). In the second, the rows are shifted relative to each other by the distance $R/2$ (Fig. 2.6). These two settings provide an adequate representation of the

nanoporous materials[63].

2.4 Macroscopic properties of nanoporous materials

Macroscopic representations of a nanoporous material Ω treat it as a continuum, without separating it into the pore space \mathcal{P} and the solid skeleton \mathcal{S} . Macroscopic solute concentration $C(\mathbf{x}, t)$ —the microscopic concentration $c(\mathbf{y}, t)$ averaged over a (representative elementary) volume V centered at point $\mathbf{x} \in \Omega$ —is defined as

$$C(\mathbf{x}, t) \equiv \frac{1}{\|\mathcal{P}_V\|} \int_{\mathcal{P}_V(\mathbf{x})} c(\mathbf{y}, t) d\mathbf{y} \quad (2.7)$$

where $\|\mathcal{P}_V\|$ is the total volume of pores contained in V .

We show in Appendix E that, for nanoporous materials composed of periodic arrangements of unit cells \mathcal{U} , the macroscopic concentration $C(\mathbf{x}, t)$ satisfies a reaction-diffusion equation

$$\frac{\partial C}{\partial t} = \phi^{-1} \nabla \cdot (\mathbf{D}_{\text{eff}} \nabla C) - \gamma_{\text{eff}} q_{\text{m}} \frac{KC}{1 + KC} \quad (2.8)$$

where $\phi \equiv \|\mathcal{P}_V\|/\|V\| = \|\mathcal{P}_{\mathcal{U}}\|/\|\mathcal{U}\|$ is the porosity (with $\mathcal{P}_{\mathcal{U}}$ denoting the pore space of the unit cell \mathcal{U}); the effective reaction constant γ_{eff} is related to $\|\Gamma_V\|$, the total surface area of the pores contained in V , (or to $\|\Gamma_{\mathcal{U}}\|$, the total surface area of the pores contained in \mathcal{U}), by

$$\gamma_{\text{eff}} = \frac{\|\Gamma_V\|}{\|\mathcal{P}_V\|} = \frac{\|\Gamma_{\mathcal{U}}\|}{\|\mathcal{P}_{\mathcal{U}}\|}; \quad (2.9)$$

and the effective diffusion tensor \mathbf{D}_{eff} defined as

$$\mathbf{D}_{\text{eff}} = \frac{D}{\|\mathcal{U}\|} \int_{\mathcal{P}_{\mathcal{U}}} (\mathbf{I} + \nabla_{\mathbf{y}} \boldsymbol{\chi}) d\mathbf{y}. \quad (2.10)$$

Here \mathbf{I} is the identity matrix, and the “closure variable” $\boldsymbol{\chi}(\mathbf{y})$ is a \mathcal{U} -periodic vector defined on $\mathcal{P}_{\mathcal{U}}$. It satisfies

$$\nabla_{\mathbf{y}}^2 \boldsymbol{\chi} = \mathbf{0}, \quad \mathbf{y} \in \mathcal{P}_{\mathcal{U}}; \quad \langle \boldsymbol{\chi}(\mathbf{y}) \rangle \equiv \frac{1}{\|\mathcal{U}\|} \int_{\mathcal{P}_{\mathcal{U}}} \boldsymbol{\chi}(\mathbf{x}) d\mathbf{y} = \mathbf{0} \quad (2.11)$$

subject to the boundary condition along the fluid-solid segments $\Gamma_{\mathcal{U}}$ of the boundary of $\mathcal{P}_{\mathcal{U}}$,

$$\mathbf{n} \cdot \nabla_{\mathbf{y}} \boldsymbol{\chi} = -\mathbf{n} \cdot \mathbf{I}, \quad \mathbf{y} \in \Gamma_{\mathcal{U}}. \quad (2.12)$$

Along the remaining (“fluid”) segments Γ_f of the boundary of $\mathcal{P}_{\mathcal{U}}$ (see Fig. 2.1) the \mathcal{U} -periodicity of $\boldsymbol{\chi}(\mathbf{x})$ is enforced. Accounting for the normalization condition $\langle \boldsymbol{\chi}(\mathbf{y}) \rangle = \mathbf{0}$, in the case of the rectangular unit cell \mathcal{U} (Fig. 2.1) this yields

$$\chi_1(-y_1^c, y_2) = \chi_1(y_1^c, y_2) = 0, \quad \frac{\partial \chi_1}{\partial y_2}(y_1, 0) = \frac{\partial \chi_1}{\partial y_2}(y_1, y_2^c) = 0 \quad (2.13a)$$

and

$$\chi_2(y_1, 0) = \chi_2(y_1, y_2^c) = 0, \quad \frac{\partial \chi_2}{\partial y_1}(-y_1^c, y_2) = \frac{\partial \chi_2}{\partial y_1}(y_1^c, y_2) = 0. \quad (2.13b)$$

Here $y_1^c = R \cos \theta$ and $y_2^c = 2R + l$. Figure 2.2 exhibits a numerical solution $\boldsymbol{\chi}(\mathbf{y}) = (\chi_1, \chi_2)^\top$ of the BVP (2.11)–(2.13) defined on $\mathcal{P}_{\mathcal{U}}$ in Fig. 2.1. This solution and all

the numerical results reported below are obtained with COMSOL.

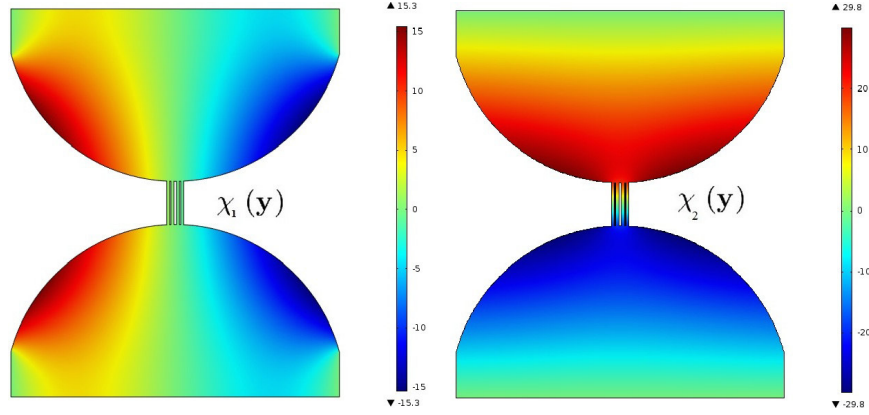


Figure 2.2: The horizontal χ_1 (left) and vertical χ_2 (right) components of the closure variable $\boldsymbol{\chi}(\mathbf{y}) = (\chi_1, \chi_2)^\top$ defined on the fluid-domain $\mathcal{P}_{\mathcal{U}}$ of the unit cell \mathcal{U} in Fig. 2.1. In this example, the four vertical nanobridges are spaced $\Delta = 0.3$ nm apart.

2.5 Simulation results

The upscaled relations derived above allow one to infer macroscopic properties of a nanomaterial, e.g., the (effective) anisotropic diffusion coefficient \mathbf{D}_{eff} and the effective reaction constant γ_{eff} , from its microscopic characteristics. Unless specified otherwise, the subsequent simulations deal with the effects of these microscopic parameters on the macroscopic properties of Material 1 (Fig. 2.1). The external concentration gradient is applied in the x_1 direction.

Nanopore radius in isolated nanotunnels. In the absence of nanobridges ($n = 0$), diffusion through the nanoporous Material 1 (Fig. 2.1) occurs only in the x direction along the disconnected nanotunnels. The latter consist of stacked nanopores of uniform radius R , which varies from $R = 20$ nm to 60 nm. The effective (macroscopic)

longitudinal diffusion coefficient D_{11} , normalized by molecular diffusion coefficient D , and the effective reaction constant γ_{eff} are shown in Fig. 2.3; the transverse diffusion coefficient is $D_{22} = 0$. The effective diffusion coefficient D_{11} increases with pore radius R and intersection angle θ . The reaction constant γ_{eff} decreases with both.

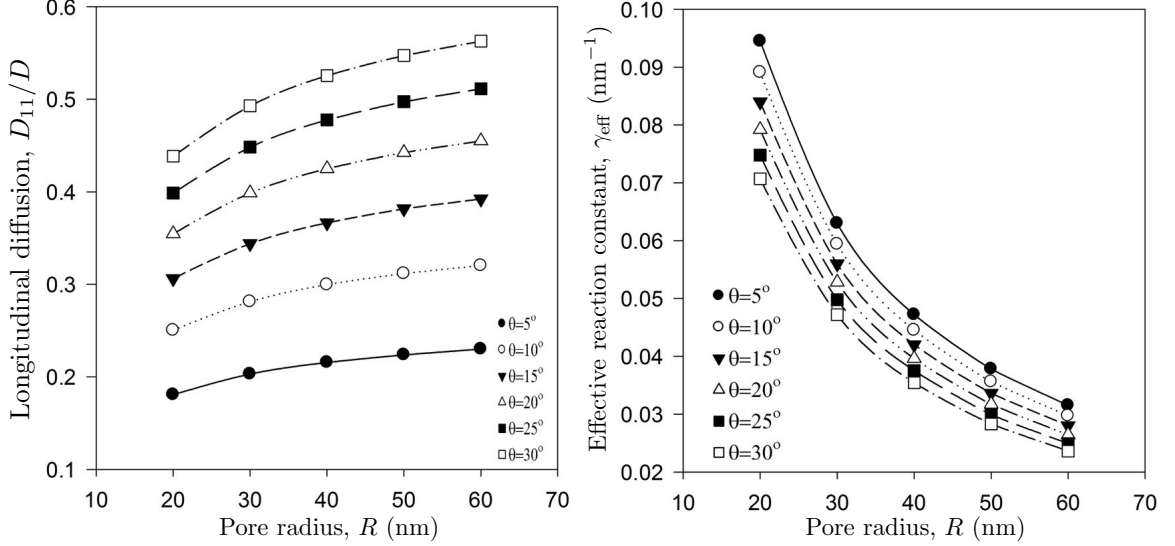


Figure 2.3: Dependence of effective longitudinal diffusion coefficient D_{11} (left) and effective reaction constant γ_{eff} (right) on pore radius R and intersection angle θ .

Intersection angle θ . Intersection angle θ quantifies the distance between the centers of any two adjacent spherical pores in a given nanotunnel (Fig.2.1), such that θ decreases as this distance increases. Figure 2.4 exhibits the impact of θ on the effective properties of Material 1 (Fig.2.1), in which nanotunnels composed of pores of radius $R = 40$ nm are connected by microporous tubes of length $l = 10$ nm. As θ increases, the throats between the adjacent pores become large, giving rise to a significant increase in the longitudinal component of the effective diffusion tensor (D_{11}). The impact of θ on both the transverse diffusion (D_{22}) and the effective reaction constant (γ_{eff}) is less pronounced. A slight ($\approx 3\%$) increase of the longitudinal

diffusion coefficient D_{11} caused by the addition of $n = 10$ nanotubes is due to the rise in the material's connectivity and porosity. Despite their negligible contribution to the porosity of this nanoporous material, the microporous tube bridges significantly alter its diffusive properties, giving rise to the non-zero transverse diffusion coefficient D_{22} . They also nearly double the effective reaction constant γ_{eff} .

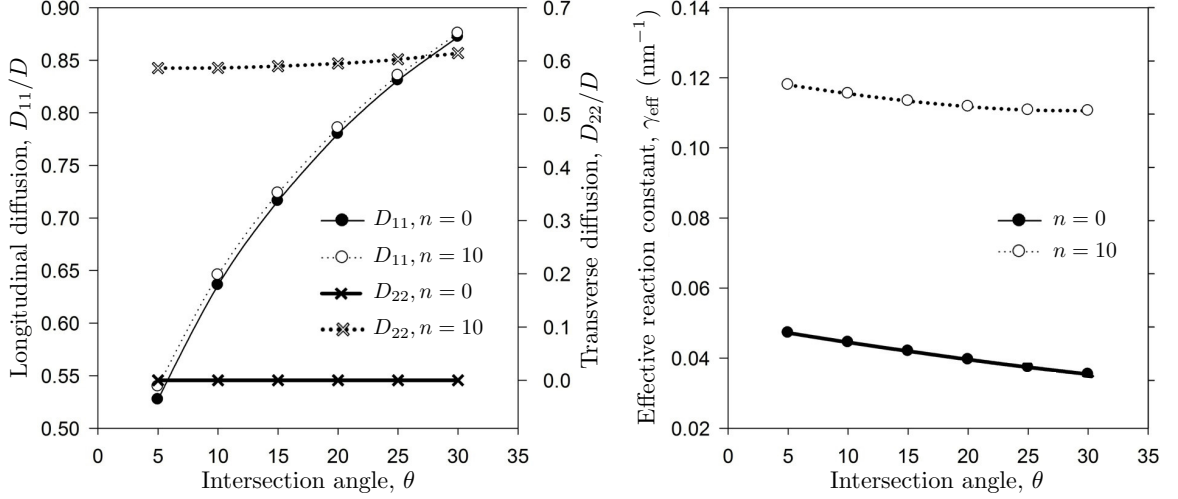


Figure 2.4: Dependence of the longitudinal (D_{11}) and transverse (D_{22}) components of the effective diffusion tensor (left) and effective reaction constant γ_{eff} (right) on intersection angle θ , for materials with disconnected ($n = 0$) and interconnected (by $n = 10$ microporous tubes) nanotunnels. The latter are composed of pores with uniform radius $R = 40$ nm.

Nanobridge density. This numerical experiment deals with nanotunnels formed by pores of radius $R = 40$ nm, which are intersected at angle $\theta = 20^\circ$; the neighboring nanotunnels are connected by microporous tubes of length $l = 10$ nm. In the simulations reported below we set the distance between individual microporous tubes to either $\Delta = 1.4$ nm or $\Delta = 0.3$ nm. For the given microporous tube length of $l = 10 \sim 11$ nm and $\Delta = 0.3$ nm, the maximum possible number of microporous tubes in the unit cell is $n_{\text{max}} = 10$. If no limits are placed on the microporous tube length (i.e., if it is allowed to vary between $l = 10 \sim 50$ nm), then placing microporous

tubes $\Delta = 1.4$ nm apart would allow for the maximum number of microporous tubes in the unit cell is $n_{\max} = 34$. The behavior of the effective transport properties of these nanoporous materials as a function of nanobridge density is shown in Fig. 2.5. While the number of microporous tubes in a bridge, n , does not appreciably affect the material's diffusive properties (D_{11} and D_{22}), it significantly influences its adsorbing capacity (γ_{eff}).

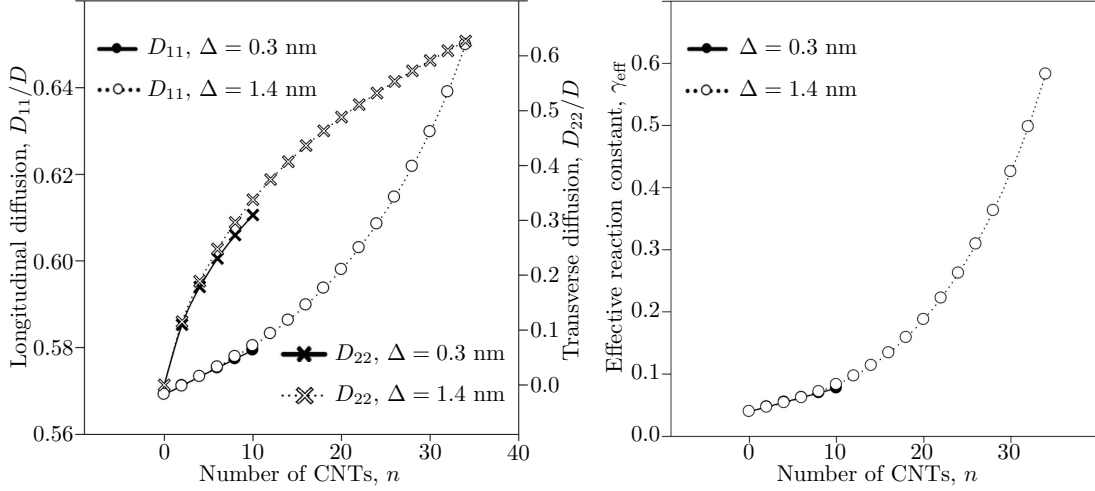


Figure 2.5: Dependence of the longitudinal (D_{11}) and transverse (D_{22}) components of the effective diffusion tensor (left) and effective reaction constant γ_{eff} (right) on the number of microporous tubes (n) comprising the nanobridges between the neighboring nanotunnels. The latter are composed of pores with uniform radius $R = 40$ nm, which are intersected at angle $\theta = 20^\circ$.

Alternative material topology. To investigate the effects of spatial arrangement of nanotunnels and nanobridges comprising a nanoporous material, we consider the second class of materials (Material 2 in Fig. 2.6). The neighboring nanotunnels in these materials are shifted by $R/2$, while in Material 1 (Fig. 2.1) they are aligned.

For a given structure of the nanotunnels (e.g., the pore radius $R = 40$ nm and the intersection angle $\theta = 20^\circ$) and nanobridges (e.g., the microporous tube spacing

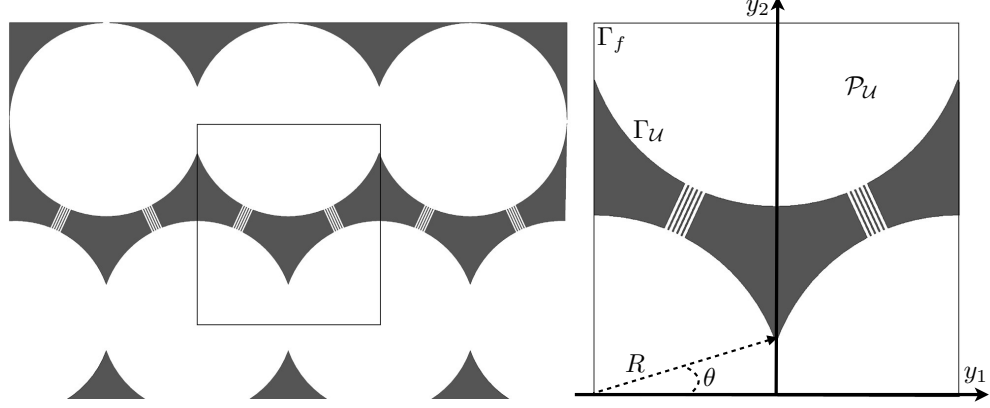


Figure 2.6: A schematic representation of Material 2 and the corresponding unit cell \mathcal{U} (right).

$\Delta = 1.4$ nm and the number of microporous tubes n), Eq. (2.9) suggests that Materials 1 and 2 have the same adsorbing capacity (the effective reaction constant γ_{eff}). The topologic differences between the two materials manifest themselves in the macroscopic diffusive properties (Fig. 2.7). Material 2 possesses the higher longitudinal diffusion coefficient (D_{11}) that is significantly more sensitive to the number of microporous tubes in the nanobridge; the transverse diffusion coefficients (D_{22}) of the two materials are practically the same. Although not shown here, a local distribution of microporous tubes within a unit cell also affects a material's diffusive properties. A symmetric arrangement of nanobridges, which consists of an equal number of nanotubes arranged at acute and obtuse angles (as in Fig. 2.6), yields the higher values of D_{11} and D_{22} than its asymmetric counterpart, in which only the left or the right bridge is present, does.

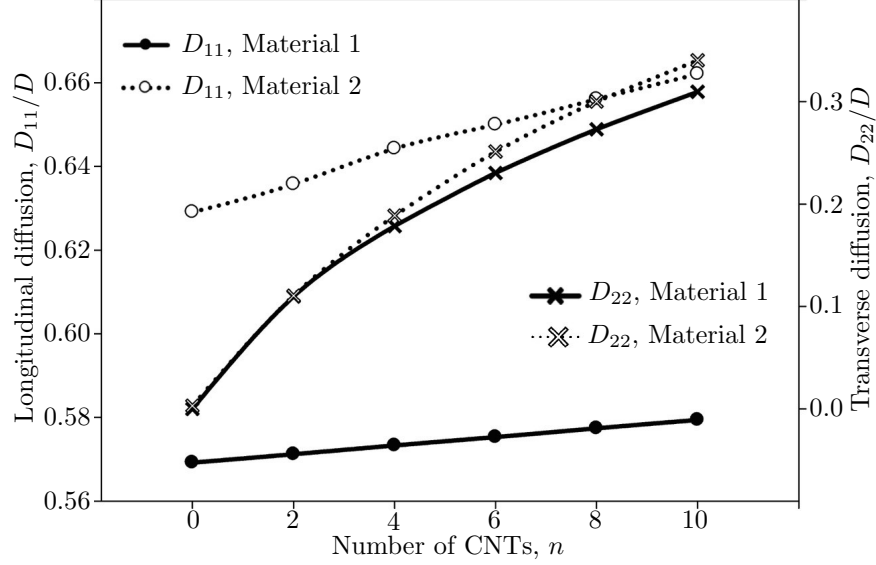


Figure 2.7: Dependence of the longitudinal (D_{11}) and transverse (D_{22}) components of the effective diffusion tensor on the number of microporous tubes (n) for Materials 1 and 2. In both materials, pores of uniform radius $R = 40$ nm are intersected at angle $\theta = 20^\circ$.

2.6 Conclusions

Modern technological advances have enabled one to manufacture nanoporous materials with a prescribed pore structure. This raises a possibility of using controllable pore-scale parameters (e.g., pore size and connectivity) to design materials with desired macroscopic properties (e.g., diffusion coefficient and adsorption capacity). By relating these two scales, the homogenization theory (or other upscaling techniques) provides a means of guiding the experimental design. To demonstrate this approach, we consider a class of nanoporous materials whose pore space consists of nanotunnels interconnected by carbon nanotubes (microporous tubes). We express the anisotropic diffusion coefficient and adsorption coefficient of such materials in terms of the tunnels' properties (pore radius and inter-pore throat width) and their connectivity (spacing between the adjacent tunnels and microporous tube-bridge density). Our analysis

leads to the following major conclusions.

1. Upscaling (e.g., by means of the homogenization theory) provides a general framework for optimal design of nanoporous materials. In the case of adsorption-diffusion systems, this approach provides a venue for manufacturing nanoporous materials with desired anisotropic diffusion coefficient \mathbf{D}_{eff} and reaction constant γ_{eff} , which can be used, for example, in the design of filters.
2. Intersection angle θ quantifies the distance between the centers of any two adjacent spherical pores in a given nanotunnel. As θ increases, the throats between the adjacent pores become large, giving rise to a significant increase in the longitudinal component of the effective diffusion tensor (D_{11}). The impact of θ on both the transverse diffusion (D_{22}) and the effective reaction constant (γ_{eff}) is less pronounced.
3. Despite their negligible contribution to the porosity of this nanoporous material, the microporous tube bridges significantly alter its diffusive properties, giving rise to the non-zero transverse diffusion coefficient D_{22} . They also nearly double the effective reaction constant γ_{eff} .
4. While the number of microporous tubes in a bridge, n , does not appreciably affect the material's diffusive properties (D_{11} and D_{22}), it significantly influences its adsorbing capacity (γ_{eff}).

2.7 Acknowledgements

This research was supported in part by Air Force Office of Scientific Research (DE-FG02-07ER25815) and National Science Foundation (EAR-1246315).

This Chapter is a reprint of the material as it appeared in: Zhang, X., Urita, K., Moriguchi, I. and Tartakovsky, D.M., 2015. Design of nanoporous materials with optimal sorption cpacity. Journal of Applied Physics, 117(24), p.244304. The dissertation author was the primary investigator and author on this paper.

Chapter 3

Effective Ion Diffusion in Charged Nanoporous Materials

3.1 Abstract

Multiscale models of ion transport in porous media relate microscopic material properties (e.g., pore size distribution, pore connectivity and tortuosity) to their macroscopic counterparts (e.g., porosity, effective diffusion coefficient and effective electrical conductivity). We derive a macroscopic model of ion transport in electrically charged nanoporous materials, and the corresponding effective diffusion coefficient, electric conductivity and transference numbers, that explicitly account for dynamic changes in electrical double layer (EDL) and possible overlap of EDLs in nanopores. The general equations comprising this model reduce to a model of an electrical double layer capacitor (EDLC) used to interpret measurements of the EDLC's voltage response to charging. While the original model relies on empirical coefficients (e.g., Bruggeman's relation), our effective coefficients are derived from the first principles

and vary with a range of electrochemical conditions (e.g., initial concentration of ions in the electrolyte). The resulting model predictions of the EDLC voltage response match the experimental data better than the original model does.

3.2 Introduction

Rapid growth of the global economy, depletion of fossil fuels, and increasing environmental concerns accelerate the shift to renewable (e.g., solar and wind) energy production and electric and/or hybrid electric vehicles with low CO₂ emissions. These and other applications rely on energy conversion and storage technologies. Some of the most effective and practical technologies for electrochemical energy conversion and storage are batteries, fuel cells, and electrochemical supercapacitors. Their performance needs to substantially improve in order to meet power density and energy density demands. This requires breakthroughs in our understanding of electrochemical phenomena at the nanoscale and ability to model these processes at the device scale, and parlaying them into design of new materials and devices.

Nanoscale pore-structure of, e.g., electrodes affects energy storage through formation of electrical double layer (EDL) at the solid material/electrolyte interfaces [61, 19, 25, 23, 89]. EDL formation plays an important role in other physical, chemical and biological systems, including separation processes used to remove heavy metals from aqueous solutions, groundwater remediation mediated by electrosorption, and capacitive desalination [70].

Nanoporous materials with a hierarchical porous structure are thought to possess attractive electrosorption and capacitance characteristics due to their large specific surface area (provided by micropores) and fast transport (facilitated by

mesopores) [69]. However, their large surface areas do not always translate into more energy stored on the surface, because the local electrical potential formation can both dominate ion transport and sorption inside nanopores and restrict pore accessibility. For example, poor electrochemical accessibility of micropores was found to significantly reduce the extent of surface reactions between the electrode material and electrolyte [97, 55]. This suggests that the porous structure of a nanoporous material controls power density and accessibility to the energy stored on the interface.

Qualitative understanding and quantitative predictions of this phenomenon and, more specifically, the effects of EDL on ion transport are a prerequisite for bottom-up design of new nanoporous metamaterials [110]. Guided by the goal of maximizing an electrode’s specific surface area accessible to electrolyte, an optimal design of such materials must account for the potential overlap of EDLs in nanoporous structures saturated with a very dilute solution, which decreases not only the ion transport rate but also the equilibrium concentration of ions inside the pores. Such design strategies are guided by mathematical models that relate microscopic material properties (e.g., pore size distribution, pore connectivity and tortuosity) to their macroscopic counterparts (e.g., porosity, effective diffusion coefficient and effective electrical conductivity).

A commonly used approach is to postulate the equivalency of mathematical descriptors on the pore and continuum scales and to use phenomenological relations to express coefficients of the continuum-scale equations in terms of their pore-scale counterparts. For instance, a diffusion process taking place within the pore network of a porous electrode might be described by diffusion equations at both scales, and the molecular diffusion coefficient D in the pore-scale equation is replaced at the

continuum scale with an assumed effective diffusion coefficient $D^{\text{eff}} = \omega D / \tau$, where ω and τ are the material’s porosity and tortuosity, respectively, often supplemented with Bruggeman’s relation [24] $\tau = \omega^{-1/2}$. This widely-used expression for estimation of effective properties in electrochemical systems is thought to be applicable for materials with low porosity, connected electrolyte transport paths, and spherical electrode particles [37]. Many porous electrode metamaterials and local electrical conditions (electrolyte concentration and applied electric field) do not satisfy these conditions, undermining the veracity of the Bruggeman model (as we demonstrate in this study) or, at least, the value of its exponent [24, 91].

Derivation of more rigorous models often relies on homogenization, e.g., via multiple-scale expansions. For example, it was used to derive macroscopic Poisson-Nernst-Planck (PNP) equations under assumptions of either a fixed surface charge density on the solid matrix [83] or an infinitely thin EDL [17]; to obtain macroscopic Onsager’s reciprocal relations from a linearized version of PNP equations [58]; and to derive a macroscopic PNP-based model of water flow and ion transport in geological deformable porous media [54, 68, 66, 65]. In addition to providing a map between the microscopic and macroscopic parameters and processes, homogenization establishes both the rigorous macroscopic descriptors grounded in the first principles and the limits of applicability of macroscopic models [38]. The homogenization analyses mentioned above are grounded in physical limitations: the assumption of a fixed surface charge density translates into an upscaled Poisson equation that does not contain information about the local electric potential distribution [83] and is not applicable for electrochemical processes in which zeta potential and solution concentration change in response to charging/discharging [66, 65].

In contrast to these and other similar studies (e.g., [92]) we derive a macroscopic model of ion transport in electrically charged nanoporous materials, and the corresponding effective diffusion coefficient, electric conductivity and transference numbers, that explicitly account for dynamic changes in the EDL. Our model goes beyond the infinitely thin EDL approximation and, hence, accounts for possible overlap of EDLs in nanopores. The general equations comprising this model reduce to a model of an electrical double layer capacitor (EDLC) used to interpret measurements of the EDLC's voltage response to charging [96]. While the original model [96] relies on empirical coefficients, such as $D^{\text{eff}} = \omega D / \tau$ or its Bruggeman's analog $D^{\text{eff}} = \omega^{3/2} D$, our effective coefficients are derived from the first principles and vary with electrochemical conditions (e.g., initial concentration of ions in the electrolyte). The resulting model predictions of the EDLC voltage response match the experimental data [96] better than the original model did.

3.3 Problem Description

We consider a hierarchical porous material Ω with a characteristic length L . Let \mathcal{P} denote the part of this material occupied by nanopores whose characteristic length scale, e.g., a typical pore diameter, is l such that $\epsilon \equiv l/L \ll 1$. The impermeable solid skeleton \mathcal{S} occupies the rest of the nanoporous material, i.e., $\Omega = \mathcal{P} \cup \mathcal{S}$. The (multi-connected, smooth) boundary between the pore space \mathcal{P} and the solid skeleton \mathcal{S} is denoted by Γ .

The pore space \mathcal{P} is completely occupied by an ionized fluid, in which cations and anions have concentrations $c_+(\mathbf{x}, t)$ and $c_-(\mathbf{x}, t)$, respectively; these concentrations have units $[\text{mol}/\text{L}^3]$, and vary both in space, $\mathbf{x} \in \mathcal{P}$, and time t . Interactions between

the ionized solution and static charges at the solid-fluid interface Γ gives rise to an electrical double layer.

Microscopic models of ion transport through the hierarchical porous material Ω track the spatiotemporal evolution of $c_{\pm}(\mathbf{x}, t)$ inside a complex pore network \mathcal{P} ; they rest on a solid electrochemical foundation but are computationally demanding, and often prohibitively so. Macroscopic models treat the porous material Ω as a continuum, i.e., associate ion concentrations $C_{\pm}(\mathbf{x}, t)$ with a certain (representative elementary) volume of the material, over which the pore-scale concentrations $c_{\pm}(\mathbf{x}, t)$ are averaged; such models are largely phenomenological, but relatively fast to solve. Microscopic and macroscopic formulations are provided below. Establishing the relationship between the two is one of the main goals of this study.

3.3.1 Microscopic transport model

Processes in the fluid-filled pores \mathcal{P} . We adopt the dilute theory of solvents, which treats ions as point charges and defines electrochemical potential [J/mol] as $\mu_{\pm} = \bar{\mu}_{\pm} + RT \ln c_{\pm} + z_{\pm} F \varphi$ where $\bar{\mu}_{\pm}$ is a reference value, and z_{\pm} are the ion charges (valencies) $[-]$. Here R [J/K/mol] and F [C/mol] are the gas and Faraday constants, respectively; T [K] is temperature; and φ [V] is the electric potential. Spatial variability of μ_{\pm} induces ionic (Nernst-Planck) fluxes $\mathbf{J}_{\text{NP}}^{\pm} = -M_{\pm} c_{\pm} \nabla \mu_{\pm}$, where the ion mobility M_{\pm} is related to the molecular diffusion coefficient of ions in the fluid, \mathcal{D}_{\pm} [L²/T], by the Einstein relation $M_{\pm} = \mathcal{D}_{\pm}/RT$. In the absence of homogeneous chemical reactions, mass conservation of anions and cations, $\partial_t c_{\pm} = -\nabla \cdot \mathbf{J}_{\text{NP}}^{\pm}$, gives rise to the

Nernst-Planck equations

$$\frac{\partial c_{\pm}}{\partial t} = \nabla \cdot [\mathcal{D}_{\pm}(\nabla c_{\pm} + c_{\pm} \frac{z_{\pm} F}{RT} \nabla \varphi)], \quad \mathbf{x} \in \mathcal{P}. \quad (3.1)$$

The total (net) ionic charge density $q \equiv F(z_+ c_+ + z_- c_-)$ is related to the electric potential $\varphi(\mathbf{x}, t)$ through a Poisson equation,

$$-\mathcal{E} \nabla^2 \varphi = F(z_+ c_+ + z_- c_-), \quad \mathbf{x} \in \mathcal{P}, \quad (3.2)$$

where \mathcal{E} is dielectric constant of the solvent.

Processes on the fluid-solid interface Γ . Within the electrical double layer (EDL) framework, the electrically charged surface Γ is “coated” with a compact Stern layer comprised of mixture of solvent molecules and a single layer of adsorbed ions. These are effectively immobilized by the interplay of adsorption, van der Waals forces and hydrogen bonding. To simplify the presentation, we assume the thickness of the Stern layer, $\ell_s \sim 0.03$ nm to 0.2 nm (a typical diameter of an ion) [87] to be negligible relative to the characteristic pore size $\ell_p \sim 1.0$ nm (a typical diameter of a micropore) to 25.0 nm (that of a mesopore), so that the Nernst-Planck-Poisson (PNP) equations (3.1)–(3.2) are defined on the whole domain \mathcal{P} and the corresponding boundary conditions are specified on the fluid-solid interface Γ . (The analysis presented below is valid even when this assumption does not hold, in which case the transport domain \mathcal{P} is reduced by the thickness of the Stern layer to \mathcal{P}_- and the interface Γ is replaced with Γ_- , the surface of \mathcal{P}_- .)

Following the standard practice [46, 48], we assume that the surface Γ carries

a constant electric (zeta) potential φ_Γ , which translates into a Dirichlet boundary condition

$$\varphi(\mathbf{x}, t) = \varphi_\Gamma, \quad \mathbf{x} \in \Gamma. \quad (3.3)$$

This assumption is applicable if the solid matrix \mathcal{S} is highly conductive, which occurs, e.g., in carbon aerogels[106]. Heterogeneous chemical reactions, $f_\pm(c_-, c_+)$, at the fluid-solid interface Γ , give rise to Robin boundary conditions

$$-\mathbf{n} \cdot \mathcal{D}_\pm(\nabla c_\pm + c_\pm \frac{z_\pm F}{RT} \nabla \varphi) = f_\pm(c_-, c_+), \quad \mathbf{x} \in \Gamma. \quad (3.4)$$

When the EDL is stably formed, the situation considered in the present analysis, the surface electrosorption reaction reaches equilibrium, $f_\pm \equiv 0$. This implies the absence of the net local current source.

EDL-explicit decomposition. The remaining part of the EDL consists of a diffusive layer, in which the EDL potential $\varphi_{\text{EDL}}(\mathbf{x}, t)$ decays rapidly with the distance from the charged surface Γ . Depending on a pore's size, this diffusive layer can either occupy the entire pore space or coexist with an electrically neutral ($c_+/\nu_+ = c_-/\nu_- \equiv c_b$, where ν_\pm are the dissociation coefficients) bulk electrolyte[70] present in the pore's core. This suggests a decomposition of the unknown electric potential $\varphi(\mathbf{x}, t)$ into the sum[18]

$$\varphi = \varphi_{\text{EDL}} + \varphi_b. \quad (3.5)$$

It follows from (3.2) and the electroneutrality condition that the bulk electric potential $\varphi_b(\mathbf{x}, t)$ satisfies

$$\nabla^2 \varphi_b = 0, \quad \mathbf{x} \in \mathcal{P}; \quad \varphi_b = 0, \quad \mathbf{x} \in \Gamma; \quad (3.6)$$

and is driven by an externally imposed (macroscopic) potential gradient.

Thermodynamic equilibrium between the EDL and electrolyte's core requires the equality of their respective chemical potentials μ_{\pm} and $\mu_{b\pm}$. Recalling the definition of chemical potential, this yields $z_{\pm}F\varphi + RT \ln c_{\pm} = z_{\pm}F\varphi_b + \nu_{\pm}RT \ln c_b$. Combining this with the decomposition (3.5) yields a Boltzmann distribution for ion concentrations in the EDL,

$$c_{\pm} = \nu_{\pm} c_b \exp \left(-\frac{z_{\pm}F}{RT} \varphi_{\text{EDL}} \right). \quad (3.7)$$

Relations (3.5) and (3.7) transform dependent variables $\varphi(\mathbf{x}, t)$, $c_+(\mathbf{x}, t)$ and $c_-(\mathbf{x}, t)$ into new unknowns $\varphi_{\text{EDL}}(\mathbf{x}, t)$, $\varphi_b(\mathbf{x}, t)$ and $c_b(\mathbf{x}, t)$. Substituting these relations into (3.1) and (3.4) gives transformed Nernst-Planck equations

$$\frac{\partial}{\partial t} \left(c_b e^{-\frac{z_{\pm}F}{RT} \varphi_{\text{EDL}}} \right) = \nabla \cdot \left[\mathcal{D}_{\pm} e^{-\frac{z_{\pm}F}{RT} \varphi_{\text{EDL}}} \left(\nabla c_b + \frac{z_{\pm}F}{RT} c_b \nabla \varphi_b \right) \right], \quad \mathbf{x} \in \mathcal{P} \quad (3.8a)$$

subject to the boundary conditions

$$\mathbf{n} \cdot \left(\nabla c_b + \frac{z_{\pm}F}{RT} c_b \nabla \varphi_b \right) = 0, \quad \mathbf{x} \in \Gamma. \quad (3.8b)$$

Substituting (3.5) and (3.7) into (3.2) and (3.3), while accounting for (3.6), leads to a

Poisson-Boltzmann equation

$$-\nabla^2 \varphi_{\text{EDL}} = \frac{F}{\mathcal{E}} c_{\text{b}} \left(\nu_+ z_+ e^{-\frac{z_+ F}{RT} \varphi_{\text{EDL}}} + \nu_- z_- e^{-\frac{z_- F}{RT} \varphi_{\text{EDL}}} \right), \quad \mathbf{x} \in \mathcal{P} \quad (3.9a)$$

subject to the boundary condition

$$\varphi_{\text{EDL}} = \varphi_{\Gamma}, \quad \mathbf{x} \in \Gamma. \quad (3.9b)$$

This formulation of the PNP equations we proposed in [18] and subsequently used to upscale fluid flow in clays [65, 66, 68].

To simplify the presentation, we set $\mathcal{D}_- = \mathcal{D}_+ \equiv \mathcal{D}$ and consider symmetric completely dissociated electrolyte ions, i.e., assume the equality of the ion charges (valency), $z_+ = -z_- \equiv z$, and dissociation constants, $\nu_+ = \nu_- \equiv \nu$. However, the methodology developed below is equally applicable to multicomponent and/or asymmetric electrolytes.

Non-dimensional formulation. The subsequent analysis is facilitated by introducing, in addition to $\epsilon = l/L$, dimensionless variables

$$\hat{\mathbf{x}} = \frac{\mathbf{x}}{L}, \quad \hat{t} = \frac{t\mathcal{D}}{L^2}, \quad \hat{\nabla} = L\nabla, \quad \hat{c}_{\text{b}} = \frac{c_{\text{b}}}{c_{\text{in}}}, \quad \hat{\varphi} = \frac{F\varphi}{RT}, \quad (3.10)$$

where c_{in} is the initial ion concentration, and rewriting (3.11) and (3.12) in dimensionless form:

$$\frac{\partial}{\partial \hat{t}} (\hat{c}_{\text{b}} e^{\mp z \hat{\varphi}_{\text{EDL}}}) = \hat{\nabla} \cdot \left[e^{\mp z \hat{\varphi}_{\text{EDL}}} (\hat{\nabla} \hat{c}_{\text{b}} \pm z \hat{c}_{\text{b}} \hat{\nabla} \hat{\varphi}_{\text{b}}) \right], \quad \hat{\mathbf{x}} \in \hat{\mathcal{P}} \quad (3.11a)$$

subject to the boundary conditions

$$\hat{\mathbf{n}} \cdot (\hat{\nabla} \hat{c}_b \pm z \hat{c}_b \hat{\nabla} \hat{\varphi}_b) = 0, \quad \hat{\mathbf{x}} \in \hat{\Gamma}; \quad (3.11b)$$

and

$$\epsilon^2 \hat{\nabla}^2 \hat{\varphi}_{\text{EDL}} = \frac{l^2}{\lambda_D^2} \hat{c}_b \sinh(z \hat{\varphi}_{\text{EDL}}), \quad \lambda_D = \sqrt{\frac{RT\mathcal{E}}{2F^2 z \nu c_{\text{in}}}}; \quad \hat{\mathbf{x}} \in \hat{\mathcal{P}} \quad (3.12a)$$

subject to the boundary condition

$$\hat{\varphi}_{\text{EDL}} = \hat{\varphi}_\Gamma, \quad \hat{\mathbf{x}} \in \hat{\Gamma}. \quad (3.12b)$$

In nanoporous materials the Debye length λ_D , a characteristic length of the EDL, is of the same order of magnitude as the characteristic pore size l .

3.3.2 Macroscopic Transport Model

Macroscopic representations of a nanoporous material Ω treat it as a continuum, without separating it into the pore space \mathcal{P} and the solid skeleton \mathcal{S} . In other words, macroscopic ion concentration $C(\mathbf{x}, t)$ and electric potential $\Phi(\mathbf{x}, t)$ are defined at every “point” $\mathbf{x} \in \Omega$. One macroscopic characteristic of such a material is its porosity, $\omega = \|\mathcal{P}\|/\|\Omega\|$. Our goal is to estimate more elusive macroscopic properties, such as an effective diffusion coefficient, which are properties of both a nanoporous material and an electrolyte.

We use the multiple-scale expansion technique [42, 10, 14, 110] to derive effective (macroscopic) counterparts of the PNP equations (3.11) and (3.12). The

method explicitly accounts for the spatial variability of ion concentration, and other dependent variables, on both macroscopic scale (across the porous material, denoted by the coordinate \mathbf{x}) and microscopic scale (inside individual pores, denoted by the coordinate \mathbf{y}). We assume that the bulk concentration and potential exhibit pronounced variability on both scales, i.e., $c_b = c_b(\mathbf{x}, \mathbf{y}, t)$ and $\varphi_b = \varphi_b(\mathbf{x}, \mathbf{y}, t)$; while the spatial variability of the EDL potential is confined to the nanoscale, i.e., $\varphi_{\text{EDL}} = \varphi_{\text{EDL}}(\mathbf{y}, t)$.

The latter assumption enables one to decouple equations (3.11) and (3.12), and to compute $\varphi_{\text{EDL}}(\mathbf{y})$ by solving (3.12) on a “unit cell” \mathcal{U} representative of the material’s pore structure,

$$\hat{\nabla}^2 \hat{\varphi}_{\text{EDL}} = \frac{l^2 \hat{c}_b^*}{\epsilon^2 \lambda_D^2} \sinh(z \hat{\varphi}_{\text{EDL}}), \quad \hat{\mathbf{y}} \in \hat{\mathcal{P}}_{\mathcal{U}}; \quad \hat{\varphi}_{\text{EDL}} = \hat{\varphi}_{\Gamma}, \quad \hat{\mathbf{x}} \in \hat{\Gamma}_{\mathcal{U}} \quad (3.13)$$

where c_b^* is a characteristic ion concentration in the system, e.g., its initial or average value; and $\hat{\mathcal{P}}_{\mathcal{U}}$ and $\hat{\Gamma}_{\mathcal{U}}$ are the pore space and fluid-solid interface contained in the unit cell \mathcal{U} . Then, (3.11) is upscaled in Appendix C to yield continuum-scale Nernst-Planck equations satisfied by macroscopic ion concentration $C(\mathbf{x}, t)$ and electric potential $\Phi(\mathbf{x}, t)$,

$$\omega \frac{\partial C}{\partial t} = \nabla \cdot [\mathbf{D}_{\pm}^{\text{eff}} (\nabla C \pm \frac{zF}{RT} C \nabla \Phi)]. \quad (3.14)$$

Here the effective diffusion coefficients $\mathbf{D}_{\pm}^{\text{eff}}$ are second-order semi-positive-definite tensors defined by

$$\mathbf{D}_{\pm}^{\text{eff}} = \frac{\mathcal{D}\omega}{G_{\pm}} \int_{\hat{\mathcal{P}}_{\mathcal{U}}} e^{\mp z \hat{\varphi}_{\text{EDL}}} (\mathbf{I} + \nabla_{\mathbf{y}} \mathbf{x}_{\pm}^{\top}) d\mathbf{y}, \quad G_{\pm} = \int_{\hat{\mathcal{P}}_{\mathcal{U}}} e^{\mp z \hat{\varphi}_{\text{EDL}}} d\mathbf{y}, \quad (3.15)$$

where \mathbf{I} is the identity matrix, and the closure variables $\chi_{\pm}(\mathbf{y})$ are \mathcal{U} -periodic vector functions, which are computed as solutions of boundary-value problems

$$\begin{aligned} \nabla_{\mathbf{y}}[e^{\mp z\hat{\varphi}_{\text{EDL}}}(\mathbf{I} + \nabla_{\mathbf{y}}\chi_{\pm}^{\top})] &= \mathbf{0}, \quad \mathbf{y} \in \hat{\mathcal{P}}_{\mathcal{U}}; \quad \mathbf{n}(\mathbf{I} + \nabla_{\mathbf{y}}\chi_{\pm}^{\top}) = \mathbf{0}, \quad \mathbf{y} \in \hat{\Gamma}_{\mathcal{U}}; \\ \int_{\hat{\mathcal{P}}_{\mathcal{U}}} \chi_{\pm} d\mathbf{y} &= \mathbf{0}. \end{aligned} \quad (3.16)$$

A few observations about this general result are in order. First, the effective equations (3.14) are identical to those obtained phenomenologically from the solute material balance considerations [70]. Second, the rigorous derivation of these equations enables one to express the diffusion coefficient tensor (3.15) in terms of the pore structure and electrical double layer potential, as opposed to treating them as fitting parameters. Third, it follows from (3.16) that the off-diagonal elements of the second-rank tensor $\nabla_{\mathbf{y}}\chi_{\pm}^{\top}$ are zeros, i.e., $\partial\chi_{\pm,i}/\partial y_k = 0$ for $i \neq k$. Consequently, the off-diagonal elements of the diffusion tensors $\mathbf{D}_{\pm}^{\text{eff}}$ are zero as well.

By way of example, let us consider a homogeneous isotropic nanoporous material assembled from the unit cell shown in Figure 3.1a. The unit cell's symmetry suggests that $\chi_{\pm,1} = \chi_{\pm,2}$, i.e., $\chi_{\pm}(\mathbf{y}) = \chi_{\pm}(\mathbf{y})(1, 1)^{\top}$. The resulting isotropy of the nanoporous material implies that the diffusion coefficients in (3.15) become scalars, D_{+}^{eff} and D_{-}^{eff} . Figure 3.1b exhibits $\chi(\mathbf{y})$, a solution of the unit cell problem (3.16) with $\varphi_{\Gamma} = 0$ and, hence, $\varphi_{\text{EDL}} = 0$, in the absence of electrical charge on the fluid-solid interface Γ . For charged surfaces ($\varphi_{\Gamma} = 0.3$ V), solutions for the closure variables $\chi_{+}(y_1, y_2)$ and $\chi_{-}(y_1, y_2)$ are shown in Figures 3.1c and 3.1d, respectively. These three solutions demonstrate that the double layer potential φ_{EDL} affects the effective transport properties of nanoporous materials (the size of the pore throats in this

example is 1.5 nm).

This finding is in contrast with often used phenomenological relations such as $\mathcal{D}^{\text{eff}} = \omega D / \tau$, where τ is the tortuosity of a porous medium, which is set to $\tau = \omega^{-0.5}$ in the Bruggeman model[70]. Such expressions are not readily adaptable to anisotropic materials and do not account for EDL's presence in charged nanoporous materials and, hence, for the dependence of \mathcal{D}^{eff} on applied voltage. Figure 3.2 shows the dependence of the normalized effective diffusion coefficient $\mathcal{D}^{\text{eff}}/D$ on porosity ω , predicted with both Bruggeman's relation, $\mathcal{D}^{\text{eff}} = D\omega^{3/2}$, and the weighted harmonic mean (a binary effective diffusion coefficient[70]),

$$\mathcal{D}^{\text{eff}} = \frac{2D_+^{\text{eff}}D_-^{\text{eff}}}{D_+^{\text{eff}} + D_-^{\text{eff}}}, \quad (3.17)$$

of the effective diffusion coefficients D_-^{eff} and D_+^{eff} computed with (3.15). As expected, the discrepancy between the two predictions increases with the surface potential φ_Γ .

The effective model presented above also allows one to estimate an electrode's surface potential φ_Γ , which is generated by applying an external voltage V . This is done by inverting a relationship[43]

$$\varphi_\Gamma = \frac{V}{2} - \varphi_{\text{ecm}} - \frac{\sigma}{C_H}, \quad (3.18)$$

where φ_{ecm} is the electrocapillary maximum, C_H is the Helmholtz capacitance, and σ is the surface charge density. The electrocapillary maximum φ_{ecm} determines a material's resistance to applied voltage, i.e., the applied electrical driving force that has to be exceeded for electrosorption to set in; experiments on carbon aerogel electrodes[106] showed that $0.1 \text{ V} \leq \varphi_{\text{ecm}} \leq 0.25 \text{ V}$. For a dilute solution and low applied voltage 1.2 V,

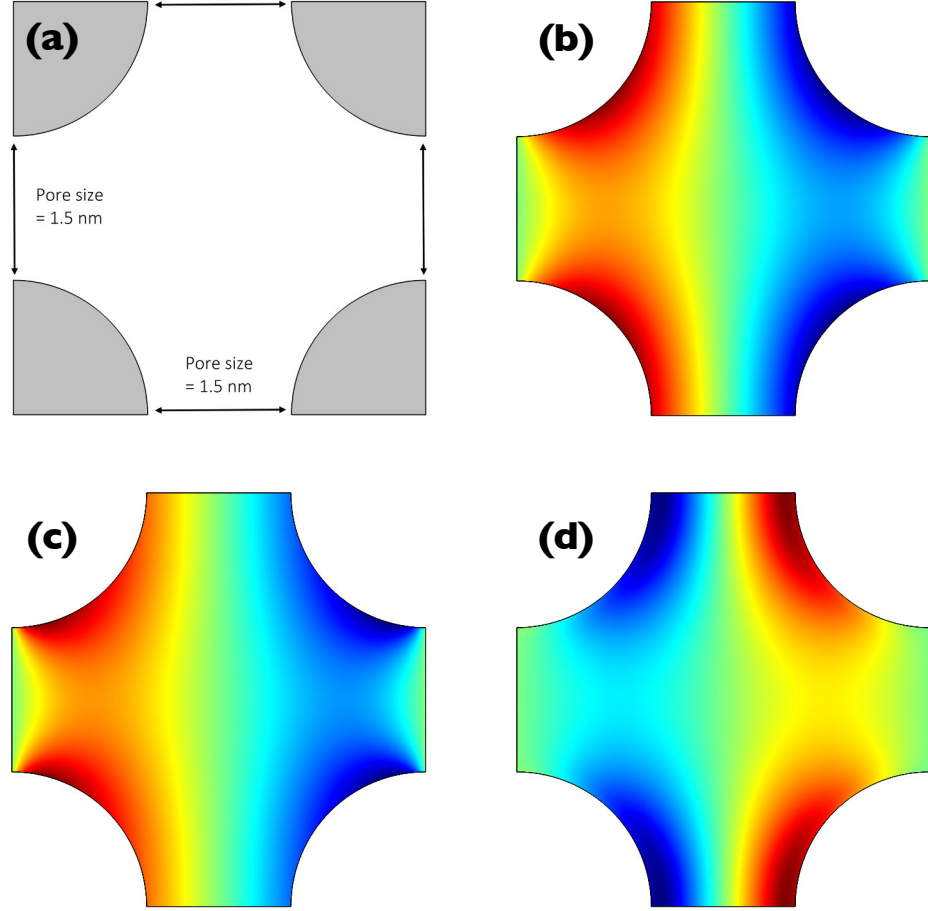


Figure 3.1: (a) A unit cell comprising a homogeneous isotropic nanoporous material with porosity $\omega = 0.67$ and pore throat size 1.5 nm. (b) Spatial distribution of the closure variable $\chi(y_1, y_2)$ for electroneutral fluid, computed by solving the scalar version of (3.16) with $\varphi_{\text{EDL}} = 0$ for $c_{\text{in}} = 0.93$ M. (c) and (d) Spatial distributions of the closure variables $\chi_+(y_1, y_2)$ and $\chi_-(y_1, y_2)$, respectively, computed by solving the scalar versions of (3.16) with $\varphi_{\text{EDL}} = 0.3$ V for $c_{\text{in}} = 0.93$ M.

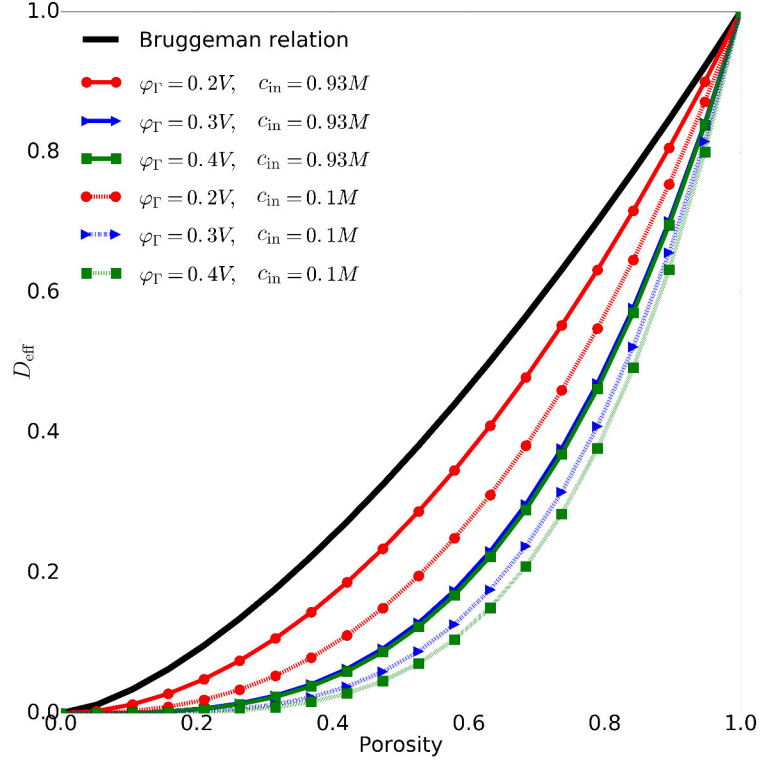


Figure 3.2: The normalized effective diffusion coefficient of an isotropic nanoporous material, $\mathcal{D}^{\text{eff}}/D$, computed alternatively with Bruggeman's relation $\mathcal{D}^{\text{eff}} = D\omega^{3/2}$ and our model (3.15) and (3.17). Unlike Bruggeman's relation, our model captures the dependence of D^{eff} on electrical surface potential φ_{Γ} and initial ion concentration c_{in} .

the Helmholtz capacitance C_H is practically independent of both the surface potential and electrolyte concentration[106, 95] and has values[35] ranging from 20 $\mu\text{F}/\text{cm}^2$ to 45 $\mu\text{F}/\text{cm}^2$. Finally, the surface charge density σ is computed as[70, 43, 106]

$$\sigma = \sqrt{4\mathcal{E}RTI} \sqrt{\cosh\left(\frac{e\varphi_\Gamma}{kT}\right) - \cosh\left(\frac{e\varphi_{\min}}{kT}\right)},$$

$$I = z^2 C, \quad \varphi_{\min} = \min_{\mathbf{y} \in \mathcal{U}_P} \varphi_{\text{EDL}}(\mathbf{y}) \quad (3.19)$$

where I is the ionic strength, φ_{\min} is the midplane potential computed by solving (3.13). Combining (3.18) and (3.19) gives a transcendental equation for φ_Γ , whose solution, depending on the choice of parameters, varies between 0.2 V and 0.4 V when the external voltage $V = 1.2$ V is applied.

3.4 Application to electrical double layer capacitors

Electrical double layer capacitors (EDLCs) store energy in the EDL; they have been shown to possess high power density and long reversible cycle life. These properties suggest that EDLCs can be used in electric and hybrid electric vehicles to offset the low charge/discharge of current in batteries, providing an acceleration boost. The performance of EDLCs has been analyzed with effective electrodiffusion models, which were validated with experimental data[96, 6, 47]. Our goal is to improve the predictive power of EDLC models by using our expressions for the effective diffusion coefficients.

A mathematical model of EDLCs. A typical EDLC consists of three compartments, positive and negative electrodes separated by a porous dielectric material (Fig. 3.3), which are fully saturated with electrolyte. The models[96, 70] assume that i) both the electrodes (made from a porous activated-carbon material) and the separator are homogeneous and isotropic, ii) temperature is uniform and constant throughout the EDLC, and iii) convection in the cell is negligible.

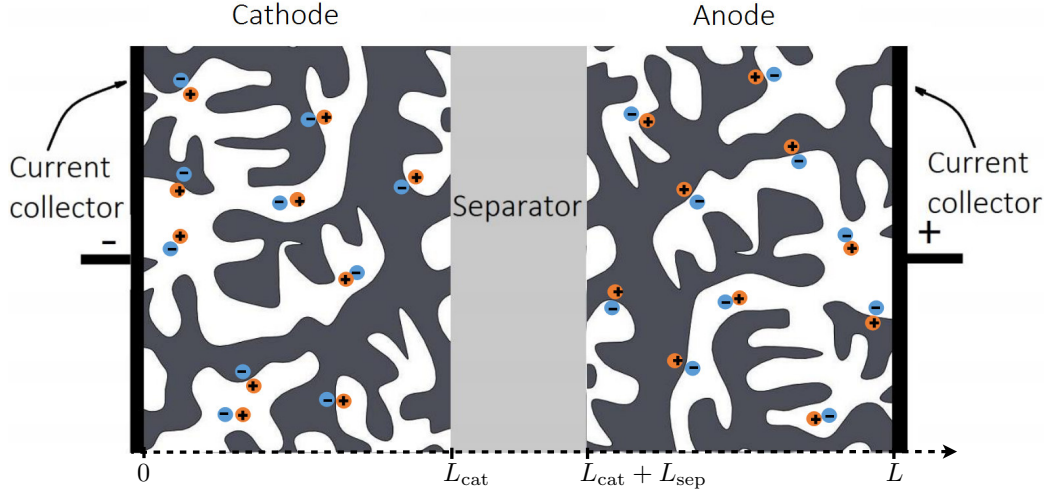


Figure 3.3: Schematic representation of an electrical double layer capacitor (EDLC) cell. Pore space of the cathode and anode and the separator is filled with electrolyte. The electrolyte within the carbon electrodes is electrically neutral, i.e., the total charge of the ions adsorbed on the electrode surfaces is balanced by the surface charge on the carbon electrodes. The separator is made of a porous dielectric material, such as glass fiber.

Under these assumptions, the EDLC behavior is characterized by three macroscopic state variables: electrolyte ionic concentration, $C(x, t)$; electrolyte potential, $\Phi(x, t)$; and electric potential of the solid phase, $\Phi_s(x, t)$. For the EDLC in Fig. 3.3, these variables satisfy a three-equation model[96] (see Appendix D for derivation),

$$C_{\text{EDL}} \frac{\partial(\Phi_s - \Phi)}{\partial t} = \frac{\partial}{\partial x} \left(\sigma_s \frac{\partial \Phi_s}{\partial x} \right), \quad (3.20)$$

$$\frac{\partial}{\partial x} \left(\sigma_s \frac{\partial \Phi_s}{\partial x} + \kappa^{\text{eff}} \frac{\partial \Phi}{\partial x} + \kappa^{\text{eff}} RT \frac{2t_+ - 1}{zF} \frac{\partial \ln C}{\partial x} \right) = 0, \quad (3.21)$$

$$\omega \frac{\partial C}{\partial t} = \frac{\partial}{\partial x} \left(\mathcal{D}^{\text{eff}} \frac{\partial C}{\partial x} \right) - \alpha \frac{\partial (\Phi_s - \Phi)}{\partial t}, \quad (3.22)$$

that is defined for $x \in [0, L]$.

Here the effective conductivity of the electrolyte, κ^{eff} , is given by

$$\kappa^{\text{eff}} = \nu z^2 \frac{F^2 c_{\text{in}}}{RT} (D_+^{\text{eff}} + D_-^{\text{eff}}); \quad (3.23a)$$

the transference number t_+ , the fraction of the current carried by cations, has the form

$$t_+ = \frac{D_+^{\text{eff}}}{D_+^{\text{eff}} + D_-^{\text{eff}}}; \quad (3.23b)$$

σ_s is the electric conductivity of the solid phase, with $\sigma_s = 0$ in the dielectric separator ($L_{\text{cat}} < x < L_{\text{cat}} + L_{\text{sep}}$); the EDL capacitance \mathcal{C}_{EDL} is absent in the dielectric separator ($\mathcal{C}_{\text{EDL}} = 0$ for $L_{\text{cat}} < x < L_{\text{cat}} + L_{\text{sep}}$); and

$$\alpha = \frac{\mathcal{C}_{\text{EDL}}}{\nu z F} \begin{cases} t_+ - 1 & 0 < x < L_{\text{cat}} \\ 0 & L_{\text{cat}} < x < L_{\text{cat}} + L_{\text{sep}} \\ t_+ & L_{\text{cat}} + L_{\text{sep}} < x < L. \end{cases} \quad (3.23c)$$

Since $\sigma_s = 0$ for $L_{\text{cat}} < x < L_{\text{cat}} + L_{\text{sep}}$, it follows from (3.20) that in the separator $i_{\text{liquid}} = i$, i.e., the liquid-phase current i_{liquid} equals the total (externally applied)

current i . Moreover, since the solid phase of the separator is dielectric, $\Phi_s = 0$ for $L_{\text{cat}} < x < L_{\text{cat}} + L_{\text{sep}}$.

The partial-differential equations (3.20)–(3.22) are subject to the following boundary conditions[96]. Since the EDLC surface is impermeable to electrolyte and the current it carries,

$$\frac{\partial C}{\partial x} = 0, \quad \frac{\partial \Phi}{\partial x} = 0 \quad \text{at } x = 0, L; \quad (3.24a)$$

with the second condition stemming from $i_{\text{liquid}} = 0$. Application of the external current i to the anode ($x = L$) gives rise to the boundary condition

$$\sigma_s \frac{\partial \Phi_s}{\partial x} = -i \quad \text{at } x = L. \quad (3.24b)$$

Finally, the (reference) electric potential at the cathode ($x = 0$) is set to

$$\Phi_s = 0 \quad \text{at } x = 0. \quad (3.24c)$$

The initial conditions are $\Phi(x, 0) = 0$, $\sigma_s \partial_x \Phi_s(x, 0) = -i$ and $C(x, 0) = c_{\text{in}}$.

An observable quantity, and the quantity of interest computed with (3.20)–(3.24), is an EDLC's voltage response, $V_{\text{cell}}(L, t) \equiv \Phi_s(L, t) - \Phi_s(0, t) = \Phi_s(L, t)$, to charging with the constant current i .

Model parametrization. The experimental study[96] of an EDLC's voltage response involves activated carbon electrodes, whose homogeneous, orderly aligned microstructure has average pore throat size of 1.5 nm, with porosity $\omega = 0.67$. These and other relevant parameter values from this experiment are collated in Table 3.1.

Table 3.1: Parameter values used in the experimental study[96] of supercapacitors.

Parameter	Value	Units
Electrodes thickness, $L_{\text{cat}} = L_{\text{an}}$	50	μm
Separator thickness, L_{sep}	25	μm
Initial ion concentration, c_{in}	0.93	mol/l
Porosity of electrodes, ω	0.67	-
Porosity of separator, ω	0.6	-
Solid phase conductivity, σ_{s}	52.1	S/m
Tortuosity of separator, τ_{sep}	1.3	-
Charge number, z	1	-
Dissociation coefficient, ν	1	-
Charging current, i	36.4	A/m ²
Conductivity of electrolyte at c_{in} , κ	0.67	mS/cm
Molecular diffusion coefficient, D	4.312×10^{-5}	cm ² /s

The nearly equal solvated tetrafluoroborate anion and tetraethylammonium cation sizes in acetonitrile used in the experiment suggest the equality of their molecular diffusion coefficients, $D_+ = D_- = D$. The value of $D = 4.312 \times 10^{-5}$ cm²/s was determined from measurements of the electrical conductivity of acetonitrile by using a free-electrolyte version of (3.23a), $D = RT\kappa/(2\nu z^2 F^2 c_{\text{in}})$. The EDL capacitance \mathcal{C}_{EDL} serves as the only fitting parameter[96].

Simulation results. The parametrization of the mathematical model (3.20)–(3.24) in the analysis[96] is completed by employing the empirical relation $\mathcal{D}_{\pm}^{\text{eff}} = \mathcal{D}^{\text{eff}} = D\omega/\tau$ with an assumed tortuosity value of $\tau = 2.3$. According to (3.23), the equality $\mathcal{D}_+^{\text{eff}} = \mathcal{D}_-^{\text{eff}}$ translates into $t_+ = 0.5$ and $\kappa^{\text{eff}} = \kappa\omega/\tau$. Fitting the resulting model prediction of the EDLC’s voltage response to data yields $\mathcal{C}_{\text{EDL}} = 42$ F/cm³, with the predicted voltage response $V_{\text{cell}}(t)$ shown in Figure 3.4 by the dotted line. A modification of this procedure, which replaces the assumed tortuosity value with that

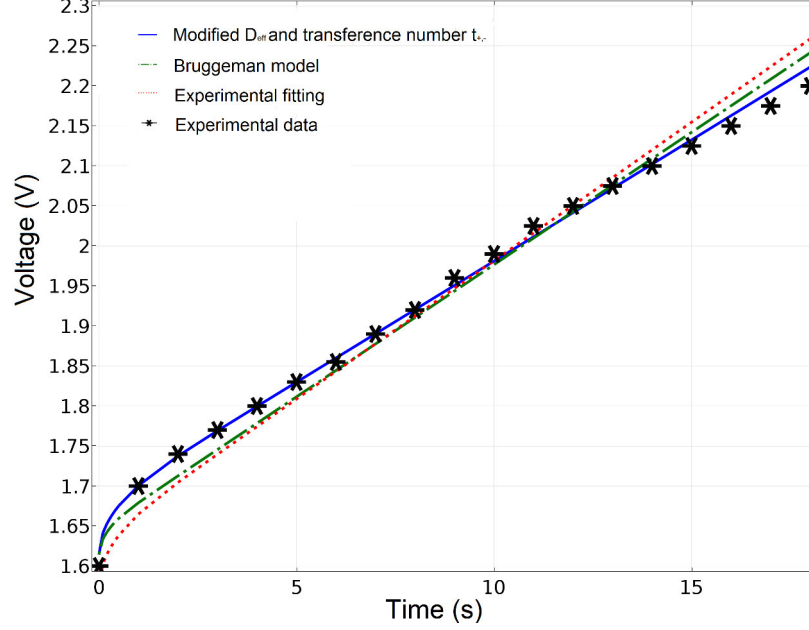


Figure 3.4: Measured EDLC voltage response to charging[96] (stars), and its counterparts predicted with the original model[96] (dotted line), the same model supplemented with the Bruggeman relation (dashed line) and our effective model (solid line).

given by the Bruggeman relation $\tau = \omega^{-0.5} = 1.2$, yields $\mathcal{C}_{\text{EDL}} = 44 \text{ F/cm}^3$ and the prediction of $V_{\text{cell}}(t)$ that is closer to the experiment (Fig. 3.4).

Unlike these two phenomenological relations, our model (??) yields unequal effective diffusion coefficients for cations and anions, $D_-^{\text{eff}} \neq D_+^{\text{eff}}$, which accounts for the EDL effects.¹ Substituting these values into (3.23b) and (3.17) yields the cation (tetraethylammonium ion) transference number $t_+ = 0.779$ and the effective binary diffusion coefficient \mathcal{D}^{eff} , respectively. Fitting the resulting model prediction of the EDLC's voltage response to data yields $\mathcal{C}_{\text{EDL}} = 47 \text{ F/cm}^3$, with the predicted voltage

¹These values were computed as follows. In the experiment[96], application of the constant charging current $i = 36.4 \text{ A/m}^2$ to the anode changed the EDLC voltage from $V = 1.6 \text{ V}$ to $V = 2.2 \text{ V}$ (Fig. 3.4). We took the midpoint voltage as external voltage $V = 1.9 \text{ V}$ of EDLC cell during charging; from (3.18) and (3.19), the diffuse layer potential $\varphi_{\Gamma} = 0.4 \text{ V}$ was calculated. Due to short time charging, the influence of concentration variation on EDL potential distribution is negligible. Double layer potential in (3.13) is thus solved with characteristic ion concentration $c_{\text{b}}^* = c_{\text{in}} = 0.93 \text{ M}$ and the diffuse layer potential $\varphi_{\Gamma} = 0.4 \text{ V}$.

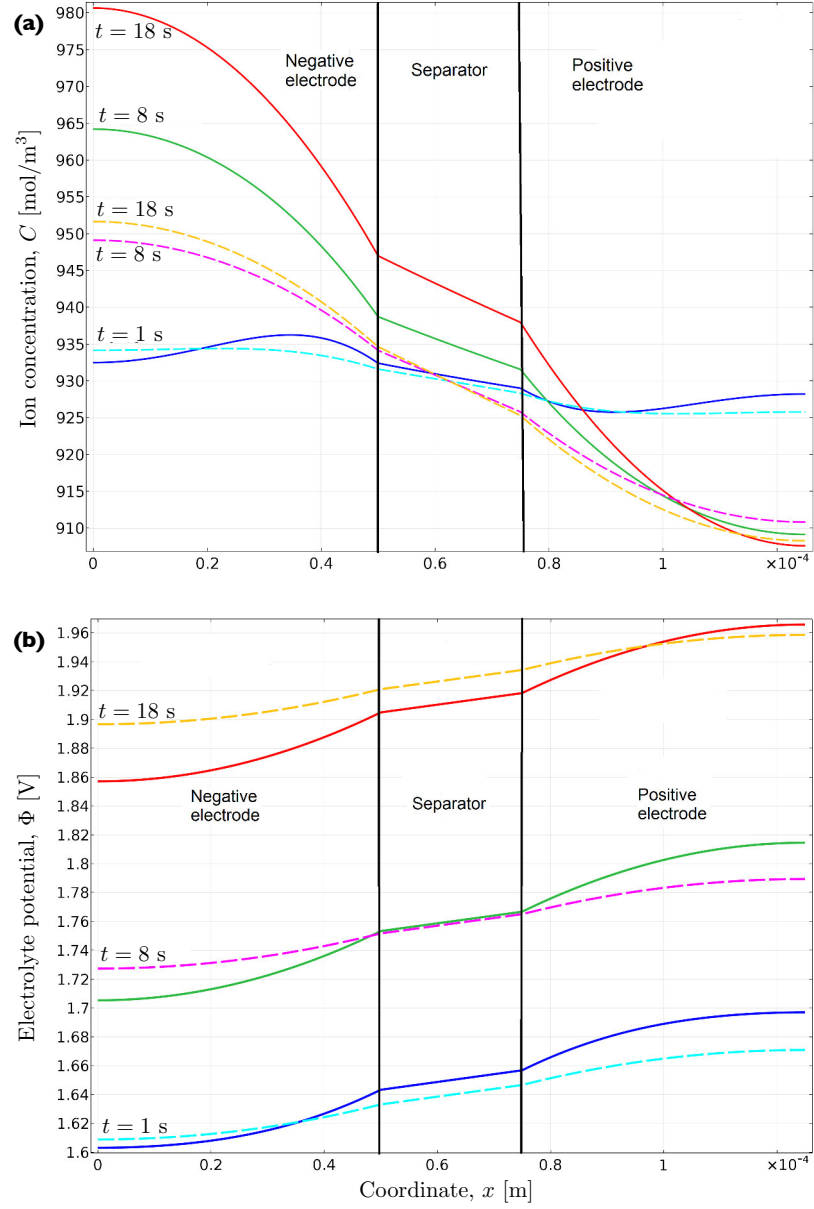


Figure 3.5: Temporal snapshots, at $t = 1, 8$ and 18 s, of the (a) ion concentration $C(x, t)$ and (b) electric potential $\Phi(x, t)$ profiles computed with our rigorously derived model (solid lines) and the Bruggeman relation (dashed lines). Our model predicts significantly higher gradients of both ion concentration and electric potential.

response $V_{\text{cell}}(t)$ shown in Figure 3.4 by the solid line. This result demonstrates that our model matches the data better than its empirical counterparts; crucially, it does not rely on the assumed relation $\mathcal{D}^{\text{eff}} = D\omega/\tau$. (If needed, one can estimate an electrode's tortuosity from this relation, which for the material under investigation yields $\tau = \omega D/\mathcal{D}^{\text{eff}} = 2.4$ or $\tau = \omega^{-2.3}$).

Figure 3.5 exhibits temporal snapshots of the ion concentration and electric potential profiles computed alternatively with our rigorously derived model and the empirical Bruggeman relation. The gradients of both the ion concentration and electric potential increase with time, as the EDLC continues to be charged with a constant current. The Bruggeman relation significantly underestimates these gradients.

3.5 Conclusions

We derived expressions for effective diffusion coefficients, $\mathbf{D}_{\pm}^{\text{eff}}$, and transference numbers t_{\pm} , which are used in macroscopic (continuum-scale) models of ion transport in nanoporous materials. These expressions relate the nanoscale topological properties of such materials (e.g., pore size and connectivity) to their macroscopic counterparts (e.g., porosity and tortuosity) and account for the nonlinear effects of the electrical double layer (EDL) on ion transport. While applicable to a wide range of electrochemical phenomena in porous materials, these expressions are deployed here to estimate the voltage response of an electrical double layer capacitor (EDLC) to charging. Our analysis leads to the following major conclusions.

1. The effective diffusion coefficients $\mathbf{D}_{\pm}^{\text{eff}}$ are, in general, second-rank semi-positive definite tensors, reflecting possible anisotropy of nanoporous structures.

2. Even if molecular diffusion coefficients of cations (D_+) and anions (D_-) in an electrolyte are equal, their effective counterparts differ, $\mathbf{D}_+^{\text{eff}} \neq \mathbf{D}_-^{\text{eff}}$, unless the binary electrolyte is symmetric (i.e., has equal dissociation coefficients, $\nu_+ = \nu_-$, and ion charges, $z_+ = z_-$).
3. Even if the cations and anions in an electrolyte have similar size, their effective transference numbers are not equal, $t_+ \neq t_-$, unless the binary electrolyte is symmetric.
4. These features of the effective parameters are a manifestation of the EDL's effects on diffusion of ions in nanoporous materials. These effects are not captured by phenomenological relations, such as Bruggeman's relation $D^{\text{eff}} = \omega^{3/2}D$, which estimate the effective ionic diffusion D^{eff} as a fraction of the molecular diffusion of ions in electrolyte, D , reduced by a power of porosity ω .
5. Bruggeman's relation overestimates the effective diffusion coefficient and effective electric conductivity, especially for dilute solutions and relatively large diffuse layer potentials φ_Γ .
6. By accounting for the electrochemical effect at the fluid-solid interfaces (specifically, the reduction of surface area[25]), our expressions increase the accuracy of predictions of double-layer capacitance of electrode materials.
7. The use of our effective coefficients in a macroscopic model of EDLC charging yields the predictions of voltage response that are in close agreement with the data[96]. The reliance on Bruggeman's relation significantly underestimates the gradients of both ion concentration and electric potential within the EDLC.

3.6 Acknowledgments

This research was supported in part by the Defense Advanced Research Projects Agency under the EQUIPS program and the National Science Foundation under grant DMS-1522799.

This chapter is a reprint of the material as it appeared in: Zhang, X. and Tartakovsky, D.M., "Effective Ion Diffusion in Charged Nanoporous Materials". The dissertation author was the primary investigator and author on this paper.

Chapter 4

Optimal Design of Nanoporous Materials for Electrochemical Devices

4.1 Abstract

Unique macroscopic properties of nanoporous metamaterials stem from their microscopic structure. An optimal design of such materials is facilitated by mapping a material's pore-network topology onto its macroscopic characteristics. This is in contrast to both a trial-and-error experimental design and design based on empirical relations between macroscopic properties, such as the often-used Bruggeman formula that relates a material's effective diffusion coefficient to its porosity. We use homogenization to construct such a map in the context of materials design that maximizes energy/power density performance in electrochemical devices. For example, effective diffusion coefficients and specific surface area, key macroscopic characteristics

of ion transport in a hierarchical nanoporous material, are expressed in terms of the material’s pore structure and, equally important, ion concentrations in the electrolyte and externally applied electric potential. Using these microscopic characteristics as decision variables we optimize the macroscopic properties for two material’s assembly templates and several operating conditions. The latter affect the material’s performance through formation of electrical double layer at the fluid-solid interfaces, which restricts the pore space available for ion transport.

4.2 Introduction

Advances in materials science offer a plethora of alternative strategies for generation of nanoporous metamaterials with prescribed pore structures [16?]. This opens the possibility of bottom-up design of application-specific materials that optimize a desired macroscopic property, e.g., permittivity [16] or electric capacitance [?]. When not done by trial-and-error, metamaterial assembly is often guided by phenomenological relations between macroscopic properties. For example, the effective diffusion coefficient, D^{eff} , for a material with porosity ω and tortuosity τ is estimated from the corresponding molecular diffusion in free solvent, D_{m} , by using a phenomenological model $D^{\text{eff}} = \omega D_{\text{m}} / \tau$; if supplemented with another assumption, $\tau = 1 / \sqrt{\omega}$, this gives Bruggeman’s relation $D^{\text{eff}} = \omega^{3/2} D_{\text{m}}$.

Reliance on such macroscopic relations has a number of limitations. First, they provide insufficient information about the pore structure and, hence, are of limited use in its design. Second, their veracity is questionable, especially when (in the case of diffusion) pores are small and concentration gradients are large. While Bruggeman’s relation is widely used to model ion diffusion in charged porous media (e.g., [70] and

references therein), it fails to account for the diffusion coefficient's reduction due to formation of an electrical double layer (EDL) on the electrolyte-solid interfaces. Effects of the latter phenomenon are magnified in nanoporous materials, wherein adjacent EDLs can overlap, appreciably restricting the pore space available for ion transport. Such materials are mooted as a breakthrough technology for energy storage [23, 25].

Dynamic maps expressing macroscopic (effective) parameters in terms of microscopic properties of porous media are derived by means of upscaling techniques. Crucially, such parameters depend not only on the pore structure but also on pore-scale processes that, in the case of electrochemical systems, affect the EDL formation. Examples of upscaling analyses of pore-scale electrochemical phenomena described by Poisson-Nernst-Planck's equations can be found in [37, 38, 83, 109]. Our goal is to use the results of one such analysis [109] to inform the design of hierarchical nanoporous materials, which optimizes a material's macroscopic properties (diffusion coefficient and electric capacitance) by using the pore structure and operation conditions (electrolyte concentration and externally imposed electric potential) as decision variables.

4.3 Macroscopic transport model

Macroscopic representations of a charged nanoporous material Ω treat it as a continuum, without separating it into the pore space \mathcal{P} and the solid skeleton \mathcal{S} . Final homogenized macroscopic Nernst-Planck equations satisfied by macroscopic ion

concentration $C(\mathbf{x}, t)$ and electric potential $\Phi(\mathbf{x}, t)$,

$$\omega \frac{\partial C}{\partial t} = \nabla \cdot [\mathbf{D}_{\pm}^{\text{eff}} (\nabla C \pm \frac{zF}{RT} C \nabla \Phi)]. \quad (4.1)$$

Here ω is porosity, F, R, z, T are Faraday constant, gas constant, valency and temperature, respectively. The effective diffusion coefficients $\mathbf{D}_{\pm}^{\text{eff}}$ are second-order semi-positive-definite tensors defined by

$$\begin{aligned} \mathbf{D}_{\pm}^{\text{eff}} &= \frac{\mathcal{D}\omega}{G_{\pm}} \int_{\mathcal{P}_{\mathcal{U}}} e^{\mp \frac{zF}{RT} \varphi_{\text{EDL}}} (\mathbf{I} + \nabla_{\mathbf{y}} \boldsymbol{\chi}_{\pm}^{\top}) d\mathbf{y}, \\ G_{\pm} &= \int_{\mathcal{P}_{\mathcal{U}}} e^{\mp \frac{zF}{RT} \varphi_{\text{EDL}}} d\mathbf{y}, \end{aligned} \quad (4.2)$$

where \mathbf{I} is the identity matrix, \mathcal{D} is molecular diffusion coefficient and φ_{EDL} is electric potential distribution inside EDL. The closure variables $\boldsymbol{\chi}_{\pm}(\mathbf{y})$ are \mathcal{U} -periodic vector functions, which are computed as solutions of boundary-value problems

$$\begin{aligned} \nabla_{\mathbf{y}} [e^{\mp \frac{zF}{RT} \varphi_{\text{EDL}}} (\mathbf{I} + \nabla_{\mathbf{y}} \boldsymbol{\chi}_{\pm}^{\top})] &= \mathbf{0}, \quad \mathbf{y} \in \mathcal{P}_{\mathcal{U}}; \\ \mathbf{n}(\mathbf{I} + \nabla_{\mathbf{y}} \boldsymbol{\chi}_{\pm}^{\top}) &= \mathbf{0}, \quad \mathbf{y} \in \Gamma_{\mathcal{U}}; \quad \int_{\mathcal{P}_{\mathcal{U}}} \boldsymbol{\chi}_{\pm} d\mathbf{y} = \mathbf{0}. \end{aligned} \quad (4.3)$$

4.4 Electrosorption on charged porous materials

Effective diffusion coefficients ($\mathbf{D}_{\pm}^{\text{eff}}$) are not only crucial elements in understanding macroscale transport, also can be used as instruction to predict performance and guide experimental design of porous electrode materials. Comparing electrosorption model with previous paper [110] of solvent transport through uncharged porous material under Langmuir adsorption reaction, charged solid materials exert considerable

influence on transport process via accumulated ions within electrical double layer.

Aiming at exploring porous structure and aiding design optimal porous electrode, we simulate ion transport in half cell - positive electrode (φ is positive). Two dimensional hierarchical structure [97, 98] is studied and discussed for the its application of various sorption behaviors. See Fig. 4.1 , pore connection stuctures, like mesopores' overlapping (transverse direction **1**) and nano-channels engaged (longitudinal direction **2**) types are explored. Either dilute solution or small pore size can impair the ion transport due to thick diffuse layer in pores. From the simulation results, we will discuss such phenomenon.

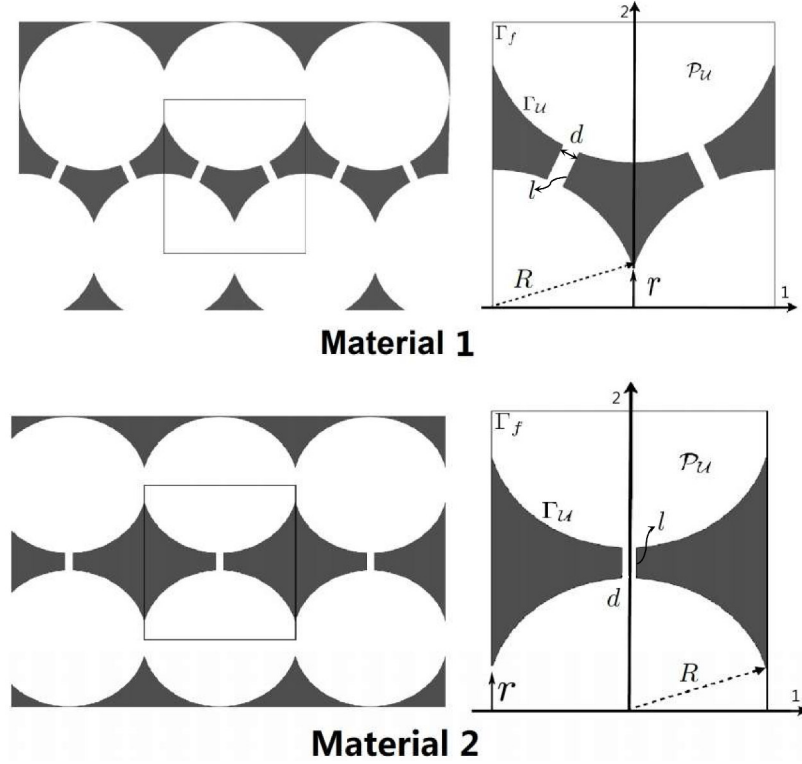


Figure 4.1: Conceptual and schematic representation of hierarchical porous texture containing mesopores and micropores[110].

Binary diffusion coefficient \mathcal{D} is used for electrochemical systems like batteries, supercapacitors, its magnitude is limited by relatively smaller ionic diffusivity[84, 106]

. For simplicity, effective binary diffusion coefficient \mathbf{D}^{eff} of monovalent solution shown in the plots is in the form of D_1 and D_2 that $\mathbf{D}^{\text{eff}}/(\omega\mathcal{D}) = \begin{bmatrix} D_1 & 0 \\ 0 & D_2 \end{bmatrix}$. Symbols D_1 and D_2 stand for the ration between effective diffusion and the product of porosity and molecular diffusivity in transverse and longitudinal direction respectively. Generally, the studies of energy storage systems use prediction $D^{\text{eff}} = \mathcal{D} \frac{\omega}{\tau}$ for effective diffusion coefficient (τ is the tortuosity of the material). This leads to the assumption that porous electrode materials are isotropic. Actually, we just prove D_1 and D_2 are not necessarily identical due to microstrucure.

4.4.1 Parameters for electrosorption study

General micro and meso pore sizes for electrical double layer capacitors are employed for this study [12, 88, 103] . Micropore size is as small as 1nm and mesopores can range from 2 to 10 nm. Versatile performances of porous carbon materials depend on pore sizes. Therefore, in the following simulation, mesopore radius R ranges from 2 nm to 5 nm, radius of adjoining mesopores is treated as $r = 0.4$ nm, nanochannel tube size $d = 0.7$ nm, lenght $l = 3$ nm.

External voltage V is limited by the breakdown voltage of electrolyte species. For example aqueous solution breakdown voltage could reach 1.23 V depends on electrolyte, while organic electrolyte can be as high as 4 V[25] . The diffuse layer potential φ_d on the charged material after an applied external voltage V is $\varphi_d = \frac{V}{2} - \phi_{\text{ecm}} - \frac{\sigma}{C_H}$ (Zhang and Tartakovsky, 2016). Therefore applied voltage factor on diffuse layer potential is studied from as low as $\varphi_d = 0.2$ V to 0.4 V for aqueous solution.

Dilute concentrations of electrolyte is assumed that Poisson Boltzmann (PB)

equation is satisfied. In the case of slit shaped pores, Yeomans [107] found that PB equation always gives very good results for low concentrations of monovalent electrolytes. Therefore, the electrolyte concentration of 0.1 M (mol/L) is considered as the upper limit of ion concentration that we use for analysis[106].

Effective diffusion coefficients of electrosorption model varying with multiple objective variables - mesopore radius R , micropore radius r , concentration C , diffuse layer potential φ_d , porosity ω and different microstructures are discovered.

4.4.2 Results and discussions

Previous study for uncharged optimal nanoporous structure isn't applicable and replicable to an electrosorption charged material [110]. Mesopores show good electrochemical accessibility. However micropores, superior in high surface area, present a slow mass transfer of ions inside pores because micropores are about the same size of Debye length. The effect of electrical double layer on retarding transport inside pores can be reduced by increasing the pore size, electrolyte concentration, and applied potential. Results of effective diffusion coefficients with different pore sizes R , electrolyte concentrations C and diffuse layer potentials φ_d are analyzed.

Electrolyte concentration C We study the effect of electrolyte concentration on ion transport in charged materials as a function of mesopore size R . Concentrations considered are for dilute electrolytes, $C = 0.1, 0.05$ M and relative diluter $C = 0.01$ M . See Fig. 4.2, Fig. 4.3 and Fig. 4.4.

Effective diffusion coefficients decrease with increasing mesopore size R in both charged and uncharged materials 1 and 2. In material 1 (Fig. 4.2), transport in longitudinal direction shows different concentrations give rise to slight deviations

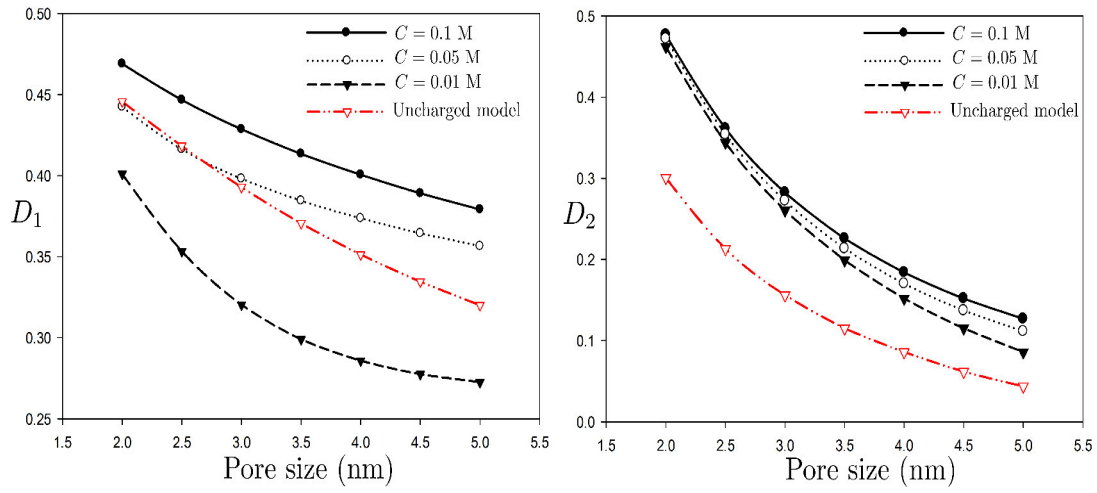


Figure 4.2: Effective diffusion coefficients \mathbf{D}^{eff} as a function of concentration, for material 1 with diffuse layer potential $\varphi_d = 0.2$ V.

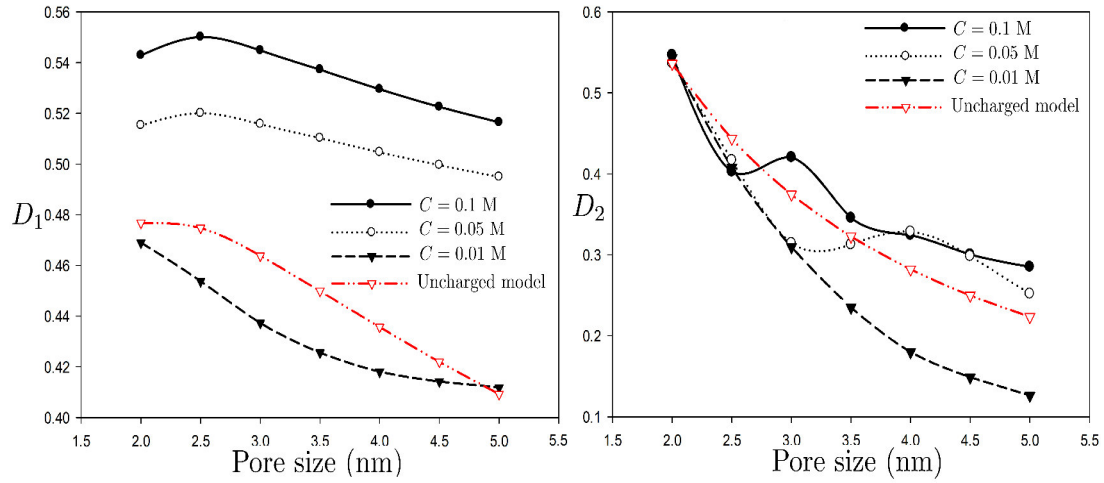


Figure 4.3: Effective diffusion coefficients \mathbf{D}^{eff} as a function of concentration, for material 2 with diffuse layer potential $\varphi_d = 0.2$ V.

of D_2 . Overall, material 2 has larger effective diffusion in both directions (Fig. 4.3). Concentration as low as $C = 0.01$ M indicates inhibition of the transport in charged materials (always smaller than uncharged materials). Material 2 data also implies that D_2 starts to surpass uncharged model for mesopore radius larger than 3.0 nm and larger concentration $C \geq 0.05$ M.

Indiscriminately choosing larger mesopore R may help create more space for ions to diffuse. However, if micropores are keeping the same, resulted from the increasing ratio of 'arc and chord', larger mesopores will lead to larger tortuosity. Micropore size r is a determinant factor of micropore-mesopore hierarchical structure. Real effective size of micropores for transport is determined by electrical double layer thickness.

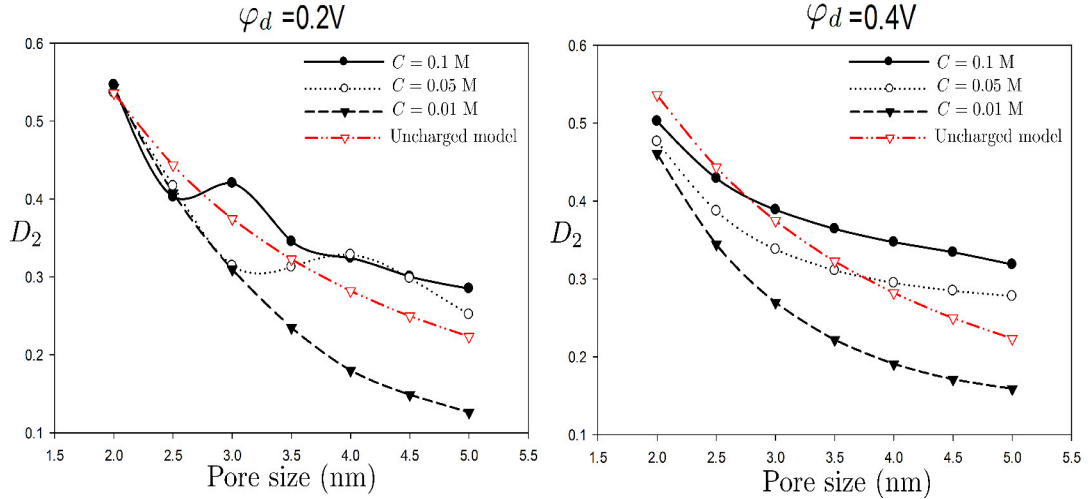


Figure 4.4: Longitudinal transport D_2 as a function of dilute concentration $C = 0.01$ M, for material 2 with different diffuse layer potentials.

Diffuse layer potential φ_d The oscillatory behaviors of charged material 2 for small $\varphi_d = 0.2$ V comes from the integrated influences of electric field, concentration and pore structure (angled channels). Such oscillation vanishes by applying larger

electric field Fig. 4.4. For material 1, higher diffuse layer potential φ_d always shows larger effective diffusion coefficients in both directions. Transverse D_1 for charged materials are smaller than uncharged model for dilute concentration $C = 0.01$ M (see Fig. 4.5). In Fig. 4.6 material 2, the occurrence of electrical double layer overlapping in micropores narrows the 'throat' for ion to transport to mesopores. Such phenomena dramatically changes D_1, D_2 tendencies with respect to mesopore size. (see Fig. 4.3 and Fig. 4.6)

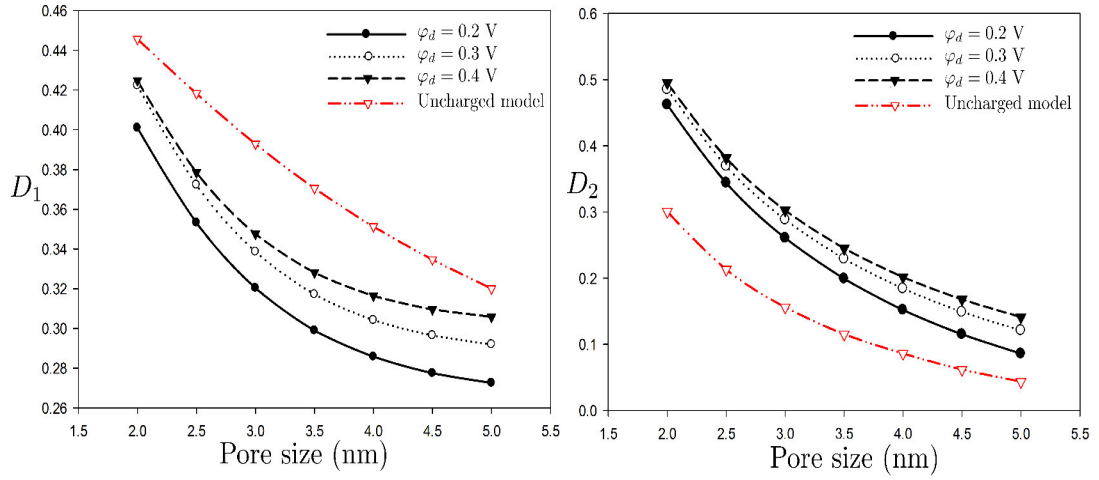


Figure 4.5: Effective diffusion coefficients D^{eff} as a function of diffuse layer potential, for material 1 with concentration $C = 0.01$ M

Synergistic Discussion Distinctions between different dilute concentrations $C = 0.1$ M and $C = 0.01$ M are magnificent (see Fig. 4.6 and Fig. 4.7). For dilute solution, due to larger double layer thickness, solution transport is interfered with the occurrence of micropores' electrical double layer overlapping. While, for denser solution $C = 0.1$ M, transport is strengthened by applied electric field. The decline tendencies of D_1 and D_2 are slowing down with larger mesopores. As a consequence, the concentration of solution plays a critical role in porous electrode application.

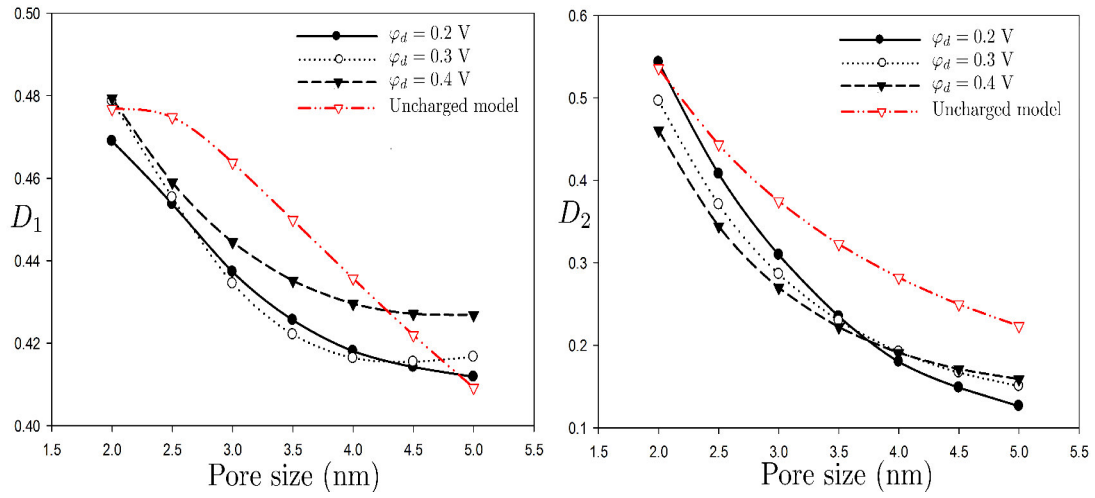


Figure 4.6: Effective diffusion coefficients D^{eff} as a function of diffuse layer potential, for material 2 with concentration $C = 0.01$ M

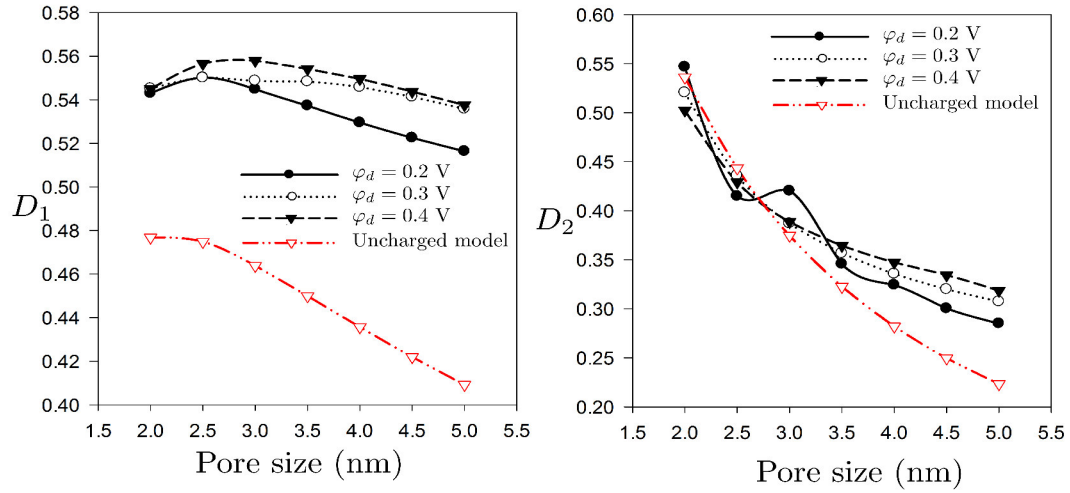


Figure 4.7: Effective diffusion coefficients D^{eff} as a function of diffuse layer potential, for material 2 with concentration $C = 0.1$ M

With regard to the relation of electric field (See Fig. 4.3, D_2), small diffuse layer potential $\varphi_d \leq 0.2$ V may cause transport oscillation in longitudinal direction owing to anisotropic pore scale structure. Such oscillational factor can be eliminated by applying larger electric field ($\varphi_d \geq 0.3$ V) Fig. 4.7.

Therefor the design of ideal porous material for the objectives of higher transport flexibility and capability should take account of synergistic effects of pore structure, electric field and solution concentration. The radius of mesopores less than 3 nm has extensive applicabilities to different electric field and concentration.

4.5 Optimum design of microstructure for charged materials

One significant goal of material science is to have perceptive knowledge of structure/properties relations to design material microstructures with desired properties and performance characteristics. Homogenization is used to obtain effective properties from microscopic information of porous materials which effective material properties are used to determine the macroscale structural performance. Optimization methods provide a systematic means of designing heterogeneous materials with desired macroscopic properties and microstructures. Combining such modeling techniques with novel synthesis and fabrication methodologies may make optimal design of real materials a reality in the future.

4.5.1 The optimization problem

To obtain optimum microstructure aiming at both high surface reaction and high transport performance, we introduce the objective function of maximizing specific surface area α_v . This is an optimization problem with constrained conditions of macroscopic diffusion coefficients $\mathbf{D}_{\text{obj}}^{\text{eff}}/(\omega\mathcal{D}) = \begin{bmatrix} D_{1,\text{obj}} & 0 \\ 0 & D_{2,\text{obj}} \end{bmatrix}$.

$$\max_{\{R,r,d,l\}} \alpha_v(R, r, d, l)$$

subject to :

$$95\%D_{1,\text{obj}} \leq D_1 \leq 105\%D_{1,\text{obj}} \quad (4.4)$$

$$95\%D_{2,\text{obj}} \leq D_2 \leq 105\%D_{2,\text{obj}}$$

$$L_b \leq \{R, r, d, l\} \leq U_b$$

Structural variables R, r, d, l are geometrical conditions in determining effective diffusion coefficient in eq. (??). Table 4.1 lists geometrical limits of design structure. Micropore radii r should be smaller than 1 nm by definition, mesopores are controlled within the range determined from previous section discussion $R < 3$ nm. Nano-channel diameter d is controlled by manufacture limits and length l determines the thickness between each mesopores. Objective of $D_{1,\text{obj}}$ and $D_{2,\text{obj}}$ in transverse and longitudinal directions are estimated from the values found in previous section.

Table 4.1: Geometry limits of porous structure

	R	r	d	l
	(nm)	(nm)	(nm)	(nm)
L_b	1.6	0.5	0.6	3.0
U_b	3.0	0.7	1.0	5.0

Optimization is running for both material 1 and material 2 under different electrolyte concentrations. A general conclusion of optimum mesopore size ($2R$) is around 3 to 4 nm, micropore ($2r$) is around 1nm. Due to the structural feature, material 2 has the capacity to reach higher transport performance (larger $D_{1,obj}$, $D_{2,obj}$). Also material 2 has larger specific surface area α_v as the objective of optimization. We can tell from $D_{2,obj} > D_{1,obj}$ in Table 4.2 and Table 4.3 that longitudinal transports of both material structures are superior to transport in transverse direction. Nano-channel size is optimum to diameter $d = 0.6$ nm, length about $l = 3.3$ nm.

Table 4.2: Material 1, dilute electrolyte ($C = 0.1$ M and 0.01 M), $\varphi_d=0.3$ V

	R	r	d	l	$D_{1,obj}=0.57$	$D_{2,obj}=0.59$	α_v
$C = 0.1$ M	1.756	0.571	0.6	3.30	0.5713	0.5896	1.223
	1.755	0.568	0.6	3.30	0.5700	0.5898	1.225
	R	r	d	l	$D_{1,obj}=0.48$	$D_{2,obj}=0.54$	α_v
$C = 0.01$ M	1.787	0.400	0.6	3.15	0.4766	0.5498	1.238
	1.787	0.400	0.6	3.15	0.4766	0.5499	1.238

Table 4.3: Material 2, dilute electrolyte ($C = 0.1$ M and 0.01 M), $\varphi_d=0.3$ V

	R	r	d	l	$D_{1,obj}=0.6$	$D_{2,obj}=0.6$	α_v
$C = 0.1$ M	1.736	0.600	0.6	3.13	0.5974	0.6150	1.423
	1.736	0.600	0.6	3.13	0.5972	0.6153	1.424
	R	r	d	l	$D_{1,obj}=0.6$	$D_{2,obj}=0.6$	α_v
$C = 0.01$ M	1.814	0.576	0.6	3.69	0.5989	0.6186	1.464
	1.814	0.576	0.6	3.69	0.5987	0.6188	1.464

4.6 Conclusions

Pore structure and microscopic ion behaviors are translated into effective diffusion coefficients in macroscopic transport model. By a proper unit cell description of pore connection and structure, effective diffusion coefficients \mathbf{D}^{eff} characterizing

transport flexibility in charged materials are derived. Such model can be used widely in multiscale electrochemical systems, from electro-separation targeting separation systems to porous electrodes based supercapacitors, batteries. Application of our model to guide experimental design of hierarchical porous materials is analyzed with design parameters, such as micropore and mesopore sizes, ion concentration and applied voltage. Our analysis leads to the following major conclusions. For maintaining micropore's high surface area feature and balancing the flexibility of transport, optimization results are concluded. Mesopore size of 3 to 4 nm and micropore size of 1 nm have extensive applicability to different electric field and concentrations. Material 2 has better transport capabilities in both directions and higher specific surface area. Very dilute concentration ($C = 0.01$ M) can cause double layer overlapping and decelerate transport in porous structure.

4.7 Acknowledgements

This research was supported in part by the Defense Advanced Research Projects Agency under the EQUiPS program and the National Science Foundation under grant DMS-1522799.

This Chapter is a reformatted reprint of the material as it appeared in: Zhang, X., and Tartakovsky, D.M., 2016. Optimal design of nanoporous materials for electrochemical devices. Submitted for review to Applied Physics Letter. The dissertation author was the primary investigator and author on this paper.

Chapter 5

Effective Transport Properties for Dendritic Spine F-actin Network

5.1 Abstract

Quantitative prediction of effective transport properties of three dimensional dendritic spine F-actin network can be accomplished with upscaling techniques. The pore scale random and complex internal structure incorporated in porous media are needed to take into account to predict the overall continuum behaviors. Such technique permits a macroscopic description of complicated pore structure for diffusion systems. Dendritic spines are the postsynaptic component of synaptic contacts. Study of the relation of synaptic structure and function is important because of the critical role of synapses in information processing in the brain and in particular learning and memory formation. The effective diffusion coefficient estimated with this technique is used to quantify transmission time between neurons in the brain. Characteristic two dimensional (2-D) unit cells drawn from 3-D models are analyzed and averaged

to obtain the anisotropic effective diffusion coefficients. Compared with intensive molecular dynamics and Brownian dynamics methods for the whole 3-D model, 2-D analysis is efficient and instructive to understand porous structure morphology and determine representative elementary volume (REV) size.

5.2 Instruction

In physical and biological science, transport problems incorporating simultaneous diffusion and reaction in porous media are in abundance. Examples are found in such widely different processes as heterogeneous catalysis, migration of atoms and defects in solids, colloid or crystal growth, and the decay of nuclear magnetism in fluid-saturated porous media, cell metabolism, diffusion of molecules through biological structures[93, 78, 39]. A detailed understanding of the complexities of transport behaviors in porous media is therefore essential for the development, design, and optimization of catalytic, signal transmission and adsorption processes and for technological exploitation of porous materials in general[45]. However, the continuum scale modeling doesn't pay attention to individual pores but the homogenized equivalent material. For instance, gas or liquid diffusion transport in the pore space is described by its molecular diffusion coefficient. The equivalent diffusion coefficient for homogenized mixture which is also known as effective/apparent diffusion coefficient is lowered than molecular diffusion coefficient. Corresponding effective transport properties could also relate to the conductivity, dielectric constant, or magnetic permeability of inhomogeneous substances.

The 3-D model is of the F-actin network of the cytoskeleton in the dendritic spine of a Purkinje neuron from an adult rat (See Fig.5.1, model provided by Dinu

Patirniche). Dendritic spines are the postsynaptic component of synaptic contacts. Synapses are the loci of neural communication and information transmission between neurons in the brain. Study of the relation of synaptic structure and function is important because of the critical role of synapses in information processing in the brain and in particular learning and memory formation. Dendritic spines are small with spine head volumes ranging $0.01 \mu\text{m}^3$ to $0.8 \mu\text{m}^3$ and it has been recently established that the precise size of each synapse is very significant to its function [13]. During learning and the formation of new memories, the efficacy of communication between neurons is adjusted through synaptic plasticity – the strengthening and weakening of individual synaptic connections in accordance with their usage histories. Functionally stronger synapses have a structurally larger spine head and area of contact and the larger size is due to an overall increase in the extent of the F-actin network in the spine. The changes in synaptic structure are affected by biochemical signaling and molecular interactions within the spine. It is important to note that the effective diffusive transport properties of the spine structure determine how fast chemical signals can transmit through it. Fig.5.1 illustrates the complexity of the F-actin network. Determination of the effective transport properties of the F-actin network would significantly reduce the complexity of the model. This is the motivation for our work here.

Methods of calculating effective transport properties, such as effective media approximation of Bruggeman and Maxwell Garret, failed to incorporate microstructure morphology information, like pore shape, pore size distribution and pore connectivity. The improvement of Maxwell theoretical work can be accessed by the utilization of statistical information about the random geometry of the medium or introduce pore

network. Probability functions are introduced in order to correlate the geometrical microstructure for a porous material [101, 67, 40]. Nevertheless, quantitatively prediction of macroscopic properties requires detailed description of internal structure, or the microstructure. Thanks to modern experimental techniques, complete information on the microstructure morphology of materials can be obtained. Techniques of capturing morphology of microstructure representations in 2-D acquire using electron or light microscopy, while in 3-D X-ray microtomography, serial sectioning, confocal imaging, or magnetic resonance imaging are commonly used [32, 90, 44]. Contrary to the case of random models of microstructures, these techniques provide the opportunities of directly reconstructed 3-D models via sweeping digitized serial sections measuring the complex morphology of the composite materials at resolutions down to a few micros. With the known morphology, computational methods such as molecular dynamics and Brownian dynamics simulations are very CPU intensive and the steady-state regime is sometimes hard to reach because one has to wait for the transient regions to decay [3, 75, 33]. A variety of robust upscaling techniques, including volume averaging [102] and homogenization via multiple-scale expansions [42] are used in this work to quantitatively predict macroscopic properties of porous materials.

In this paper work, general framework for relating macroscopic anisotropic effective diffusion coefficients to microscopic structure (reconstructed 3-D F-actin dendritic spine network) is accomplished with homogenization via multiple-scale expansions. A sufficient amount of 2-D unit cells representing microstructure are extracted from plane cross-sections of 3-D model. Effective diffusion coefficients are sequentially computed and statistically obtained by solving the closure problem in each unit cell. 2-D unit cells allow us to investigate the different diffusion behaviors

through the differences in morphology of microstructure. Unit cell (or REV) size is discussed depending on statistical analysis of effective diffusion calculations. Recasting the closure problem in 3-D unit cell, MCell can remarkably reduce computational effort.

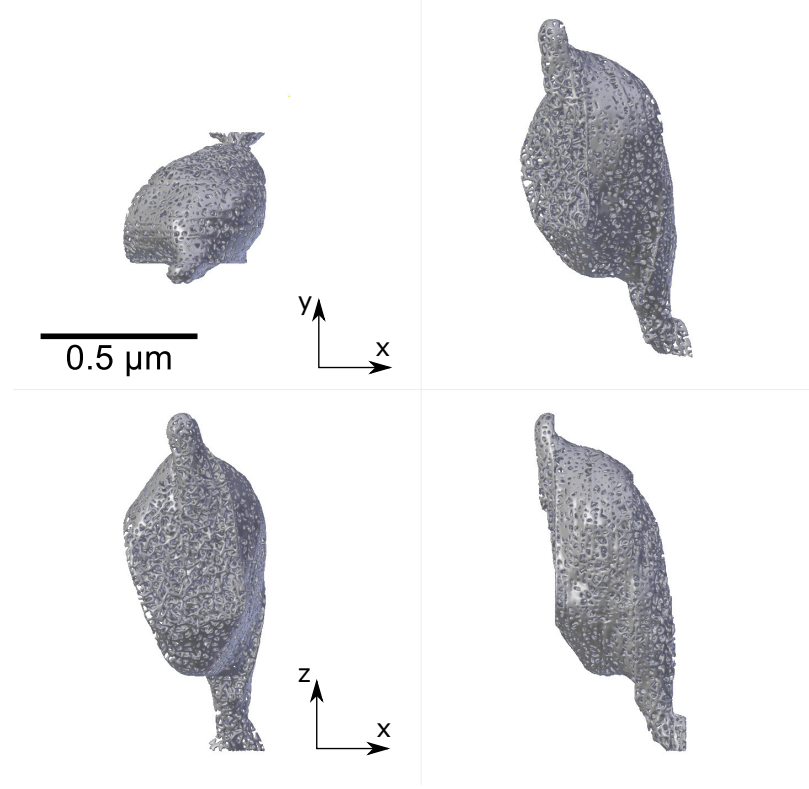
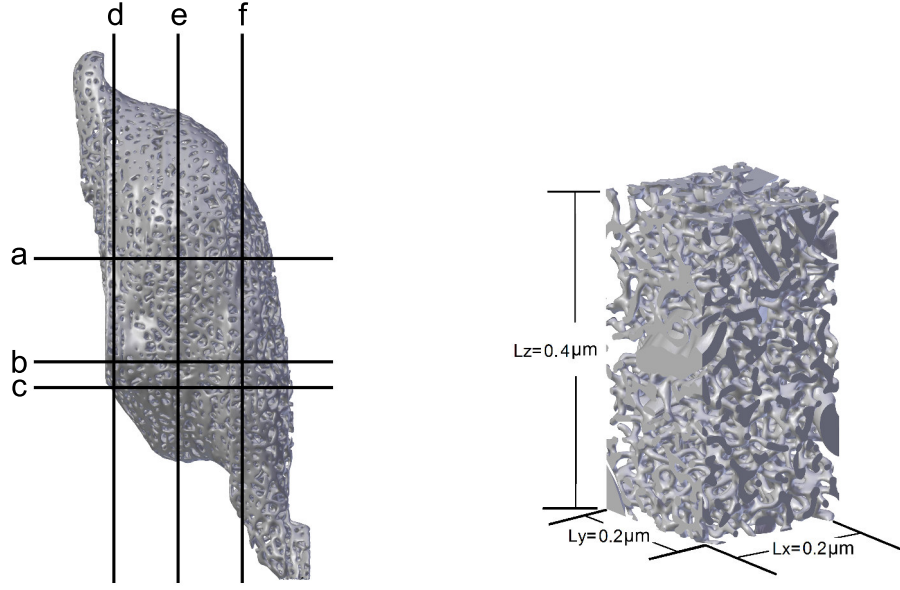


Figure 5.1: 3-D dendritic spine head model. Porosity of this F-actin network of the cytoskeleton is 0.689.

5.3 Effective transport properties of spine network structure

Diffusion transport model relating macroscopic anisotropic diffusion coefficients to the complexity of the F-actin network is obtained with homogenization via multiple-



(a) Cross section sample in XY and XZ planes (b) 3-D representative volume element

Figure 5.2: 2-D cross sections sampling and 3-D representative volume element.

scale expansion [110]. The effective anisotropic diffusion coefficients unveiling transport features of the microscale spine structure Fig.5.1 help to understand biochemical signaling and molecular interactions within the spine affected by the changes in synaptic structure. Meanwhile effective diffusive transport properties of this spine structure can quantify the travel time of transmitting chemical signals in the spine.

5.3.1 Problem formulation

We consider a nanoporous material Ω with a characteristic length L , and let \mathcal{P} denote the part of this material occupied by pores whose characteristic length scale, e.g., a typical pore diameter, is l such that $\epsilon \equiv l/L \ll 1$. The impermeable solid skeleton \mathcal{S} occupies the rest of the porous material, i.e., $\Omega = \mathcal{P} \cup \mathcal{S}$. The multiconnected boundary between the pore space \mathcal{P} and solid skeleton \mathcal{S} is denoted

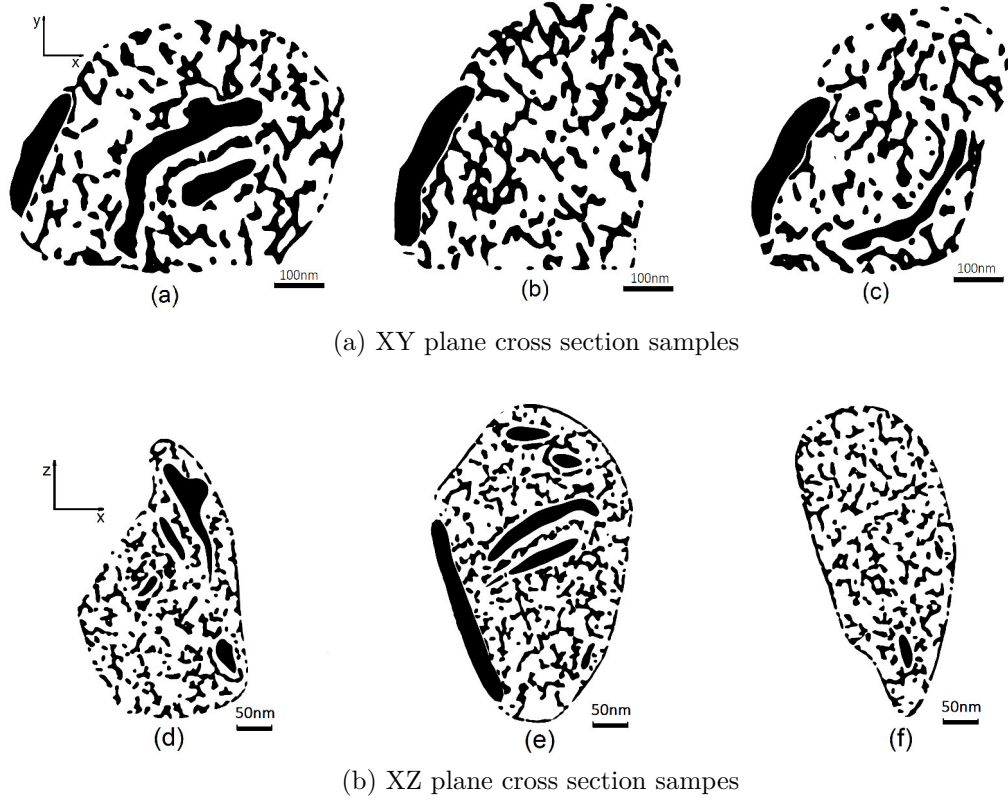


Figure 5.3: XY plane and XZ plane cross sections of 3-D actin spin model in Fig. 5.2a

by Γ .

The pore space \mathcal{P} is occupied by a fluid, which contains a solute with concentration $c(\mathbf{x}, t)$ [mol/m³], where \mathbf{x} denotes a point in \mathcal{P} and t is time. The solute diffuses throughout the pore space \mathcal{P} , taking place in isothermal conditions. This process is described by a diffusion equation

$$\frac{\partial c}{\partial t} + \nabla \cdot (-D \nabla c) = 0, \quad \mathbf{x} \in \mathcal{P}, \quad t > 0. \quad (5.1)$$

Here $D[\text{L}^2/\text{T}]$ is the diffusion coefficient. Analysis presented below is capable of handling spatially variable and anisotropic diffusion coefficients, we use constant

diffusion coefficient D to simplify the presentation.

Mass conservation along the impermeable solid-fluid interface Γ requires the normal component of the solute mass flux $-D\nabla c$ to be balanced by the rate of change (surface reaction) at the solid-fluid interface. Here we assume no interaction between solid and fluid at the interface, i.e.,

$$-\mathbf{n} \cdot (D\nabla c) = 0, \quad \mathbf{x} \in \Gamma, \quad t > 0. \quad (5.2)$$

5.3.2 Macroscopic properties of porous material

Macroscopic representations of a nanoporous material Ω treat it as a continuum, without separating it into the pore space \mathcal{P} and the solid skeleton \mathcal{S} . Macroscopic solute concentration $C(\mathbf{x}, t)$ —the microscopic concentration $c(\mathbf{y}, t)$ averaged over a (representative elementary) volume V centered at point $\mathbf{x} \in \Omega$ —is defined as

$$C(\mathbf{x}, t) \equiv \frac{1}{\|\mathcal{P}_V\|} \int_{\mathcal{P}_V(\mathbf{x})} c(\mathbf{y}, t) d\mathbf{y}, \quad (5.3)$$

where $\|\mathcal{P}_V\|$ is the total volume of pores contained in V .

We show in Appendix E that, for materials composed of periodic arrangements of unit cells \mathcal{U} , the macroscopic concentration $C(\mathbf{x}, t)$ satisfies a diffusion equation

$$\varepsilon \frac{\partial C}{\partial t} = \nabla \cdot (\mathbf{D}^{\text{eff}} \nabla C), \quad (5.4)$$

where $\varepsilon \equiv \|\mathcal{P}_V\|/\|V\| = \|\mathcal{P}_\mathcal{U}\|/\|\mathcal{U}\|$ is the porosity (with $\mathcal{P}_\mathcal{U}$ denoting the pore space

of the unit cell \mathcal{U}); and the effective diffusion tensor \mathbf{D}^{eff} defined as

$$\mathbf{D}^{\text{eff}} = \frac{D}{\|\mathcal{U}\|} \int_{\mathcal{P}_{\mathcal{U}}} (\mathbf{I} + \nabla_{\mathbf{y}} \boldsymbol{\chi}) d\mathbf{y}. \quad (5.5)$$

Here \mathbf{I} is the identity matrix, and the “closure variable” $\boldsymbol{\chi}(\mathbf{y})$ is a \mathcal{U} -periodic vector defined on $\mathcal{P}_{\mathcal{U}}$. It satisfies

$$\nabla_{\mathbf{y}}^2 \boldsymbol{\chi} = \mathbf{0}, \quad \mathbf{y} \in \mathcal{P}_{\mathcal{U}}; \quad \langle \boldsymbol{\chi}(\mathbf{y}) \rangle \equiv \frac{1}{\|\mathcal{U}\|} \int_{\mathcal{P}_{\mathcal{U}}} \boldsymbol{\chi}(\mathbf{x}) d\mathbf{y} = \mathbf{0} \quad (5.6)$$

subject to the boundary condition along the fluid-solid segments $\Gamma_{\mathcal{U}}$ of the boundary of $\mathcal{P}_{\mathcal{U}}$,

$$-\mathbf{n} \cdot (\nabla_{\mathbf{y}} \boldsymbol{\chi} + \mathbf{I}) = 0, \quad \mathbf{y} \in \Gamma_{\mathcal{U}}. \quad (5.7)$$

The rigorous derivation of closure equations enables one to express the diffusion coefficient tensor (5.5) in terms of the pore structure. Following from (5.6) that the off-diagonal elements of the second-rank tensor $\nabla_{\mathbf{y}} \boldsymbol{\chi}^{\top}$ are zeros, i.e., $\partial \chi_i / \partial y_k = 0$ for $i \neq k$. Consequently, the off-diagonal elements of the diffusion tensors \mathbf{D}^{eff} are zero as well.

5.4 Results and discussion

Unit cells are considered as a function of porosity (pore fraction of the constituents). 3-D dendritic spine model has porosity of 0.689. The porosity of sample unit cells chosen from each XY-plane and XZ-plane cross sections should be consistent with model global porosity, see Fig. 5.6.

Effective diffusion coefficients are computed through solving closure problems in sample cells in Fig. 5.4. Fig. 5.5 shows the solution to closure variable χ in a sample unit cell. From eq.(5.5), the effective diffusion coefficients can be computed. We extract a sufficient large number of unit cells in XY-plane with porosity variance of $\sigma_\varepsilon = 0.0006$ which gives rise to the variance of calculated effective diffusion coefficients $D_{x,y}^{\text{eff}}$ up to $\sigma_x = \sigma_y = 0.0045$ (See Fig. 5.8). Due to the largely variant morphology in XY-plane and XZ-plane shown in Fig.5.4, for the same size of unit cells extracted in XZ-plane with porosity variance of $\sigma_\varepsilon = 0.0006$, the calculated effective diffusion coefficients $D_{x,z}^{\text{eff}}$ have variances of $\sigma_x = \sigma_z = 0.002$ (Fig. 5.7). This implies the unit cell size in XZ plane is sufficiently large to represent microstructure because when increasing cell size, the variance of computed effective diffusion properties decreases.

Following discusses the anisotropy of spine material respective to factors like porous morphology and tortuosity. The representative elementary size of unit cells is estimated. For a given precision of effective diffusion coefficients, cell size should account for actin grown pattern in each direction.

5.4.1 Porosity

The porosity of all unit cells satisfies Gaussian distribution with mean of 0.685 which is consistent with global porosity and a variance of $\sigma_\varepsilon = 0.0006$ (See Fig.5.6). It is clear in general that larger porosity (volume fraction) results more paths for molecules to diffuse. However, the fluctuations of effective diffusion coefficients Fig.5.8 cannot be barely explained by porosity. Calculated XY-plane and XZ-plane effective properties show that D_x^{eff} , D_y^{eff} and D_z^{eff} have anisotropic behaviors which are highly influenced by microscopic structures of actin Fig.5.7, Fig.5.8.

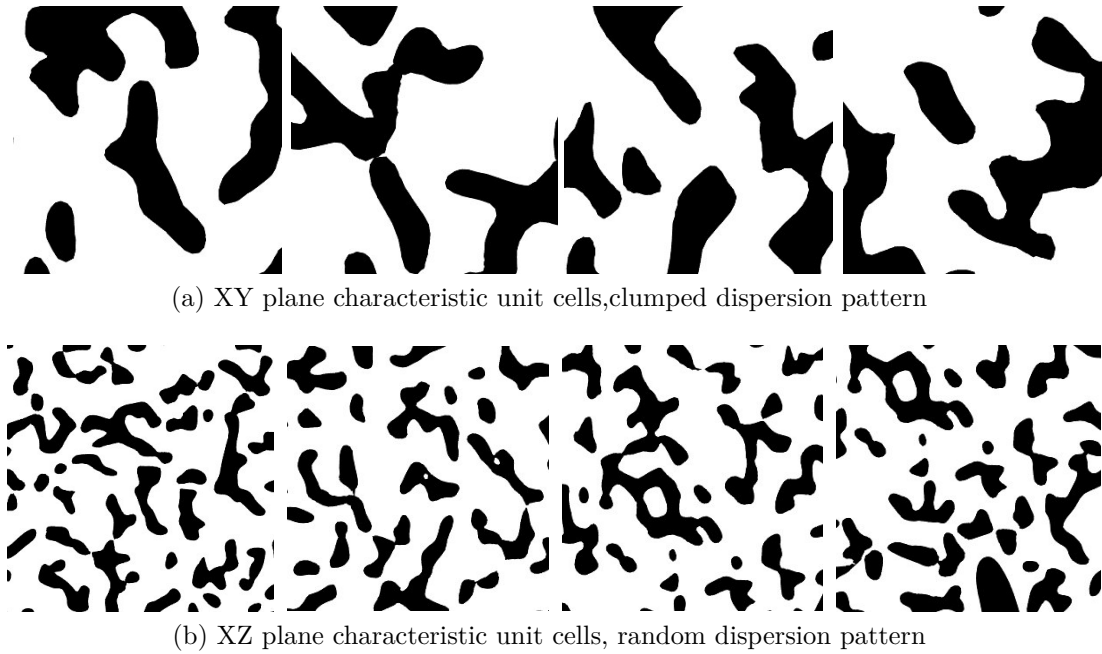


Figure 5.4: Unit cells \mathcal{U} in XY and XZ planes. The \mathcal{U} -periodicity of $\chi(\mathbf{x})$ is enforced. For the same representative cell size of $100 \text{ nm} \times 100 \text{ nm}$, distinguishable differences of morphology of unit cells are observed.

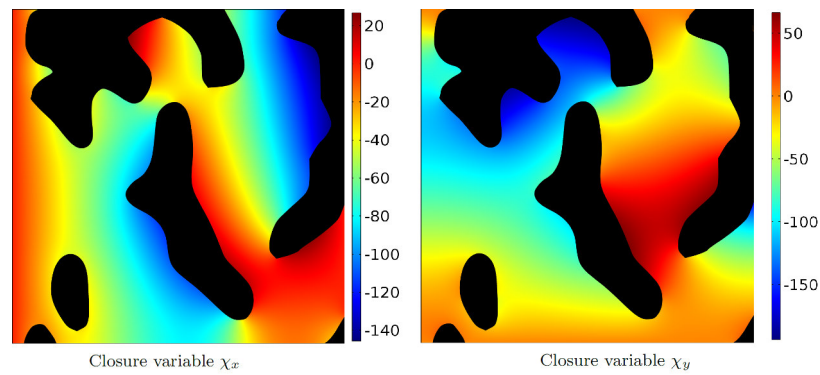


Figure 5.5: Simulation results of closure variable χ of the first unit cell in Fig. 5.4a

Unlike in XY-plane, the effective diffusion coefficients in XZ-plane Fig.5.7, presented as D_x^{eff} and D_z^{eff} , show a linearly-like dependence on porosity. As explained, the unit cells extracted from XZ-plane are sufficiently large that fluctuations of microstructure are compensated by averaging over large representative cell.

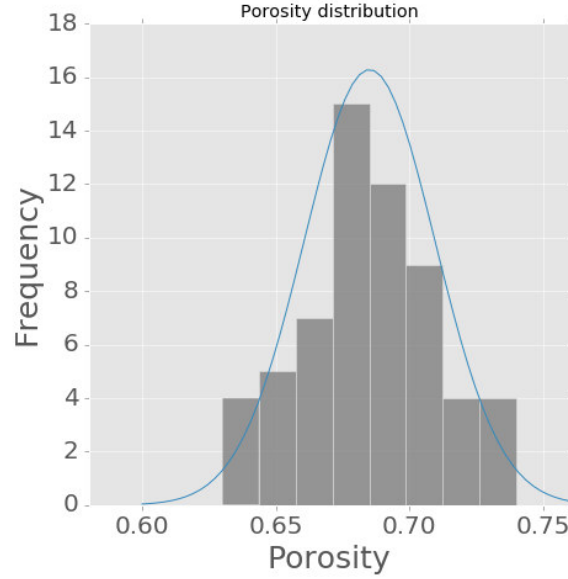


Figure 5.6: Porosity of selected unit cell satisfies Gaussian distribution. Mean value of porosity of all samples, consistent in XY-plane and XZ-plane, is 0.685.

5.4.2 Porous morphology

Aside from the influence of porosity, we dig into the microscale information of sample cells that can explain the statistical results of effective diffusion behaviors in all directions (See Fig. 5.7 and Fig. 5.8). Sample cells in Fig. 5.4 selected from multiple XY-plane and XZ-plane cross-sections represent typical actin grown pattern – random and clumped interior structures. Actin in XY-plane clumps into a larger size than that in XZ-plane which implies the characteristic length in XY plane is larger than that in XZ-plane. This clumped formation requires a larger cell size to adequately

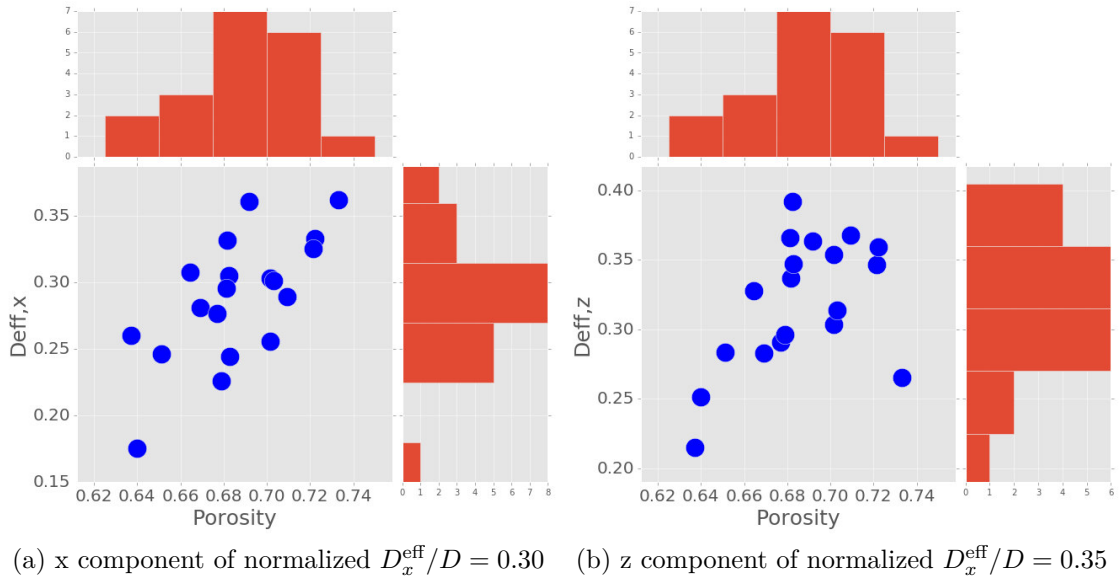


Figure 5.7: Dependency of effective diffusion coefficients and porosity in XZ plane

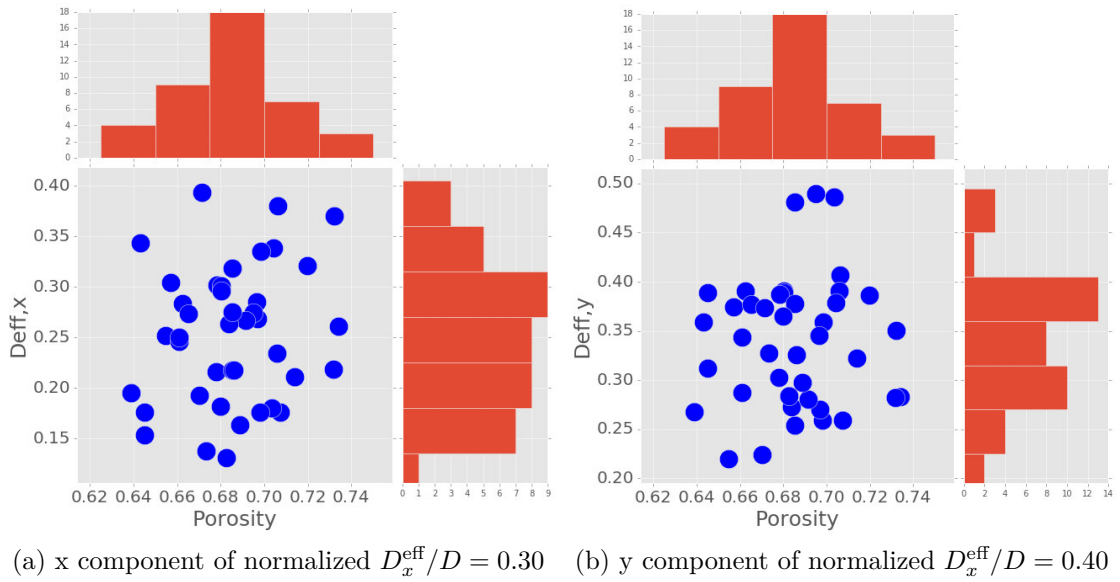


Figure 5.8: Dependency of effective diffusion coefficients and porosity in XY plane

present macroscopic transport properties. Cell size smaller than representative cell size can induce microstructure uncertainties and can not be accurately used to predict effective transport properties.

Clumped actin formation in XY-plane Fig. 5.4a results oval or strip like geometry lying vertically which significantly decreases x direction transport. The calculation of D_x^{eff} is about 25% smaller than that in y direction. As well in XZ-plane, smaller size actin strip-like geometry randomly distributed in vertical i.e., z direction. Because of strip-like geometry, the statistical results in Fig. 5.7 shows z direction has better diffusion transport ($D_z^{\text{eff}} > D_x^{\text{eff}}$).

While randomly grown actin Fig. 5.4b enlarges the interface region for trapping particles which is one kind of structure modes used for compromising the transport ability and interface area. The consequential effective diffusion in z direction D_z^{eff} is slightly smaller than D_y^{eff} . In favor of increasing surface area for surface reaction and studies of solid and particle interactions, we can emphasize on random structure.

5.4.3 Tortuosity

This effective diffusion linear-like dependence on porosity in XZ-plane suggests an alternative description of effective diffusion coefficients. Next we will discuss the geometries of porous material and their accumulative grown pattern on effective diffusion coefficients in terms of tortuosity. The basic idea of introducing tortuosity is to account for microstructure without solving computational intense microscale model. This additional porous materials variable serves as a parameter in macroscopic theories dealing with transport in complex porous media. Such material property is obtained in this work via rigorously derived model for relating effective diffusion

coefficients to microscopic actin grown pattern. Therefore, this alternative description can facilitate the prediction of effective diffusion for other dendritic spin network with similar actin grown features.

Tortuosity as an introduced additional parameter is attempted to generalize effects which take care of the more complicated transport paths neglected in the model. As a physical quantity, it can be defined in various ways. The preferred definition depends on the context and on the model being used. The most intuitive and straightforward definition is that of the ratio of the average length of true flow paths to the length of the system in the direction of the macroscopic flux. Tortuosity depends not only on the microscopic geometry of the pores, but also on the transport process undergoing[51]. The concept of tortuosity is often introduced in the context of solving the closure problem for transport in porous media, i.e., in deriving the macroscopic transport equations in terms of averaged quantities alone[81]. We define,

$$D^{\text{eff}} = D \frac{\varepsilon}{\tau}, \quad (5.8)$$

where D^{eff} is effective diffusion coefficient for solute or molecule transport; D is free-water diffusion coefficient or molecule diffusion coefficient; ε is porosity of material; and τ is a tortuosity factor that accounts for the reduction diffusion caused by tortuous path lengths in porous materials.

Here we use effective D_x^{eff} (x component effective diffusion coefficient) to address tortuosity in x direction. Fig. 5.7 and Fig. 5.8 conclude the mean value of D_x^{eff} is 0.30, gives $\tau_x = \frac{\varepsilon}{D_x^{\text{eff}}/D} = 2.36$. Same for getting $\tau_y = 1.7$ and $\tau_z = 1.95$. Larger tortuosity τ_x stands for longer true flow path for particle to diffuse in x direction. It's hard to

distinguish by eye that z-direction is less tortuous than x and y direction from Fig. 5.3. Tortuosity gives accumulated pore morphological effects and is very straightforward to present material structure. The tortuosity obtained in our work can instructively apply to similar actin network to predict effective transport properties.

5.5 Future work – MCell simulation

The closure problem (5.6) can also be solved through MCell which uses Monte Carlo algorithms to track the Brownian dynamics random-walk diffusion of discrete particles (e.g. molecules) in complex 3-D spaces. The motions of individual particles are tracked by ray-tracing their trajectories through space and their collisions and interactions with other particles and boundaries embedded in the space. Boundaries are represented as triangulated 2-D manifold surfaces embedded in 3-D space. Boundaries can be given reflective, absorptive, or emissive properties with respect to particle identities[20]. MCell’s particle-based Monte Carlo reaction/diffusion algorithms can be much more computationally efficient than PDE-based numerical methods especially in cases involving complex geometry and boundary conditions. The main disadvantages of PDE-based methods are due to the requirement to create complex, computational quality tetrahedral meshes – a tetrahedral mesh of the whole spine with F-actin network would be composed of billions of mesh elements. In contrast MCell requires only triangulated 2-D meshes of the boundaries – about 1.7 million triangles for the full F-actin network. Future work is to solve 3-D unit cell Fig. 5.2b with MCell to reduce computational effort.

To solve this closure problem with MCell we recast the problem formulated in equations (5.6), and (5.7) as a steady-state diffusion problem in a period unit cell

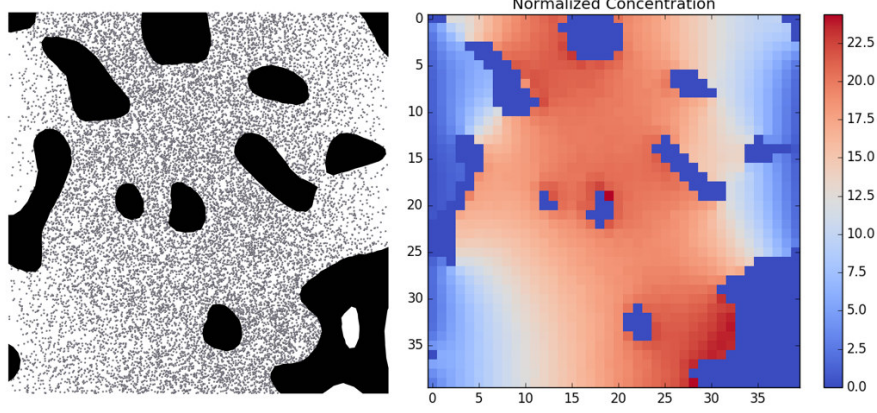


Figure 5.9: MCell simulation of 2-D unit cell. (a) is particle distribution at steady state. Porosity of this unit cell is $\varepsilon = 0.757$ (COMSOL result). (b) is the spatial distribution of the closure variable $\chi_x(y_1, y_2)$. Porosity prediction using MCell is 0.83. Smaller voxel size is needed for MCell to increase accuracy.

in which Neumann (i.e. constant flux) boundary conditions are imposed on the solid boundaries. The value of the spatial distribution of $\chi(y_1, y_2)$ is the total number of particles in each voxel when the diffusion process is at steady state. (See Fig. 5.9) From eq.(5.5) it can be seen that the effective diffusion coefficients can be computed by integrating over the gradient vector field of χ .

5.6 Conclusions

In this paper, we use homogenization to calculate effective properties of 3-D dendritic spine models. The upscaling method can be widely used to determine effective properties of various porous materials as well as microstructure design and optimization. Through 2-D unit cells drawn from plane cross sections, effective diffusion coefficients of this dendritic spine are evaluated. The effects of porosity, porous morphology and pore tortuosity on effective diffusion coefficients are discussed. The computations show that:

- Porosity of sample cells collected from both XY-plane and XZ-plane is inherent in consistence with global porosity. As shown in Fig. 5.7 and Fig. 5.8, besides porosity, microscopic structures strikingly play roles on transport abilities. Larger porosity enables more space for molecules to diffuse which generally gives a larger effective diffusion coefficients. Porous morphology analysis discovers even for the same porosity, a random actin structure may cause larger diffusion length and result in a lower effective diffusion in relative to clumped structure. Clumped geometry and orientation determine the anisotropy of the material.
- An additional parameter tortuosity τ is introduced. It illustrates more complicated transport paths by the ratio of the average length of true transport path to the length of the system in the direction of the macroscopic flux. Calculation shows that x direction has larger τ_x , y and z directions have smaller τ_y, τ_z .

5.7 Acknowledgements

This Chapter is currently being prepared for submission for peer review and publication: Zhang, X., Bartol, T. and Tartakovsky, D.M., 2016. Effective transport properties for dendritic spine F-actin network. Biophysical Journal. The dissertation author was the primary investigator and author on this paper.

Chapter 6

Conclusions

This research integrates multiscale studies and analyses of transport phenomena in hierarchical nanoporous materials. The main contribution of this research is the introduction of robust and efficient analytical methods for capturing with anisotropic macroscopic properties of porous media and improving the current approximations of effective diffusion coefficients and electrolyte conductivities in porous electrodes materials.

The fundamental features of this research impact several disciplines. The results obtained for non-equilibrium Langmuir-type adsorption reactions can be used to capture microscale fluid-solid surface sorption on the macroscopic behavior of nanoporous materials. The new insights into the electrical double layer formation at the pore scale are crucial for many interfacial phenomena, especially for the design of the pore structure of porous electrodes. The results obtained by using the electrical double layer modification for macroscopic charged ion transport show remarkable congruence with experimental data from electrical double layer capacitors. The models developed for the solvent transport in nanoporous materials under the influence of

electrical double layer potential and dynamic Langmuir-type adsorption provide insight into design and tailoring of nanoporous materials for separation and energy storage applications. Based on the analytical analysis and modeling results, the following specific conclusions are drawn.

Homogenization theory (or other upscaling techniques) provides a means of bridging pore-scale structure and macroscopic properties:

- By relating these two scales, the possibilities of designing materials with desired macroscopic properties (e.g., diffusion coefficient and adsorption capacity) are raised by using controllable pore-scale parameters (e.g., pore size and connectivity). Such analysis is applicable for solute that undergo a non-equilibrium Langmuir adsorption reaction on the surface of fluid filled pores, as well as other homogeneous and heterogeneous reactions. The presented results can be used to guide the design of nanoporous materials with optimal permeability and sorption capacity.

A class of porous materials designed by embedding micro-tubes in microporous materials is applied to study the adsorption capacity and anisotropic effective diffusion coefficients. Optimization results indicate that despite the negligible contribution of tubes to the porosity of this nanoporous material, the tube bridges significantly alter its diffusive properties. They also nearly double the effective reaction constant γ_{eff} . While the number of microporous tubes in a bridge, n , does not appreciably affect the material's diffusive properties in longitudinal and horizontal directions, it significantly influences its adsorbing capacity (γ_{eff})

- The effect of electrical double layer (EDL) formation in charged porous electrode

materials on macroscopic diffusion coefficients and electrolyte conductivities are studied. The macroscopic diffusion coefficients incorporating porous structure and local electric potential determined by EDL are derived through multi-scale analysis. The modifications of effective diffusion and electrolyte conductivities indicate, for dilute solutions, diverse electrolyte concentrations and charged conditions can vary macroscopic ion diffusion through their impacts on EDL.

This effective model of predicting porous electrode effective diffusion coefficients, electrolyte conductivities and transference number improves the understanding of phenomenal pore scale transport contrast to Bruggeman empirical relation. Especially for the conditions that pore size is of the same order of magnitude as the electrical double layer thickness, Bruggeman relation overestimates the effective diffusion coefficients.

- Considering the impact of pore size, local electric potential and porous structure, closure problems based periodic unit cell of porous materials are solved. For dilute solution, however, micropore size is of the same order of magnitude as the electrical double layer thickness. In this condition, micropores notably restrain the mesopores' performance. Regardless of micropore's dominant contribution to high surface area, pore accessibility is restricted and ion transport is impeded by electrical double layer formation.

Two different material morphologies are used to optimize micro/meso-pore pairs for different EDL conditions. For maintaining micropore's high surface area features and balancing the flexibility of transport, optimization presents a general $3 \sim 4$ nm mesopore size and micropore size of 1.5 nm (for solution concentration $c > 0.01$ M) result. Morphology 2 (Material 2) has better transport capabilities

in both directions and higher specific surface area. The lower bound condition of concentration is discussed and concluded. For very dilute concentration ($c_{\text{in}} = 0.01 \text{ M}$), double layer overlapping will cause deceleration of transport in porous materials.

- A detailed microscopic three dimensional F-actin network model is launched and macroscopic effective diffusion coefficients of a dendritic spine network are evaluated. The effects of porosity, porous morphology and pore tortuosity on the effective diffusion coefficients are discussed.

Sample cells collected from both xy-plane and xz-plane are consistently inherent in global porosity and minimum statistical request for same $D_{\text{eff},x}$. Calculated effective diffusion coefficients indicate that besides porosity, microscopic structures play dramatically roles on determining transport abilities. Larger porosity enables more space for molecules to diffuse which generally gives a larger effective diffusion coefficients. The porous morphology analysis reveals that, even for the same porosity, a random actin packing may cause longer length of diffusion and result in a lower effective diffusion in relative to a clumped packing mode. Clumped geometry and orientation determine the anisotropy of the material. An additional parameter tortuosity τ is introduced. As calculated from effective diffusion coefficients in all directions in, x direction has larger τ_x , y and z directions have smaller τ_y and τ_z .

Appendix A

Derivation of the boundary condition

Rewriting (2.2) and (2.3) in terms of the dimensionless quantities (2.5) yields

$$-\mathbf{n} \cdot \nabla c = q_m \frac{\partial s}{\partial t}, \quad \text{and} \quad \frac{ds}{dt} = \text{Da} (s_{\text{eq}} - s). \quad (\text{A.1})$$

In a typical application of nanoporous materials, e.g., mesoporous catalyst membranes, the characteristic macroscopic length (membrane size) is[73] $L \sim 100 \mu\text{m}$ and the characteristic pore scale is[62] $l \sim 20 - 100 \text{ nm}$. Hence the length-scale ratio is $\epsilon \equiv l/L \sim 10^{-4}$. Moreover, the characteristic time scale of adsorption processes in mesoporous membranes, e.g., for methylene blue, is[62, 34] $1/\gamma \sim 40 - 80 \text{ min}$, while its diffusion coefficient is [52] $D \sim 10^{-5} \text{ cm}^2\text{s}^{-1}$. Hence, the Damköhler number is $\text{Da} \sim \mathcal{O}(10^{-3})$, which allows its use as a small perturbation parameter.

Consider an asymptotic expansion of $s(\mathbf{x}, t)$ in the powers of Da , $s = s_0 + \text{Da} s_1 + \mathcal{O}(\text{Da}^2)$. Substituting this expansion into the second equation in (A.1) and

collecting the terms of equal powers of Da yields

$$\frac{ds_0}{dt} = 0 \quad \text{and} \quad \frac{ds_1}{dt} = s_{\text{eq}} - s_0. \quad (\text{A.2})$$

For the homogenous initial condition, $s(\mathbf{x}, 0) = 0$, this yields $s_0 = 0$ and $ds_1/dt = Kc/(1 + Kc)$. Hence, the first-order approximation of the sorbed concentration, $s \approx s_0 + \text{Da } s_1$, gives rise to

$$\frac{ds}{dt} \approx \text{Da} \frac{Kc}{1 + Kc}. \quad (\text{A.3})$$

Substituting this approximation into (A.1) yields (2.6a).

Appendix B

Homogenization of transport equations

Three types of local average of a quantity $A(\mathbf{x}, t)$ are defined

$$\langle A \rangle \equiv \frac{1}{\|\mathcal{U}\|} \int_{\mathcal{P}_{\mathcal{U}}(\mathbf{x})} A d\mathbf{y}, \quad \langle A \rangle_{\mathcal{P}} \equiv \frac{1}{\|\mathcal{P}_{\mathcal{U}}\|} \int_{\mathcal{P}_{\mathcal{U}}(\mathbf{x})} A d\mathbf{y}, \quad \langle A \rangle_{\Gamma} \equiv \int_{\Gamma_{\mathcal{U}}(\mathbf{x})} A d\mathbf{y}, \quad (\text{B.1})$$

such that $\langle A \rangle = \phi \langle A \rangle_{\mathcal{P}}$ where $\phi = \|\mathcal{P}_{\mathcal{U}}\|/\|\mathcal{U}\|$ is the porosity. We use the multiple-scale expansion technique [42, 14] to derive effective continuum scale equations for average concentration $C(\mathbf{x}, t) \equiv \langle c(\mathbf{x}, t) \rangle$. The method postulates that concentration exhibits both large-scale (across the porous material, denoted by the coordinate \mathbf{x}) and small-scale (inside individual pores, denoted by the coordinate \mathbf{y}) spatial variability, such that $\mathbf{y} = \epsilon^{-1} \mathbf{x}$ with $\epsilon \ll 1$; the corresponding temporal scales are denoted, respectively, by t and $\tau_r = \text{Da } t$ where Da is the Damköhler number.

Let us introduce a membership (indicator) function $\Pi(\mathbf{x}) = \Pi(\mathbf{x}/\epsilon)$,

$$\Pi(\mathbf{x}) = \begin{cases} 1, & \mathbf{x} \in \mathcal{P} \\ 0, & \mathbf{x} \in \mathcal{S}. \end{cases} \quad (\text{B.2})$$

For the nanoporous materials under consideration, the function $\Pi(\mathbf{x}) = \Pi(\mathbf{x}/\epsilon)$ is periodic on the unit cell \mathcal{U} . This allows one to define the pore-scale diffusion equation (2.6b) on the whole unit cell \mathcal{U} (rather than on the multi-connected subdomain $\mathcal{P}_{\mathcal{U}}$ occupied the liquid),

$$\frac{\partial c}{\partial t} = \nabla \cdot (\Pi \nabla c), \quad \mathbf{y} \in \mathcal{U}, \quad t > 0. \quad (\text{B.3})$$

Replacing the concentration $c(\mathbf{x}, t)$ with $c(\mathbf{x}, \mathbf{y}, t, \tau_r)$ and substituting into Eq. (B.3) yields

$$\frac{\partial c}{\partial t} + \text{Da} \frac{\partial c}{\partial \tau_r} = \nabla_{\mathbf{x}} \cdot [\Pi(\nabla_{\mathbf{x}} c + \epsilon^{-1} \nabla_{\mathbf{y}} c)] + \epsilon^{-1} \nabla_{\mathbf{y}} \cdot [\Pi(\nabla_{\mathbf{x}} c + \epsilon^{-1} \nabla_{\mathbf{y}} c)], \quad \mathbf{y} \in \mathcal{U}. \quad (\text{B.4a})$$

The interfacial condition (2.6a) takes the form

$$-\mathbf{n} \cdot (\nabla_{\mathbf{x}} c + \epsilon^{-1} \nabla_{\mathbf{y}} c) = \text{Da} q_m \frac{Kc}{1 + Kc}, \quad \mathbf{y} \in \Gamma_{\mathcal{U}}. \quad (\text{B.4b})$$

In the multiple-scale expansion method, the concentration $c(\mathbf{x}, \mathbf{y}, t, \tau_r)$ is represented by an asymptotic series

$$c(\mathbf{x}, \mathbf{y}, t, \tau_r) = \sum_{m=0}^{\infty} \epsilon^m c_m(\mathbf{x}, \mathbf{y}, t, \tau_r). \quad (\text{B.5})$$

Substituting Eq. (B.5) into Eqs. (B.4), approximating the Langmuir adsorption isotherm with a series

$$\begin{aligned} \frac{Kc}{1+Kc} &= 1 - \frac{1}{1+Kc} = 1 - \left[1 - K(c_0 + \epsilon c_1) + K^2(c_0^2 + 2\epsilon c_1 c_0) \right] + \mathcal{O}(\epsilon^2), \\ &= Kc_0 - K^2 c_0^2 + \epsilon(Kc_1 - 2K^2 c_0 c_1) + \mathcal{O}(\epsilon^2), \end{aligned} \quad (\text{B.6})$$

and recalling from Appendix A that $\text{Da} \sim \mathcal{O}(\epsilon^1)$, we obtain

$$\begin{aligned} & -\epsilon^{-2} \nabla_{\mathbf{y}} \cdot (\Pi \nabla_{\mathbf{y}} c_0) \\ & - \epsilon^{-1} \{ \nabla_{\mathbf{x}} \cdot (\Pi \nabla_{\mathbf{y}} c_0) + \nabla_{\mathbf{y}} \cdot [\Pi(\nabla_{\mathbf{y}} c_1 + \nabla_{\mathbf{x}} c_0)] \} \\ & + \epsilon^0 \left\{ \frac{\partial c_0}{\partial t} - \nabla_{\mathbf{x}} \cdot [\Pi(\nabla_{\mathbf{x}} c_0 + \nabla_{\mathbf{y}} c_1)] - \nabla_{\mathbf{y}} \cdot [\Pi(\nabla_{\mathbf{x}} c_1 + \nabla_{\mathbf{y}} c_2)] \right\} = \mathcal{O}(\epsilon^1), \quad \mathbf{y} \in \mathcal{U} \end{aligned} \quad (\text{B.7})$$

and

$$\begin{aligned} & -\epsilon^{-1} \mathbf{n} \cdot \nabla_{\mathbf{y}} c_0 - \epsilon^0 [\mathbf{n} \cdot (\nabla_{\mathbf{x}} c_0 + \nabla_{\mathbf{y}} c_1)] \\ & - \epsilon^1 [q_m(Kc_0 - K^2 c_0^2) + \mathbf{n} \cdot (\nabla_{\mathbf{x}} c_1 + \nabla_{\mathbf{y}} c_2)] = \mathcal{O}(\epsilon^2), \quad \mathbf{y} \in \Gamma_{\mathcal{U}}. \end{aligned} \quad (\text{B.8})$$

Collecting terms of the equal powers of ϵ yields boundary-value problems (BVPs) for $c_m(\mathbf{x}, \mathbf{y}, t, \tau_r)$ ($m = 0, 1, \dots$).

Leading-order term, $\mathcal{O}(\epsilon^{-2})$. Collecting the $\mathcal{O}(\epsilon^{-2})$ terms yields a BVP for the leading-order term in the expansion (B.5),

$$\nabla_{\mathbf{y}} \cdot (\Pi \nabla_{\mathbf{y}} c_0) = 0, \quad \mathbf{y} \in \mathcal{U}; \quad -\mathbf{n} \cdot \nabla_{\mathbf{y}} c_0 = 0, \quad \mathbf{y} \in \Gamma_{\mathcal{U}}. \quad (\text{B.9})$$

This BVP has a trivial solution, which implies that c_0 is independent of \mathbf{y} .

Term of order $\mathcal{O}(\epsilon^{-1})$. Since $\text{Da} \sim \mathcal{O}(\epsilon^1)$, collecting the $\mathcal{O}(\epsilon^{-1})$ terms yields a BVP for the first-order term in the expansion (B.5),

$$\nabla_{\mathbf{y}} \cdot [\Pi(\nabla_{\mathbf{x}}c_0 + \nabla_{\mathbf{y}}c_1)] = 0, \quad \mathbf{y} \in \mathcal{U} \quad (\text{B.10a})$$

subject to the interfacial condition

$$-\mathbf{n} \cdot (\nabla_{\mathbf{x}}c_0 + \nabla_{\mathbf{y}}c_1) = 0, \quad \mathbf{y} \in \Gamma_{\mathcal{U}}. \quad (\text{B.10b})$$

Equations (B.10), which form a BVP for $c_1(\mathbf{x}, \mathbf{y}, t, \tau_r)$, define a local problem. It depends only on the geometry of the unit cell. We represent its solution as [42, 14]

$$c_1(\mathbf{x}, \mathbf{y}, t, \tau_r) = \boldsymbol{\chi}(\mathbf{y}) \cdot \nabla_{\mathbf{x}}c_0(\mathbf{x}, t, \tau_r) + \bar{c}_1(\mathbf{x}, t, \tau_r). \quad (\text{B.11})$$

Substituting this into Eq. (B.10a) yields an equation for the closure variable (a vector) $\boldsymbol{\chi}(\mathbf{y})$,

$$\nabla_{\mathbf{y}} \cdot (\mathbf{I} + \nabla_{\mathbf{y}}\boldsymbol{\chi})\nabla_{\mathbf{x}}c_0 = 0, \quad \mathbf{y} \in \mathcal{P}_{\mathcal{U}} \quad (\text{B.12})$$

This equation is subject to $\langle \boldsymbol{\chi} \rangle = \mathbf{0}$ and the boundary condition

$$\mathbf{n} \cdot (\mathbf{I} + \nabla_{\mathbf{y}}\boldsymbol{\chi})\nabla_{\mathbf{x}}c_0 = 0, \quad \mathbf{y} \in \Gamma_{\mathcal{U}}, \quad (\text{B.13})$$

which is obtained by substituting Eq. (B.11) into Eq. (B.10b).

Terms of order $\mathcal{O}(\epsilon^0)$. Collecting the terms of order ϵ (B.7) yields

$$\frac{\partial c_0}{\partial t} - \nabla_{\mathbf{x}} \cdot [\Pi(\nabla_{\mathbf{x}} c_0 + \nabla_{\mathbf{y}} c_1)] - \nabla_{\mathbf{y}} \cdot [\Pi(\nabla_{\mathbf{x}} c_1 + \nabla_{\mathbf{y}} c_2)] = 0, \quad \mathbf{y} \in \mathcal{U} \quad (\text{B.14a})$$

subject to the interfacial condition

$$-q_{\text{m}}(Kc_0 - K^2c_0^2) - \mathbf{n} \cdot (\nabla_{\mathbf{x}} c_1 + \nabla_{\mathbf{y}} c_2) = 0, \quad \mathbf{y} \in \Gamma_{\mathcal{U}}, \quad (\text{B.14b})$$

Integrating over \mathcal{U} with respect to \mathbf{y} , applying the interfacial conditions (B.14b), and accounting for the periodicity of $\Pi(\mathbf{y})$ on the boundary of the unit cell \mathcal{U} , we obtain

$$\frac{\partial c_0}{\partial t} - \nabla_{\mathbf{x}} \cdot (\phi^{-1} \langle (\mathbf{I} + \nabla_{\mathbf{y}} \chi) \rangle \nabla_{\mathbf{x}} c_0) + \gamma_{\text{eff}} q_{\text{m}}(Kc_0 - K^2c_0^2) = 0 \quad (\text{B.15})$$

where γ_{eff} is defined in Eq. (2.9), ϕ is the porosity and effective diffusion coefficient $\mathbf{D}_{\text{eff}}/D = \langle (\mathbf{I} + \nabla_{\mathbf{y}} \chi) \rangle$ is defined in (2.10).

Rewriting the linearized form of the Langmuir isotherm, $Kc_0 - K^2c_0^2$, in its original form, $Kc_0/(1 + Kc_0)$; approximating the solute concentration $c \approx c_0$; and defining its average over the cell as $C(\mathbf{x}, t) \equiv \langle c(\mathbf{x}, t) \rangle$ leads to the homogenized continuum-scale diffusion-reaction equation for the average concentration (2.8).

Appendix C

Homogenization of PNP equations

In the derivations below we drop the hats over the dimensionless quantities to simplify the notation. The “fast” (\mathbf{y}) and “slow” (\mathbf{x}) scales are related by $\mathbf{y} = \epsilon^{-1}\mathbf{x}$, with $\epsilon \ll 1$, such that $\nabla = \nabla_{\mathbf{x}} + \epsilon^{-1}\nabla_{\mathbf{y}}$. The state variables $c_b(\mathbf{x}, t)$ and $\varphi_b(\mathbf{x}, t)$ are replaced with their two-scale counterparts $c_b(\mathbf{x}, \mathbf{y}, t)$ and $\varphi_b(\mathbf{x}, \mathbf{y}, t)$, and the macroscopic (average) ion concentration and electric potential are defined as

$$C(\mathbf{x}, t) = \frac{\omega}{\|\mathcal{P}_{\mathcal{U}}\|} \int_{\mathcal{P}_{\mathcal{U}}} c_b(\mathbf{x}, \mathbf{y}, t) d\mathbf{y} \quad \text{and} \quad \Phi_{\text{av}}(\mathbf{x}, t) = \frac{\omega}{\|\mathcal{P}_{\mathcal{U}}\|} \int_{\mathcal{P}_{\mathcal{U}}} \varphi_b(\mathbf{x}, \mathbf{y}, t) d\mathbf{y}. \quad (\text{C.1})$$

Following the standard practice in homogenization, we postulate that the nanoporous material Ω can be viewed as an assemblage of periodically repeated unit cells \mathcal{U} , each of which consists of the fluid-filled pore space $\mathcal{P}_{\mathcal{U}}$ and solid phase $\mathcal{S}_{\mathcal{U}}$.

Since $\varphi_{\text{EDL}} = \varphi_{\text{EDL}}(\mathbf{y})$, $c_b = c_b(\mathbf{x}, \mathbf{y}, t)$ and $\varphi_b = \varphi_b(\mathbf{x}, \mathbf{y}, t)$, (3.11) yields

$$\begin{aligned} e^{\mp z \varphi_{\text{EDL}}} \frac{\partial c_b}{\partial t} = & e^{\mp z \varphi_{\text{EDL}}} \nabla_{\mathbf{x}} \cdot \{ \nabla_{\mathbf{x}} c_b + \epsilon^{-1} \nabla_{\mathbf{y}} c_b \pm z c_b (\nabla_{\mathbf{x}} \varphi_b + \epsilon^{-1} \nabla_{\mathbf{y}} \varphi_b) \} \\ & + \epsilon^{-1} \nabla_{\mathbf{y}} \cdot \{ e^{\mp z \varphi_{\text{EDL}}} [\nabla_{\mathbf{x}} c_b + \epsilon^{-1} \nabla_{\mathbf{y}} c_b \pm z c_b (\nabla_{\mathbf{x}} \varphi_b + \epsilon^{-1} \nabla_{\mathbf{y}} \varphi_b)] \}, \quad \mathbf{y} \in \mathcal{P}_{\mathcal{U}}. \end{aligned} \quad (\text{C.2a})$$

The interfacial condition (3.4) takes the form

$$\mathbf{n} \cdot [\nabla_{\mathbf{x}} c_b + \epsilon^{-1} \nabla_{\mathbf{y}} c_b \pm z c_b (\nabla_{\mathbf{x}} \varphi_b + \epsilon^{-1} \nabla_{\mathbf{y}} \varphi_b)] = 0, \quad \mathbf{y} \in \Gamma_{\mathcal{U}}. \quad (\text{C.2b})$$

Next, the state variables $c_b(\mathbf{x}, \mathbf{y}, t)$ and $\varphi_b(\mathbf{x}, \mathbf{y}, t)$ are expanded in asymptotic series in the powers of the small parameter ϵ ,

$$c_b(\mathbf{x}, \mathbf{y}, t) = \sum_{m=0}^{\infty} \epsilon^m c_m(\mathbf{x}, \mathbf{y}, t), \quad \varphi_b(\mathbf{x}, \mathbf{y}, t) = \sum_{m=0}^{\infty} \epsilon^m \varphi_m(\mathbf{x}, \mathbf{y}, t), \quad (\text{C.3})$$

where the functions $c_m(\mathbf{x}, \mathbf{y}, t)$ and $\varphi_m(\mathbf{x}, \mathbf{y}, t)$ are \mathcal{U} -periodic in \mathbf{y} . Substituting (C.3) into (C.2) and collecting the terms of equal powers of ϵ yields the following set of recursive boundary-value problems (BVPs) for the expansion coefficients c_i and φ_i ($i = 0, 1, \dots$).

Terms of order ϵ^{-2} . Collecting the terms of order ϵ^{-2} yields

$$\nabla_{\mathbf{y}} \cdot [\Pi c_0 e^{\mp z \varphi_{\text{EDL}}} (\nabla_{\mathbf{y}} c_0 \pm z c_0 \nabla_{\mathbf{y}} \varphi_0)] = 0, \quad \mathbf{y} \in \mathcal{P}_{\mathcal{U}} \quad (\text{C.4a})$$

subject to

$$\mathbf{n} \cdot (\nabla_{\mathbf{y}} c_0 \pm z c_0 \nabla_{\mathbf{y}} \varphi_0) = 0, \quad \mathbf{y} \in \Gamma_{\mathcal{U}} \quad (\text{C.4b})$$

This homogeneous BVP has a trivial solution, i.e., both c_0 and φ_0 are independent of \mathbf{y} . That indicates insignificant spatial variability of both bulk concentration and bulk potential at the pore scale.

Terms of order ϵ^{-1} . Since c_0 and φ_0 are independent of \mathbf{y} , collecting the terms of order ϵ^{-1} yields

$$\nabla_{\mathbf{y}} \cdot [e^{\mp z \varphi_{\text{EDL}}} \nabla_{\mathbf{y}} (c_1 \pm z c_0 \varphi_1)] = -\nabla_{\mathbf{y}} e^{\mp z \varphi_{\text{EDL}}} \cdot (\nabla_{\mathbf{x}} c_0 \pm z c_0 \nabla_{\mathbf{x}} \varphi_0), \quad \mathbf{y} \in \mathcal{P}_{\mathcal{U}} \quad (\text{C.5a})$$

subject to

$$\mathbf{n} \cdot \nabla_{\mathbf{y}} (c_1 \pm z c_0 \varphi_1) = -\mathbf{n} \cdot (\nabla_{\mathbf{x}} c_0 \pm z c_0 \nabla_{\mathbf{x}} \varphi_0), \quad \mathbf{y} \in \Gamma_{\mathcal{U}}. \quad (\text{C.5b})$$

This BVP involves both the fast and slow scales; to decouple these scales we introduce pore-scale \mathcal{U} -periodic closure variables [65, 66, 68, 83] $\chi_{\pm}(\mathbf{y})$, such that

$$c_1 \pm z c_0 \varphi_1 = \chi_{\pm} \cdot (\nabla_{\mathbf{x}} c_0 \pm z c_0 \nabla_{\mathbf{x}} \varphi_0). \quad (\text{C.6})$$

Substituting this closure approximation into (C.5) gives

$$\nabla_{\mathbf{y}} \cdot [e^{\mp z \varphi_{\text{EDL}}} (\mathbf{I} + \nabla_{\mathbf{y}} \chi_{\pm}^{\top}) (\nabla_{\mathbf{x}} c_0 \pm z c_0 \nabla_{\mathbf{x}} \varphi_0)] = 0, \quad \mathbf{y} \in \mathcal{P}_{\mathcal{U}} \quad (\text{C.7a})$$

subject to the boundary condition

$$-\mathbf{n} \cdot [(\mathbf{I} + \nabla_{\mathbf{y}} \chi_{\pm}^{\top}) (\nabla_{\mathbf{x}} c_0 \pm z c_0 \nabla_{\mathbf{x}} \varphi_0)] = 0, \quad \mathbf{y} \in \Gamma_{\mathcal{U}}. \quad (\text{C.7b})$$

These BVPs are turned into identities if the vector functions $\chi_{\pm}^{\top}(\mathbf{y})$ are defined as

solutions to the first two equations in (3.16). When supplemented with the third condition in (3.16), this definition ensures that a solution of the unit cell problem, i.e., the vector functions $\boldsymbol{\chi}_\pm^\top(\mathbf{y})$, is unique[9, 21, 7, 8].

Terms of order ϵ^0 . Collecting the terms of order ϵ^0 yields

$$\begin{aligned} e^{\mp z\varphi_{\text{EDL}}} \frac{\partial c_0}{\partial t} &= e^{\mp z\varphi_{\text{EDL}}} \nabla_{\mathbf{x}} \cdot \{ \nabla_{\mathbf{x}} c_0 + \nabla_{\mathbf{y}} c_1 \pm z c_0 (\nabla_{\mathbf{x}} \varphi_0 + \nabla_{\mathbf{y}} \varphi_1) \} \\ &+ \nabla_{\mathbf{y}} \cdot \{ e^{\mp z\varphi_{\text{EDL}}} [\nabla_{\mathbf{x}} c_1 + \nabla_{\mathbf{y}} c_2 \pm z c_0 (\nabla_{\mathbf{x}} \varphi_1 + \nabla_{\mathbf{y}} \varphi_2) \pm z c_1 (\nabla_{\mathbf{x}} \varphi_0 + \nabla_{\mathbf{y}} \varphi_1)] \}, \quad \mathbf{y} \in \mathcal{P}_{\mathcal{U}} \end{aligned} \quad (\text{C.8a})$$

subject to

$$\mathbf{n} \cdot [\nabla_{\mathbf{x}} c_1 + \nabla_{\mathbf{y}} c_2 \pm z c_0 (\nabla_{\mathbf{x}} \varphi_1 + \nabla_{\mathbf{y}} \varphi_2) \pm z c_1 (\nabla_{\mathbf{x}} \varphi_0 + \nabla_{\mathbf{y}} \varphi_1)] = 0, \quad \mathbf{y} \in \Gamma_{\mathcal{U}}. \quad (\text{C.8b})$$

Approximating c_b and φ_b in (C.1) with their leading-order counterparts, c_0 and φ_0 , and integrating (C.8a) over $\mathcal{P}_{\mathcal{U}}$ leads to

$$\frac{\partial C}{\partial t} = \nabla_{\mathbf{x}} \cdot \left[\nabla_{\mathbf{x}} C \pm \frac{zC}{\omega} \nabla_{\mathbf{x}} \Phi_{\text{av}} + \frac{\omega}{G_{\pm} \|\mathcal{P}_{\mathcal{U}}\|} \int_{\mathcal{P}_{\mathcal{U}}} e^{\mp z\varphi_{\text{EDL}}} \nabla_{\mathbf{y}} (c_1 \pm z c_0 \varphi_1) d\mathbf{y} \right]. \quad (\text{C.9})$$

where G_{\pm} is defined in (3.15). Accounting for (E.10), this turns into

$$\frac{\partial C}{\partial t} = \nabla_{\mathbf{x}} \cdot \left[\left(\mathbf{I} + \frac{1}{G_{\pm}} \int_{\mathcal{P}_{\mathcal{U}}} e^{\mp z\varphi_{\text{EDL}}} \nabla_{\mathbf{y}} \boldsymbol{\chi}_{\pm}^\top d\mathbf{y} \right) (\nabla_{\mathbf{x}} C \pm \frac{zC}{\omega} \nabla_{\mathbf{x}} \Phi_{\text{av}}) \right]. \quad (\text{C.10})$$

To account for the effects of electrical potential in the solid matrix, it is common[70] to define an average potential for the fluid-solid mixture. In our context, it is equivalent to defining the average as $\Phi(\mathbf{x}, t) = \frac{1}{\|\mathcal{U}\|} \int_{\mathcal{P}_{\mathcal{U}}} \varphi_b(\mathbf{x}, \mathbf{y}, t) d\mathbf{y}$, i.e., setting $\Phi = \Phi_{\text{av}}/\omega$. This leads to (3.14) with the effective diffusion coefficient tensors $\mathbf{D}_{\pm}^{\text{eff}}$ given by (3.15).

The condition $\int_{\mathcal{P}_U} \chi_{\pm} d\mathbf{y} = 0$ also ensures the order (in ϵ) consistency between the approximations of the (dimensionless) bulk electrochemical potential $\hat{\mu}_{b\pm} = \ln \hat{c}_{b\pm} + z_{\pm} \hat{\phi}_b$ and other state variables. Indeed, dropping the hats, substituting the expansions (C.3) into this expression and retaining the terms up to the second order in ϵ yields $\mu_{b\pm} = \ln c_0 \pm z\varphi_0 + \epsilon(c_1 \pm zc_0\varphi_1)/c_0 + \mathcal{O}(\epsilon^2)$. Accounting for the closure (C.6) this leads to $\mu_{b\pm} = \ln c_0 \pm z\varphi_0 + \epsilon \chi_{\pm} \cdot \nabla_{\mathbf{x}}(\ln c_0 \pm z\varphi_0) + \mathcal{O}(\epsilon^2)$. Integration of this expression over \mathcal{P}_U yields the leading-order approximation of the average electrochemical potential in terms of the leading-order approximations of the average concentration and bulk potential.

Appendix D

Macroscopic model of an EDLC cell

Charge conservation. Total electrical current through a porous electroconductive material, $\mathbf{i} = \mathbf{i}_{\text{solid}} + \mathbf{i}_{\text{liquid}}$, is the sum of the currents through its solid ($\mathbf{i}_{\text{solid}}$) and liquid-saturated ($\mathbf{i}_{\text{liquid}}$) phases. Hence, conservation of the total charge, $\nabla \cdot \mathbf{i} = 0$ yields

$$\nabla \cdot \mathbf{i}_{\text{liquid}} = -\nabla \cdot \mathbf{i}_{\text{solid}}. \quad (\text{D.1})$$

Because of electric double layer charging/discharge, charges are storing in double layer capacitance. Conservation of charge in the liquid phase leads to[70],

$$\nabla \cdot \mathbf{i}_{\text{liquid}} = \mathcal{C}_{\text{EDL}} \frac{\partial(\Phi_s - \Phi)}{\partial t}, \quad (\text{D.2})$$

where \mathcal{C}_{EDL} is the EDL capacitance [F/cm³]. Substituting (D.1) into (D.2) and using Ohm's law in solid phase $\mathbf{i}_{\text{solid}} = -\sigma_s \nabla \Phi_s$, where σ_s is the electric conductivity of the

solid phase [S/m], yields

$$\mathcal{C}_{\text{EDL}} \frac{\partial(\Phi_s - \Phi)}{\partial t} = \nabla \cdot (\sigma_s \nabla \Phi_s). \quad (\text{D.3})$$

Mass conservation. Macroscopic mass balance (Nernst-Planck) equations for positively and negatively charged ions have the form

$$\omega \frac{\partial C_{\pm}}{\partial t} = -\nabla \cdot \mathbf{J}_{\text{NP}}^{\pm} + S_{\pm}, \quad \mathbf{J}_{\text{NP}}^{\pm} = -D_{\pm}^{\text{eff}} \nabla C_{\pm} - D_{\pm}^{\text{eff}} \frac{z_{\pm} F}{RT} C_{\pm} \nabla \Phi. \quad (\text{D.4})$$

The concentrations of cations (C_+) and anions (C_-) are related to the ion concentration C by

$$C = \frac{C_+}{\nu_+} = \frac{C_-}{\nu_-}, \quad (\text{D.5})$$

where ν_{\pm} are the dissociation coefficients. Combined with (D.5), the charge neutrality condition[70], $Fz_+C_+ + Fz_-C_- = 0$, gives

$$z_+\nu_+ + z_-\nu_- = 0. \quad (\text{D.6})$$

(For example, asymmetric electrolyte CaCl_2 has $\nu_+ = 1$ and $\nu_- = 2$, and the ion charges $z_+ = 2$ and $z_- = -1$.) The current density $S_{\pm}(\mathbf{x}, t)$ represents the rate of ion transfer to/from the EDL storage. We express it as

$$S_{\pm} = \mathcal{H}[\pm(\Phi - \Phi_s)] \mathcal{M} R_{\text{EDL}}, \quad (\text{D.7})$$

where $\mathcal{H}[\cdot]$ is the Heaviside function, $\mathcal{M}(\mathbf{x})$ is the membership function such that $\mathcal{M} = 1$ for all \mathbf{x} in the electrodes and $= 0$ otherwise, and the transfer rate R_{EDL} is defined as follows. Multiplying (D.4) with Fz_{\pm} and summing up the resulting two equations, while accounting for (D.5) and (D.6), yields $\nabla \cdot \mathbf{i}_{\text{liquid}} = F(z_+S_+ + z_-S_-)$; combining this with (D.2) and (D.7) gives an expression for the transfer rate,

$$\mathcal{M}R_{\text{EDL}} = \frac{\mathcal{C}_{\text{EDL}}}{\psi F} \frac{\partial(\Phi_s - \Phi)}{\partial t}, \quad (\text{D.8})$$

where $\psi = z_+\mathcal{H}(\Phi - \Phi_s) + z_-\mathcal{H}(\Phi_s - \Phi)$.

Problem reformulation in terms of charge current. The analyses[96, 70] found it necessary to rewrite conservation laws (D.4) and (D.1) in terms of the ionic flux $\mathbf{i}_{\text{liquid}} = F(z_+\mathbf{J}_{\text{NP}}^+ + z_-\mathbf{J}_{\text{NP}}^-)$. Substituting the definition of $\mathbf{J}_{\text{NP}}^{\pm}$ in (D.4) into this expression we obtain

$$\frac{\mathbf{i}_{\text{liquid}}}{\nu_+z_+F} = -\frac{F}{RT}(z_+D_+^{\text{eff}} + \frac{\nu_-z_-^2}{\nu_+z_+}D_-^{\text{eff}})C\nabla\Phi - (D_+^{\text{eff}} + \frac{\nu_-z_-}{\nu_+z_+}D_-^{\text{eff}})\nabla C. \quad (\text{D.9})$$

Using the latter to eliminate $C\nabla\Phi$ from the definition of \mathbf{J}_{NP}^+ leads to

$$\mathbf{J}_{\text{NP}}^+ = -\nu_+\mathcal{D}_+^{\text{eff}}\nabla C + \frac{t_+\mathbf{i}_{\text{liquid}}}{z_+F}, \quad (\text{D.10})$$

with the binary effective diffusion coefficient \mathcal{D}^{eff} and the transference number t_+ defined as

$$\mathcal{D}_+^{\text{eff}} = \frac{\nu_-z_-(z_- - z_+)D_+^{\text{eff}}D_-^{\text{eff}}}{\nu_+z_+^2D_+^{\text{eff}} + \nu_-z_-^2D_-^{\text{eff}}}, \quad t_+ = \frac{\nu_+z_+^2D_+^{\text{eff}}}{\nu_+z_+^2D_+^{\text{eff}} + \nu_-z_-^2D_-^{\text{eff}}}. \quad (\text{D.11})$$

By the same token, eliminating $C\nabla\Phi$ from the definition of \mathbf{J}_{NP}^- yields

$$\mathbf{J}_{\text{NP}}^- = -\nu_- \mathcal{D}_-^{\text{eff}} \nabla C + \frac{t_- \mathbf{i}_{\text{liquid}}}{z_- F}. \quad (\text{D.12})$$

with

$$\mathcal{D}_-^{\text{eff}} = \frac{\nu_+ z_+ (z_+ - z_-) D_+^{\text{eff}} D_-^{\text{eff}}}{\nu_+ z_+^2 D_+^{\text{eff}} + \nu_- z_-^2 D_-^{\text{eff}}}, \quad t_- = \frac{\nu_- z_-^2 D_-^{\text{eff}}}{\nu_+ z_+^2 D_+^{\text{eff}} + \nu_- z_-^2 D_-^{\text{eff}}}. \quad (\text{D.13})$$

Hence, we obtain a general expression for the ion fluxes

$$\mathbf{J}_{\text{NP}}^\pm = -\nu_\pm \mathcal{D}_\pm^{\text{eff}} \nabla C + \frac{t_\pm \mathbf{i}_{\text{liquid}}}{z_\pm F}. \quad (\text{D.14})$$

The charge conservation law (D.1) is rewritten[96, 70] by combining it with Ohm's law, $\mathbf{i}_{\text{solid}} = -\sigma_s \nabla \Phi_s$, the definition of the the ionic flux, $\mathbf{i}_{\text{liquid}} = F(z_+ \mathbf{J}_{\text{NP}}^+ + z_- \mathbf{J}_{\text{NP}}^-)$, and the definitions of $\mathbf{J}_{\text{NP}}^\pm$ in (D.4):

$$\nabla \cdot (\kappa^{\text{eff}} \nabla \Phi) + F \nabla \cdot [(\nu_+ z_+ \mathcal{D}_+^{\text{eff}} + \nu_- z_- \mathcal{D}_-^{\text{eff}}) C \nabla \ln C] = -\nabla \cdot (\sigma_s \nabla \Phi_s), \quad (\text{D.15})$$

where the effective conductivity of the electrolyte is defined as

$$\kappa^{\text{eff}} = \frac{F^2 C}{RT} (\nu_+ z_+^2 \mathcal{D}_+^{\text{eff}} + \nu_- z_-^2 \mathcal{D}_-^{\text{eff}}). \quad (\text{D.16})$$

When combined with the expressions for the transference numbers t_+ and t_- in (D.11) and (D.13), this definition of κ^{eff} transforms (D.15) into

$$\nabla \cdot \left[\kappa^{\text{eff}} \nabla \Phi + \kappa^{\text{eff}} \frac{RT}{F} \left(\frac{t_+}{z_+} + \frac{t_-}{z_-} \right) \nabla \ln C \right] = -\nabla \cdot (\sigma_s \nabla \Phi_s). \quad (\text{D.17})$$

A three-compartment formulation. The mass conservation equations (D.4) and (D.14) are simplified when written for each compartment (the two electrodes and separator in Fig. 3.3) separately. In the cathode ($0 < x < L_{\text{cat}}$), $\Phi - \Phi_s > 0$ and combining (D.4), (D.7), (D.8) and (D.14) yields mass conservation equations

$$\omega \frac{\partial C}{\partial t} = \nabla \cdot (\mathcal{D}_+^{\text{eff}} \nabla C) + \frac{t_- \mathcal{C}_{\text{EDL}}}{\nu_+ z_+ F} \frac{\partial(\Phi_s - \Phi)}{\partial t}, \quad (\text{D.18a})$$

and

$$\omega \frac{\partial C}{\partial t} = \nabla \cdot (\mathcal{D}_-^{\text{eff}} \nabla C) - \frac{t_- \mathcal{C}_{\text{EDL}}}{\nu_- z_- F} \frac{\partial(\Phi_s - \Phi)}{\partial t}. \quad (\text{D.18b})$$

These two equations are identical since, accounting for (D.6), $\mathcal{D}_+^{\text{eff}} = \mathcal{D}_-^{\text{eff}} \equiv \mathcal{D}^{\text{eff}}$. A similar procedure is used to derive mass conservation equations for the anode ($L_{\text{cat}} + L_{\text{sep}} < x < L$), wherein $\Phi - \Phi_s < 0$. Finally, mass conservation equations for the separator ($L_{\text{cat}} < x < L_{\text{sep}}$) are derived by setting $S_{\pm} = 0$. The resulting mass balance equation takes the form

$$\omega \frac{\partial C}{\partial t} = \nabla \cdot (\mathcal{D}^{\text{eff}} \nabla C) - \alpha \frac{\partial(\Phi_s - \Phi)}{\partial t}, \quad 0 < x < L; \quad (\text{D.19a})$$

and

$$\alpha = \begin{cases} \frac{t_- \mathcal{C}_{\text{EDL}}}{z_- \nu_- F} & 0 < x < L_{\text{cat}} \\ 0 & L_{\text{cat}} < x < L_{\text{cat}} + L_{\text{sep}} \\ \frac{t_+ \mathcal{C}_{\text{EDL}}}{z_+ \nu_+ F} & L_{\text{cat}} + L_{\text{sep}} < x < L. \end{cases} \quad (\text{D.19b})$$

The three conservation equations, (D.3), (D.17) and (D.19), govern the dy-

namics of the three state variables, $C(\mathbf{x}, t)$, $\Phi(\mathbf{x}, t)$ and $\Phi_s(\mathbf{x}, t)$. These equations are subject to boundary conditions at the EDLC external surfaces $x = 0$ and $x = L$. When solved separately in each of the compartments, they are also subject to continuity conditions at the internal interfaces $x = L_{\text{cat}}$ and $x = L_{\text{cat}} + L_{\text{sep}}$. [96]

Model simplification for symmetric binary electrolytes. These equations are simplified for a symmetric binary electrolyte ($\nu_+ = \nu_- \equiv \nu$) with equal of ion charges ($z_+ = -z_- \equiv z$). In this case, both $\mathcal{D}_+^{\text{eff}}$ in (D.11) and $\mathcal{D}_-^{\text{eff}}$ in (D.13) reduce to \mathcal{D}^{eff} given by (3.17), t_+ in (D.11) gives rise to its counterpart in (3.23b), t_- in (D.13) becomes $t_- = 1 - t_+$, and κ^{eff} in (D.16) is approximated with (3.23a) upon replacing the ion concentration C with its initial value c_{in} . Finally, the governing equations (D.3), (D.17) and (D.19) reduce to their one-dimensional counterparts (3.20), (3.21) and (3.22).

Appendix E

Homogenization of diffusion equation

Three types of local average of a quantity $A(\mathbf{x}, t)$ are defined

$$\langle A \rangle \equiv \frac{1}{\|\mathcal{U}\|} \int_{\mathcal{P}_{\mathcal{U}}(\mathbf{x})} A d\mathbf{y}, \quad \langle A \rangle_{\mathcal{P}} \equiv \frac{1}{\|\mathcal{P}_{\mathcal{U}}\|} \int_{\mathcal{P}_{\mathcal{U}}(\mathbf{x})} A d\mathbf{y}, \quad \langle A \rangle_{\Gamma} \equiv \int_{\Gamma_{\mathcal{U}}(\mathbf{x})} A d\mathbf{y}, \quad (\text{E.1})$$

such that $\langle A \rangle = \phi \langle A \rangle_{\mathcal{P}}$ where $\phi = \|\mathcal{P}_{\mathcal{U}}\|/\|\mathcal{U}\|$ is the porosity. We use the multiple-scale expansion technique [42] to derive effective continuum scale equations for average concentration $C(\mathbf{x}, t) \equiv \langle c(\mathbf{x}, t) \rangle$. The method postulates that concentration exhibits both large-scale (across the porous material, denoted by the coordinate \mathbf{x}) and small-scale (inside individual pores, denoted by the coordinate \mathbf{y}) spatial variability, such that $\mathbf{y} = \epsilon^{-1} \mathbf{x}$ with $\epsilon \ll 1$;

Let us introduce a membership (indicator) function $\Pi(\mathbf{x}) = \Pi(\mathbf{x}/\epsilon)$,

$$\Pi(\mathbf{x}) = \begin{cases} 1, & \mathbf{x} \in \mathcal{P} \\ 0, & \mathbf{x} \in \mathcal{S}. \end{cases} \quad (\text{E.2})$$

For the nanoporous materials under consideration, the function $\Pi(\mathbf{x}) = \Pi(\mathbf{x}/\epsilon)$ is periodic on the unit cell \mathcal{U} . This allows one to define the pore-scale diffusion equation (5.1) on the whole unit cell \mathcal{U} (rather than on the multi-connected subdomain $\mathcal{P}_{\mathcal{U}}$ occupied the liquid),

$$\frac{\partial c}{\partial t} = \nabla \cdot (\Pi \nabla c), \quad \mathbf{y} \in \mathcal{U}, \quad t > 0. \quad (\text{E.3})$$

Replacing the concentration $c(\mathbf{x}, t)$ with $c(\mathbf{x}, \mathbf{y}, t, \tau_r)$ and substituting into Eq. (E.3) yields

$$\frac{\partial c}{\partial t} = \nabla_{\mathbf{x}} \cdot [\Pi(\nabla_{\mathbf{x}} c + \epsilon^{-1} \nabla_{\mathbf{y}} c)] + \epsilon^{-1} \nabla_{\mathbf{y}} \cdot [\Pi(\nabla_{\mathbf{x}} c + \epsilon^{-1} \nabla_{\mathbf{y}} c)], \quad \mathbf{y} \in \mathcal{U}. \quad (\text{E.4a})$$

The interfacial condition (5.2) takes the form

$$-\mathbf{n} \cdot (\nabla_{\mathbf{x}} c + \epsilon^{-1} \nabla_{\mathbf{y}} c) = 0, \quad \mathbf{y} \in \Gamma_{\mathcal{U}}. \quad (\text{E.4b})$$

In the multiple-scale expansion method, the concentration $c(\mathbf{x}, \mathbf{y}, t, \tau_r)$ is represented by an asymptotic series

$$c(\mathbf{x}, \mathbf{y}, t, \tau_r) = \sum_{m=0}^{\infty} \epsilon^m c_m(\mathbf{x}, \mathbf{y}, t, \tau_r). \quad (\text{E.5})$$

we obtain

$$\begin{aligned}
& -\epsilon^{-2} \nabla_{\mathbf{y}} \cdot (\Pi \nabla_{\mathbf{y}} c_0) \\
& -\epsilon^{-1} \{ \nabla_{\mathbf{x}} \cdot (\Pi \nabla_{\mathbf{y}} c_0) + \nabla_{\mathbf{y}} \cdot [\Pi(\nabla_{\mathbf{y}} c_1 + \nabla_{\mathbf{x}} c_0)] \} \\
& + \epsilon^0 \left\{ \frac{\partial c_0}{\partial t} - \nabla_{\mathbf{x}} \cdot [\Pi(\nabla_{\mathbf{x}} c_0 + \nabla_{\mathbf{y}} c_1)] - \nabla_{\mathbf{y}} \cdot [\Pi(\nabla_{\mathbf{x}} c_1 + \nabla_{\mathbf{y}} c_2)] \right\} = \mathcal{O}(\epsilon^1), \quad \mathbf{y} \in \mathcal{U}
\end{aligned} \tag{E.6}$$

and

$$\begin{aligned}
& -\epsilon^{-1} \mathbf{n} \cdot \nabla_{\mathbf{y}} c_0 - \epsilon^0 [\mathbf{n} \cdot (\nabla_{\mathbf{x}} c_0 + \nabla_{\mathbf{y}} c_1)] \\
& - \epsilon^1 [\mathbf{n} \cdot (\nabla_{\mathbf{x}} c_1 + \nabla_{\mathbf{y}} c_2)] = \mathcal{O}(\epsilon^2), \quad \mathbf{y} \in \Gamma_{\mathcal{U}}.
\end{aligned} \tag{E.7}$$

Collecting terms of the equal powers of ϵ yields boundary-value problems (BVPs) for $c_m(\mathbf{x}, \mathbf{y}, t, \tau_r)$ ($m = 0, 1, \dots$).

Leading-order term, $\mathcal{O}(\epsilon^{-2})$. Collecting the $\mathcal{O}(\epsilon^{-2})$ terms yields a BVP for the leading-order term in the expansion (E.5),

$$\nabla_{\mathbf{y}} \cdot (\Pi \nabla_{\mathbf{y}} c_0) = 0, \quad \mathbf{y} \in \mathcal{U}; \quad -\mathbf{n} \cdot \nabla_{\mathbf{y}} c_0 = 0, \quad \mathbf{y} \in \Gamma_{\mathcal{U}}. \tag{E.8}$$

This BVP has a trivial solution, which implies that c_0 is independent of \mathbf{y} .

Term of order $\mathcal{O}(\epsilon^{-1})$. Since $\text{Da} \sim \mathcal{O}(\epsilon^1)$, collecting the $\mathcal{O}(\epsilon^{-1})$ terms yields a BVP for the first-order term in the expansion (E.5),

$$\nabla_{\mathbf{y}} \cdot [\Pi(\nabla_{\mathbf{x}} c_0 + \nabla_{\mathbf{y}} c_1)] = 0, \quad \mathbf{y} \in \mathcal{U} \tag{E.9a}$$

subject to the interfacial condition

$$-\mathbf{n} \cdot (\nabla_{\mathbf{x}} c_0 + \nabla_{\mathbf{y}} c_1) = 0, \quad \mathbf{y} \in \Gamma_{\mathcal{U}}. \quad (\text{E.9b})$$

Equations (E.9), which form a BVP for $c_1(\mathbf{x}, \mathbf{y}, t, \tau_r)$, define a local problem. It depends only on the geometry of the unit cell. We represent its solution as [42, 14]

$$c_1(\mathbf{x}, \mathbf{y}, t, \tau_r) = \boldsymbol{\chi}(\mathbf{y}) \cdot \nabla_{\mathbf{x}} c_0(\mathbf{x}, t, \tau_r) + \bar{c}_1(\mathbf{x}, t, \tau_r). \quad (\text{E.10})$$

Substituting this into Eq. (E.9a) yields an equation for the closure variable (a vector) $\boldsymbol{\chi}(\mathbf{y})$,

$$\nabla_{\mathbf{y}} \cdot (\mathbf{I} + \nabla_{\mathbf{y}} \boldsymbol{\chi}) \nabla_{\mathbf{x}} c_0 = 0, \quad \mathbf{y} \in \mathcal{P}_{\mathcal{U}} \quad (\text{E.11})$$

This equation is subject to $\langle \boldsymbol{\chi} \rangle = \mathbf{0}$ and the boundary condition

$$\mathbf{n} \cdot (\mathbf{I} + \nabla_{\mathbf{y}} \boldsymbol{\chi}) \nabla_{\mathbf{x}} c_0 = 0, \quad \mathbf{y} \in \Gamma_{\mathcal{U}}, \quad (\text{E.12})$$

which is obtained by substituting Eq. (E.10) into Eq. (E.9b).

Terms of order $\mathcal{O}(\epsilon^0)$. Collecting the terms of order ϵ (E.6) yields

$$\frac{\partial c_0}{\partial t} - \nabla_{\mathbf{x}} \cdot [\Pi(\nabla_{\mathbf{x}} c_0 + \nabla_{\mathbf{y}} c_1)] - \nabla_{\mathbf{y}} \cdot [\Pi(\nabla_{\mathbf{x}} c_1 + \nabla_{\mathbf{y}} c_2)] = 0, \quad \mathbf{y} \in \mathcal{U} \quad (\text{E.13a})$$

subject to the interfacial condition

$$-\mathbf{n} \cdot (\nabla_{\mathbf{x}} c_1 + \nabla_{\mathbf{y}} c_2) = 0, \quad \mathbf{y} \in \Gamma_{\mathcal{U}}, \quad (\text{E.13b})$$

Integrating over \mathcal{U} with respect to \mathbf{y} , applying the interfacial conditions (E.13b), and

accounting for the periodicity of $\Pi(\mathbf{y})$ on the boundary of the unit cell \mathcal{U} , we obtain

$$\varepsilon \frac{\partial c_0}{\partial t} - \nabla_{\mathbf{x}} \cdot (\langle (\mathbf{I} + \nabla_{\mathbf{y}} \chi) \rangle \nabla_{\mathbf{x}} c_0) = 0 \quad (\text{E.14})$$

ε is the porosity and effective diffusion coefficient $\mathbf{D}_{\text{eff}}/D = \langle (\mathbf{I} + \nabla_{\mathbf{y}} \chi) \rangle$ is defined in (5.5). Defining its average over the cell as $C(\mathbf{x}, t) \equiv \langle c(\mathbf{x}, t) \rangle$ leads to the homogenized continuum-scale diffusion-reaction equation for the average concentration (5.4).

Bibliography

- [1] Basic research needs for electric energy storage. Technical report, United State Department of Energy, 2007.
- [2] S. P. Adiga, L. A. Curtiss, J. W. Elam, M. J. Pellin, C.-C. Shih, C.-M. Shih, S.-J. Lin, Y.-Y. Su, S. D. Gittard, and J. Zhang. Nanoporous materials for biomedical devices. *JOM*, 60(3):26–32, 2008.
- [3] Pierre M Adler, Christian G Jacquin, and Jean-François Thovert. The formation factor of reconstructed porous media. *Water Resources Research*, 28(6):1571–1576, 1992.
- [4] G. Allaire, R. Brizzi, A. Mikelić, and A. Piatnitski. Two-scale expansion with drift approach to the Taylor dispersion for reactive transport through porous media. *Chem. Engrg. Sci.*, 65(7):2292–2300, 2010.
- [5] G. Allaire, A. Mikelić, and A. Piatnitski. Homogenization approach to the dispersion theory for reactive transport through porous media. *SIAM J. Math. Anal.*, 42(1):125–144, 2010.
- [6] Srikanth Allu, B Velamur Asokan, William A Shelton, Bobby Philip, and Sreekanth Pannala. A generalized multi-dimensional mathematical model for charging and discharging processes in a supercapacitor. *J. Power Sources*, 256:369–382, 2014.
- [7] J. L. Auriault. Heterogeneous media: is an equivalent homogeneous description always possible? *Int. J. Engrg. Sci.*, 29(7):785–795, 1991.
- [8] J. L. Auriault and J. Lewandowska. Homogenization analysis of diffusion and adsorption macrotransport in porous media: macrotransport in the absence of advection. *Geotechnique*, 43(3):457–69, 1993.
- [9] Jean-Louis Auriault, Claude Boutin, and Christian Geindreau. *Homogenization of coupled phenomena in heterogeneous media*, volume 149. John Wiley & Sons, 2010.
- [10] Jean-Louis Auriault and Jolanta Lewandowska. Effective diffusion coefficient: from homogenization to experiment. *Transport Porous Med.*, 27(2):205–223, 1997.

- [11] Saeid Azizian. Kinetic models of sorption: a theoretical analysis. *J. Colloid Interface Sci.*, 276(1):47–52, 2004.
- [12] O Barbieri, M Hahn, A Herzog, and R Kötz. Capacitance limits of high surface area activated carbons for double layer capacitors. *Carbon*, 43(6):1303–1310, 2005.
- [13] Thomas M Bartol Jr, Cailey Bromer, Justin Kinney, Michael A Chirillo, Jennifer N Bourne, Kristen M Harris, and Terrence J Sejnowski. Nanoconnectomic upper bound on the variability of synaptic plasticity. *Elife*, 4:e10778, 2015.
- [14] I. Battiato and D. M. Tartakovsky. Applicability regimes for macroscopic models of reactive transport in porous media. *J. Contam. Hydrol.*, 120-121:18–26, 2011.
- [15] Jacob Bear and AH-D Cheng. *Modeling groundwater flow and contaminant transport*, volume 23. Springer, 2010.
- [16] Juergen Biener, Gregory W. Nyce, Andrea M. Hodge, Monika M. Biener, Alex V. Hamza, and Stefan A. Maier. Nanoporous plasmonic metamaterials. *Adv. Mater.*, 9999:1–7, 2008.
- [17] P. M. Biesheuvel and M. Z. Bazant. Nonlinear dynamics of capacitive charging and desalination by porous electrodes. *Phys. Rev. E*, 81(3):031502, 2010.
- [18] S. G. Bie and D. C. Prieve. Electrohydrodynamics of thin double layers: a model for the streaming potential profile. *J. Colloid Interf. Sci.*, 154(1):87–96, 1992.
- [19] I. Bispo-Fonseca, J. Aggar, C. Sarrazin, P. Simon, and J. F. Fauvarque. Possible improvements in making carbon electrodes for organic supercapacitors. *J. Power Sources*, 79(2):238–241, 1999.
- [20] Henri Casanova, Thomas M Bartol, Joel Stiles, and Francine Berman. Distributing mcell simulations on the grid. *International Journal of High Performance Computing Applications*, 15(3):243–257, 2001.
- [21] G A Chechkin, A L Piatnitski, and A S Shamaev. *Homogenization*, volume 234 of *Translations of Mathematical Monographs*. American Mathematical Society, Providence, RI, 2007.
- [22] CW Cheung, JF Porter, and G McKay. Sorption kinetics for the removal of copper and zinc from effluents using bone char. *Separation Purification Tech.*, 19(1):55–64, 2000.
- [23] J. Chmiola, G. Yushin, Y. Gogotsi, C. Portet, P. Simon, and P. L. Taberna. Anomalous increase in carbon capacitance at pore sizes less than 1 nanometer. *Science*, 313(5794):1760–1763, 2006.
- [24] D.-W. Chung, Martin Ebner, David R Ely, Vanessa Wood, and R Edwin García.

- Validity of the Bruggeman relation for porous electrodes. *Modelling Simul. Mater. Sci. Eng.*, 21:074009, 2013.
- [25] Brian E. Conway. *Electrochemical supercapacitors: scientific fundamentals and technological applications*. Springer, 2013.
 - [26] Liming Dai, Dong Wook Chang, Jong-Beom Baek, and Wen Lu. Carbon nanomaterials for advanced energy conversion and storage. *small*, 8(8):1130–1166, 2012.
 - [27] Mark E Davis. Ordered porous materials for emerging applications. *Nature*, 417(6891):813–821, 2002.
 - [28] Tejal A Desai, Derek J Hansford, Lawrence Kulinsky, Amir H Nashat, Guido Rasi, Jay Tu, Yuchun Wang, Miqin Zhang, and Mauro Ferrari. Nanopore technology for biomedical applications. *Biomed. Microdevices*, 2(1):11–40, 1999.
 - [29] Yalchin Efendiev and Thomas Y Hou. *Multiscale finite element methods: theory and applications*, volume 4. Springer Science & Business Media, 2009.
 - [30] C. G. Enfield, C. C. Harlin, and B. E. Bledsoe. Comparison of five kinetic models for orthophosphate reactions in mineral soils. *Soil Sci. Soc. Am. J.*, 40(2):243–249, 1976.
 - [31] David Ferry and Stephen Marshall Goodnick. *Transport in nanostructures*. Number 6. Cambridge university press, 1997.
 - [32] Brian P Flannery, Harry W Deckman, Wayne G Roberge, and KEVIN L D’AMICO. Three-dimensional x-ray microtomography. *Science*, 237(4821):1439–1444, 1987.
 - [33] EJ Garboczi and Anthony Roy Day. An algorithm for computing the effective linear elastic properties of heterogeneous materials: three-dimensional results for composites with equal phase poisson ratios. *Journal of the Mechanics and Physics of Solids*, 43(9):1349–1362, 1995.
 - [34] Daniel E Giammar and Janet G Hering. Time scales for sorption-desorption and surface precipitation of uranyl on goethite. *Environ. Sci. Tech.*, 35(16):3332–3337, 2001.
 - [35] David C Grahame. Differential capacity of mercury in aqueous sodium fluoride solutions. I. Effect of concentration at 25°. *J. Am. Chem. Soc.*, 76(19):4819–4823, 1954.
 - [36] Carlos A Grattoni, Richard A Dawe, and Mirtha S Bidner. On the simultaneous determination of dispersion and nonlinear adsorption parameters from displacement tests by using numerical models and optimisation techniques. *Adv. Water Resour.*, 16(2):127–135, 1993.

- [37] A Gully, H Liu, S Srinivasan, A. K. Sethurajan, S Schougaard, and B Protas. Effective transport properties of porous electrochemical materials—a homogenization approach. *J. Electrochem. Soc.*, 161(8):E3066–E3077, 2014.
- [38] Ilenia Battiato Harikesh Arunachalam, Simona Onori. On veracity of macroscopic lithium-ion battery models. *J. Electrochem. Soc.*, 162(10):A1940–A1951, 2015.
- [39] Paul Heitjans and Jörg Kärger. *Diffusion in condensed matter: methods, materials, models*. Springer Science & Business Media, 2006.
- [40] D Hlushkou, H Liasneuski, U Tallarek, and S Torquato. Effective diffusion coefficients in random packings of polydisperse hard spheres from two-point and three-point correlation functions. *Journal of Applied Physics*, 118(12):124901, 2015.
- [41] Yuh-Shan Ho and Gordon McKay. Pseudo-second order model for sorption processes. *Process Biochem.*, 34(5):451–465, 1999.
- [42] U. Hornung. *Homogenization and Porous Media*. Springer, New York, 1997.
- [43] Robert J Hunter. *Foundations of colloid science*. Oxford University Press, 2001.
- [44] Toufik Kanit, Franck Nâ€™Guyen, Samuel Forest, Dominique Jeulin, Matt Reed, and Scott Singleton. Apparent and effective physical properties of heterogeneous materials: representativity of samples of two materials from food industry. *Computer Methods in Applied Mechanics and Engineering*, 195(33):3960–3982, 2006.
- [45] Jörg Kärger, Douglas M Ruthven, and Doros N Theodorou. *Diffusion in nanoporous materials*. John Wiley & Sons, 2012.
- [46] George Karniadakis, Ali Beskok, and Narayan Aluru. *Microflows and nanoflows: fundamentals and simulation*, volume 29. Springer Science & Business Media, 2006.
- [47] Ali Ghorbani Kashkooli, Siamak Farhad, Victor Chabot, Aiping Yu, and Zhongwei Chen. Effects of structural design on the performance of electrical double layer capacitors. *Appl. Energ.*, 138:631–639, 2015.
- [48] Brian J Kirby. *Micro-and nanoscale fluid mechanics: transport in microfluidic devices*. Cambridge University Press, 2010.
- [49] M. P. Klein, B. W. Jacobs, M. D. Ong, S. J. Fares, D. B. Robinson, V. Stavila, G. J. Wagner, and I. Arslan. Three-dimensional pore evolution of nanoporous metal particles for energy storage. *J. Am. Chem. Soc.*, 133(24):9144–9147, 2011.
- [50] S. Kondrat, C. R. Pérez, V. Presser, Y. Gogotsi, and A. A. Kornyshev. Effect of pore size and its dispersity on the energy storage in nanoporous supercapacitors. *Energy Environ. Sci.*, 5:6474–6479, 2012.

- [51] A Koponen, M Kataja, and Jv Timonen. Tortuous flow in porous media. *Physical Review E*, 54(1):406, 1996.
- [52] K. L. Kostka, M. D. Radcliffe, and E. von Meerwall. Diffusion coefficients of methylene blue and thioflavin T dyes in methanol solution. *J. Phys. Chem.*, 96(5):2289–2292, 1992.
- [53] Svenska Lagergren. About the theory of so-called adsorption of soluble substances. *Kungliga Svenska Vetenskapsakademiens Handlingar*, 24(4):1–39, 1898.
- [54] Tien Dung Le, Christian Moyne, and Marcio A Murad. A three-scale model for ionic solute transport in swelling clays incorporating ion–ion correlation effects. *Adv. Water Resour.*, 75:31–52, 2015.
- [55] Gyoung-Ja Lee and Su-Il Pyun. Theoretical approach to ion penetration into pores with pore fractal characteristics during double-layer charging/discharging on a porous carbon electrode. *Langmuir*, 22(25):10659–10665, 2006.
- [56] Quan Li. *Nanomaterials for Sustainable Energy*. Springer, 2016.
- [57] G Limousin, J-P Gaudet, L Charlet, S Szenknect, V Barthes, and M Krimissa. Sorption isotherms: a review on physical bases, modeling and measurement. *Appl. Geochem.*, 22(2):249–275, 2007.
- [58] Jason R Looker and Steven L Carnie. Homogenization of the ionic transport equations in periodic porous media. *Transport Porous Med.*, 65(1):107–131, 2006.
- [59] GQ Lu and Xiu Song Zhao. *Nanoporous materials: science and engineering*, volume 4. World Scientific, 2004.
- [60] Edward Allen Mason and AP Malinauskas. *Gas transport in porous media: the dusty-gas model*, volume 17. Elsevier Science Ltd, 1983.
- [61] S. T. Mayer, R. W. Pekala, and J. L. Kaschmitter. The aerocapacitor: An electrochemical double-layer energy-storage device. *J. Electrochem. Soc.*, 140(2):446–451, 1993.
- [62] Isamu Moriguchi, Masakuni Honda, Taro Ohkubo, Yoshio Mawatari, and Yasutake Teraoka. Adsorption and photocatalytic decomposition of methylene blue on mesoporous metallosilicates. *Catalysis Today*, 90(3-4):297–303, 2004.
- [63] Isamu Moriguchi, Yuki Shono, Hirotohi Yamada, and Tetsuichi Kudo. Colloidal crystal-derived nanoporous electrode materials of cut SWNTs-assembly and TiO₂/SWNTs nanocomposite. *J. Phys. Chem. B*, 112:14560–14565, 2008.
- [64] Russell E Morris and Paul S Wheatley. Gas storage in nanoporous materials. *Angewandte Chemie International Edition*, 47(27):4966–4981, 2008.
- [65] Christian Moyne and Márcio A Murad. Electro-chemo-mechanical couplings in

- swelling clays derived from a micro/macro-homogenization procedure. *Int. J. Solids Struct.*, 39(25):6159–6190, 2002.
- [66] Christian Moyne and Márcio A Murad. A two-scale model for coupled electro-chemo-mechanical phenomena and Onsager’s reciprocity relations in expansive clays: I homogenization analysis. *Transport Porous Med.*, 62(3):333–380, 2006.
 - [67] Deqiang Mu, Zhong-Sheng Liu, Cheng Huang, and Ned Djilali. Determination of the effective diffusion coefficient in porous media including knudsen effects. *Microfluidics and Nanofluidics*, 4(3):257–260, 2008.
 - [68] Márcio A Murad and Christian Moyne. A dual-porosity model for ionic solute transport in expansive clays. *Comput. Geosci.*, 12(1):47–82, 2008.
 - [69] Rajaram Narayanan, Hema Vijwani, Sharmila M. Mukhopadhyay, and Prabhakar R. Bandaru. Electrochemical charge storage in hierarchical carbon manifolds. *Carbon*, 99:267–271, 2016.
 - [70] John Newman and Karen E Thomas-Alyea. *Electrochemical Systems*. John Wiley & Sons, 2012.
 - [71] Christof M Niemeyer. Nanoparticles, proteins, and nucleic acids: biotechnology meets materials science. *Angewandte Chemie International Edition*, 40(22):4128–4158, 2001.
 - [72] Takahiro Ohkubo, Jin Miyawaki, Katsumi Kaneko, Ryong Ryoo, and Nigel A. Seaton. Adsorption properties of templated mesoporous carbon (CMK-1) for nitrogen and supercritical methane experiment and GCMC simulation. *J. Phys. Chem. B*, 106(25):6523–6528, 2002.
 - [73] M. J. Pellin, P. C. Stair, G. Xiong, J. W. Elam, J. Birrell, L. Curtiss, S. M. George, C. Y. Han, L. Iton, and H. Kung. Mesoporous catalytic membranes: synthetic control of pore size and wall composition. *Catal. Lett.*, 102(3-4):127–130, 2005.
 - [74] Wojciech Plazinski, Wladyslaw Rudzinski, and Anita Plazinska. Theoretical models of sorption kinetics including a surface reaction mechanism: a review. *Adv. Colloid Interface Sci.*, 152(1):2–13, 2009.
 - [75] J Poutet, D Manzoni, F Hage-Chehade, J-F Thovert, and PM Adler. The effective mechanical properties of random porous media. *Journal of the Mechanics and Physics of Solids*, 44(10):1587–1620, 1996.
 - [76] Zacaria Reddad, Claire Gerente, Yves Andres, and Pierre Le Cloirec. Adsorption of several metal ions onto a low-cost biosorbent: kinetic and equilibrium studies. *Environ. Sci. Tech.*, 36(9):2067–2073, 2002.
 - [77] A. J. Rosenbloom, D. M. Sipe, Y. Shishkin, Y. Ke, R. P. Devaty, and W. J. Choyke. Nanoporous SiC: A candidate semi-permeable material for biomedical

- applications. *Biomed. Microdevices*, 6(4):261–267, 2004.
- [78] Muhammad Sahimi. *Flow and transport in porous media and fractured rock: from classical methods to modern approaches*. John Wiley & Sons, 2011.
 - [79] Soheil Saraji, Lamia Goual, and Mohammad Piri. Adsorption of asphaltenes in porous media under flow conditions. *Energy Fuels*, 24(11):6009–6017, 2010.
 - [80] Mehmet Sarikaya, Candan Tamerler, Alex K-Y Jen, Klaus Schulten, and Francois Baneyx. Molecular biomimetics: nanotechnology through biology. *Nature materials*, 2(9):577–585, 2003.
 - [81] K Prasad Saripalli, R Jeffery Serne, Philip D Meyer, and B Peter McGrail. Prediction of diffusion coefficients in porous media using tortuosity factors based on interfacial areas. *Ground Water*, 40(4):346–352, 2002.
 - [82] Dale W Schaefer. Engineered porous materials. *MRS Bulletin*, 19(04):14–19, 1994.
 - [83] M. Schmuck and M. Z. Bazant. Homogenization of the Poisson-Nernst-Planck equations for ion transport in charged porous media. *SIAM J. Appl. Math.*, 75(3):1369–1401, 2015.
 - [84] Julian Seymour Schwinger, WY Tsai, Lester L De Raad, and KA Milton. *Classical electrodynamics*. Perseus, 1998.
 - [85] Jung Soo Seo, Dongmok Whang, Hyoyoung Lee, Sung Im Jun, Jinho Oh, Young Jin Jeon, and Kimoon Kim. A homochiral metal–organic porous material for enantioselective separation and catalysis. *Nature*, 404(6781):982–986, 2000.
 - [86] G. Severino, G. Dagan, and C. J. van Duijn. A note on transport of a pulse of nonlinearly reactive solute in a heterogeneous formation. *J. Comput. Geosci*, 4:275–286, 2000.
 - [87] R. D. Shannon. Revised effective ionic radii and systematic studies of interatomic distances in halides and chalcogenides. *Acta Cryst.*, A32(5):751–767, 1976.
 - [88] Hang Shi. Activated carbons and double layer capacitance. *Electrochimica Acta*, 41(10):1633–1639, 1996.
 - [89] A Soffer and M Folman. The electrical double layer of high surface porous carbon electrode. *J. Electroanal. Chem. Interfacial Electrochem.*, 38(1):25–43, 1972.
 - [90] P Spanne, JF Thovert, CJ Jacquin, WB Lindquist, KW Jones, and PM Adler. Synchrotron computed microtomography of porous media: topology and transports. *Physical Review Letters*, 73(14):2001, 1994.
 - [91] Indrajeet V Thorat, David E Stephenson, Nathan A Zacharias, Karim Zaghib, John N Harb, and Dean R Wheeler. Quantifying tortuosity in porous Li-ion

- battery materials. *J. Power Sources*, 188(2):592–600, 2009.
- [92] Claudia Timofte. Homogenization results for ionic transport in periodic porous media. *Comput. Math. Appl.*, 68(9):1024–1031, 2014.
 - [93] Salvatore Torquato. *Random heterogeneous materials: microstructure and macroscopic properties*, volume 16. Springer Science & Business Media, 2013.
 - [94] Cornelius J Van Duijn and Peter Knabner. Travelling waves in the transport of reactive solutes through porous media: Adsorption and binary ion exchange-Part 1. *Trans. Porous Media*, 8(2):167–194, 1992.
 - [95] Julian Varghese, Hainan Wang, and Laurent Pilon. Simulating electric double layer capacitance of mesoporous electrodes with cylindrical pores. *J. Electrochem. Soc.*, 158(10):A1106–A1114, 2011.
 - [96] Mark W Verbrugge and Ping Liu. Microstructural analysis and mathematical modeling of electric double-layer supercapacitors. *J. Electrochem. Soc.*, 152(5):D79–D87, 2005.
 - [97] Da-Wei Wang, Feng Li, Min Liu, Gao Qing Lu, and Hui-Ming Cheng. 3d aperiodic hierarchical porous graphitic carbon material for high-rate electrochemical capacitive energy storage. *Angewandte Chemie*, 120(2):379–382, 2008.
 - [98] Guoping Wang, Lei Zhang, and Jiujuun Zhang. A review of electrode materials for electrochemical supercapacitors. *Chemical Society Reviews*, 41(2):797–828, 2012.
 - [99] W. J. Weber, P. M. McGinley, and L. E. Katz. Sorption phenomena in subsurface systems: concepts, models and effects on contaminant fate and transport. *Water Res.*, 25(5):499–528, 1991.
 - [100] E Weinan. *Principles of multiscale modeling*. Cambridge University Press, 2011.
 - [101] Harold L Weissberg. Effective diffusion coefficient in porous media. *Journal of Applied Physics*, 34(9):2636–2639, 1963.
 - [102] S. Whitaker. *The method of volume averaging*. Netherlands: Kluwer Academic Publishers, 1999.
 - [103] Kaisheng Xia, Qiuming Gao, Jinhua Jiang, and Juan Hu. Hierarchical porous carbons with controlled micropores and mesopores for supercapacitor electrode materials. *Carbon*, 46(13):1718–1726, 2008.
 - [104] Hirotoshi Yamada, Haruka Nakamura, Fumihiro Nakahara, Isamu Moriguchi, and Tetsuichi Kudo. Electrochemical study of high electrochemical double layer capacitance of ordered porous carbons with both meso/macropores and micropores. *J. Phys. Chem. C*, 111(1):227–233, 2007.
 - [105] Cheol-Min Yang, Yong-Jung Kim, Morinobu Endo, Hirofumi Kanoh, Masako

- Yudasaka, Sumio Iijima, and Katsumi Kaneko. Nanowindow-regulated specific capacitance of supercapacitor electrodes of single-wall carbon nanohorns. *J. Am. Chem. Soc.*, 129(1):20–21, 2007.
- [106] Kun-Lin Yang, Tung-Yu Ying, Sotira Yiacoumi, Costas Tsouris, and E Steven Vittoratos. Electrosorption of ions from aqueous solutions by carbon aerogel: an electrical double-layer model. *Langmuir*, 17(6):1961–1969, 2001.
- [107] Laura Yeomans, Scott E Feller, Enrique Sánchez, and Marcelo Lozada-Cassou. The structure of electrolytes in cylindrical pores. *The Journal of chemical physics*, 98(2):1436–1450, 1993.
- [108] Li Li Zhang and X. S. Zhao. Carbon-based materials as supercapacitor electrodes. *Chem. Soc. Rev.*, 38:2520–2531, 2009.
- [109] X. Zhang and D. M. Tartakovsky. Effective ion diffusion in charged nanoporous materials. *J. Electrochem. Soc.*, 2016, under review.
- [110] X. Zhang, K. Urita, I. Moriguchi, and D. M. Tartakovsky. Design of nanoporous materials with optimal sorption capacity. *J. Appl. Phys.*, 117(24):244304, 2015.